Large area electro-optical tactile sensor: Characterization and design of a polymer, nanoparticle based tunneling device

Vivek Chandra Maheshwari

Dissertation submitted to the faculty of the Virginia Polytechnic Institute and State University in partial fulfillment of the requirements for the degree of

Doctor of Philosophy
In
Macromolecular Science and Engineering

David Cox, Chairman
Ravi Saraf, Co-Chairman
Garth Wilkes
Richey Davis
Alan Esker

04th, December 2006
Blacksburg, Virginia USA

Keywords: Tactile Sensor, Electronic Skin, Tunneling, Self-assembly, Nanoparticles, Polyelectrolyte, Large Area Device, Thin Film, Electroluminescence

Large area electro-optical tactile sensor: Characterization and design of a polymer, nanoparticle based tunneling device

Vivek Chandra Maheshwari

Abstract

Touch (or tactile) sensors are gaining renewed interest as the level of sophistication in the application of minimally invasive surgery and humanoid robots increases. The spatial resolution of current large-area tactile sensors (greater than 1 cm^2) lag human fingers by over an order of magnitude. Using metal and semiconducting nanoparticles, a ~100 nm thick, large area thin-film device working on the principles of electron tunneling is self-assembled, such that the change in current density through the film and the electroluminescence light intensity are linearly proportional to the local stress. By pressing a United States 1 cent coin (and also a copper grid) on the device a well resolved stress image by focusing the electroluminescence light directly on CCD is obtained. Both the lateral and height resolution of texture are comparable to human finger at similar stress levels of ~10 KPa.

The fabrication of the film is based on self-assembly of polyelectrolytes, and metal and semiconducting nanoparticles in a layered architecture. The polyelectrolyte layer functions as the dielectric tunneling barrier and the nanoparticles function as the base for tunneling electrons. The assembly of the device can be simplified by incorporating the functionality of polyelectrolyte and nanoparticles in a single composite medium. A non-micellar mineralization process for the synthesis of multifunctional nanocomposite materials is also reported as a possible building block for the assembly of tactile sensor. The non-micellar method results in the synthesis of monodisperse semiconducting nanoparticles templated on polymer chains dissolved in solution at high yield. The monodispersity is achieved due to the beaded necklace morphology of the polyelectrolyte chains in solution where the beads are nanometer-scale nodules in the polymer chain and the nanoparticles are confined to the beads. The resultant structure is a nanoparticle studded necklace where the particles are imbedded in the beads. Multiple cycles of synthesis on the polymer template yield nanoparticles of identical size, resulting in a nanocomposite with high particle fraction. The resultant nanocomposite has beaded-fibrilar morphology with imbedded nanoparticles, and can be solution cast to make electroluminescent thin film devices. The concept is further modified for synthesis of metal nanoparticles on polyelectrolyte templates with isolated beaded morphology.

Acknowledgement

The successful completion of this work has been a wonderful learning experience for me. The encouragement, guidance and help I have received from my colleagues and professors has been vital for achieving the results and focusing the efforts in right direction.

My everlasting respect and gratitude to Dr. Saraf for providing this opportunity and guiding me throughout the course. Our constant discussions on and off the subject, with or without agreement, observation of his hard work and the freedom in research I had during this study have shaped my views and have given me the motivation to pursue science as a career.

I am grateful to Dr. Cox, Dr. Wilkes, Dr. Davis and Dr. Esker for their support during this work. Their guidance has helped me understand the critical aspects of this work and channel the efforts in right direction. My sincere regards to Dr. Cox for the extra responsibility he accepted in allowing me to graduate from Virginia Tech.

My appreciation for the help provided by Michael Vaught and Riley Chan at Virginia Tech., Chemical Engineering and Leonard Akert at University of Nebraska Lincoln, Chemical Engineering with assembly and fabrication of instruments.

I am thankful to, Dr. Shivakumara as a mentor for synthesis of nanoparticles, Dr. Selim Elhadj and Dr. Subrata Kundu for numerous discussions and help in my queries during this project, and the often coffee breaks I enjoyed with Selim.

My group members Dr. Sanjun Niu, Dr. Rajender Gil, Gaurav Singh, Vikas Berry, Ravi Shenoy, Arvind Bhatt and Jennifer Kane have provided ever-ready and unending support in both academic and off the lab adventures. Specifically, Mr. Singh for his patience and part in our adventurous activities, he survives despite all attempts. They have made these five years appear short.

I owe this accomplishment to Shikhali, my wife, our daughter Vibha for being her and our parents the source of our motivation and guidance.

Table of contents

List of Figures

List of tables

Literature review

1.1 Nanotechnology

Research in the field of nanotechnology is fueled by the possibility of tailoring the fundamental properties of materials with simplification of processing and assembly of devices. The change in properties arises from quantum confinement effects, where the properties of a material become size dependent. The limited number of atoms/molecules in a nanoscale material compared to the bulk state and its nanoscale dimension lead to a strong effect of size, geometry and composition on its physical and chemical properties. Manipulation of composition, environment, geometry and size of a nanoscale material provide an avenue to tailor its properties. Phenomena observed in these systems include altered electro-optical properties like enhanced photoluminescence and absorption, transformation of continuous energy states to discreet ones, enhanced effects from single electron charging and tunneling, catalytic activity, sensitivity to surface layer and environment. The ability to tailor fundamental electro-optical properties and organization by self-assembly displayed by these materials, coupled with the drive for miniaturization of electronic devices has led to increased efforts in the field of nanoelectronics.

The thesis starts by introducing a plan for the self-assembly of a tunneling based electro-optical device composed of nanoparticles and polyelectrolyte, together with a literature review and a brief on the motivation for this project. The device functions as an electro-optical tactile sensor: electronic skin. The assembly and characterization of a device is presented in the final section.

Critical components for the device are nanoparticles and polyelectrolytes. The functioning of the device is based on electron tunneling. The device response is characterized by both the measured current and emitted electroluminescence. An abbreviated review on properties of nanoscale systems with emphasis on aspects and components central to device assembly and function is presented in the next section.

Nanoscale systems and their properties

Important characteristics

Nanoscale materials that have been widely investigated for their properties and application include: 0-dimensional system (0-D) of nanoparticles (NPs), 1-D system of nanorods and nanotubes, biological polymers like deoxyribonucleic acid (DNA) and proteins, thin polymer films, polyelectrolytes (PE), nanocomposites, and organic-inorganic hybrid structures. These systems have nanoscale dimensions with large surface area to volume ratio, important in the following aspects:

1. Reducing dimensionality changes the electronic properties, with decreasing size the density of states and spatial length scale of electronic motion are reduced. The transformation from continuous to discreet energy states, observance of coulomb blockade, and size dependent bandgap in semiconductors are manifestation of reduced size effects. The small volume of these materials makes them sensitive to changes in their composition.
2. Large surface area compared to small size provides a large interaction interface for these materials. The result is sensitivity of their properties to

chemical and physical environment. Examples of this include sensitivity of nanoparticle properties like photoluminescence to surface ligands and chemical environment.

3. Small size and large surface area leads to strong influence of forces like van-der-Waals bonding, hydrogen bonding, columbic interaction and surface tension on these systems resulting in their unique physical characteristics, like self-assembly, morphology and sensitivity to environment.

Decreasing size in nanoparticles leads to a more intense photoluminescence (PL) as shown in Fig. 1 for cadmium sulfide (CdS). The effect is due to stronger quantum confinement which increases the efficiency of radiative decay for the excited electrons*.

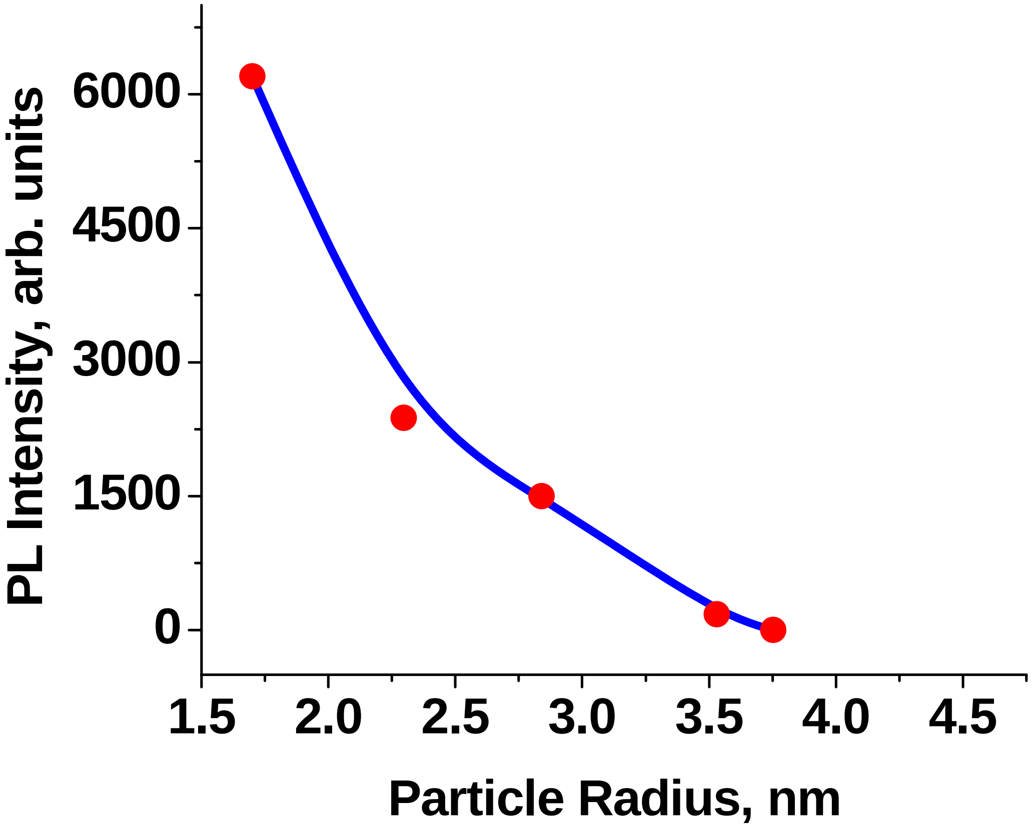

Figure 1. The effect of size on CdS nanoparticle photoluminescence. Smaller size leads to stronger quantum confinement resulting in increased photoluminescence

---

[*] V. Maheshwari, S. Shivakumara and R. Saraf, *unpublished work*.

The nanoscale volume also makes the band structure (electronic property) sensitive to doping with other elements. Shown in Fig. 2, composite nanoparticles of Cd/ZnS show a continuous shift in their photoluminescence spectrum resulting from the change in their band structure*. The photoluminescence spectrum shifts from 400 nm for pure ZnS to 537 nm for pure CdS in a continuous fashion based on their relative concentration in the nanoparticle. The photoluminescence emission hence can be tailored to desired characteristic wavelength by varying the composition.

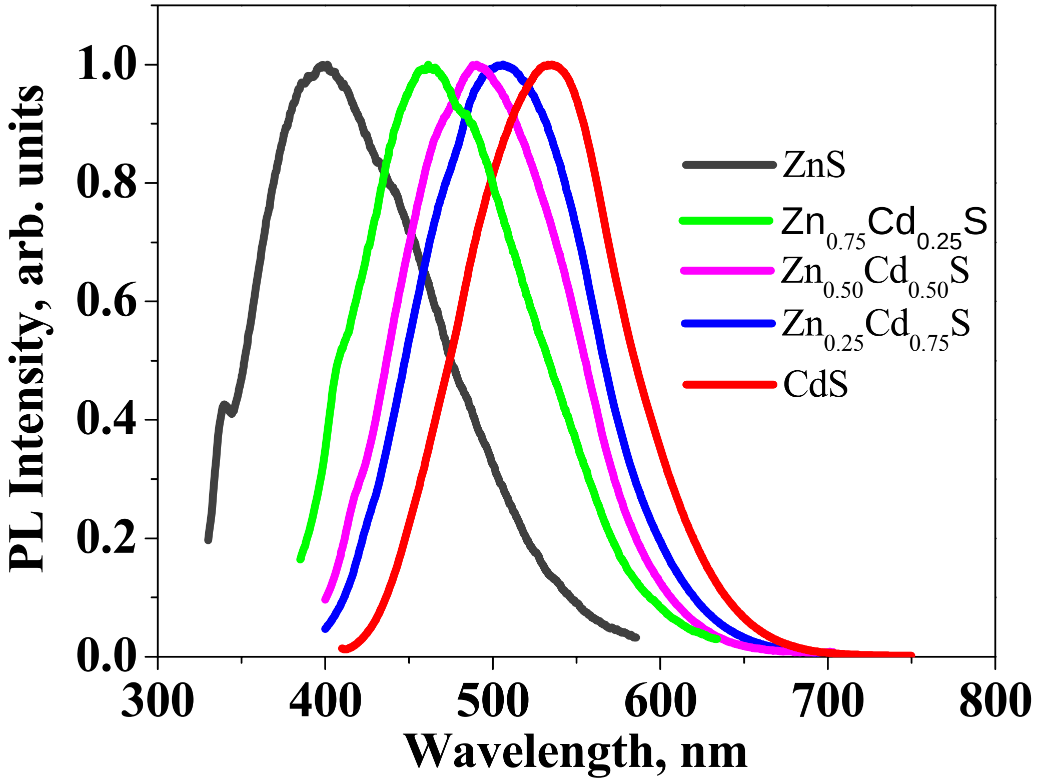

Figure 2. The effect of composition on Cd/ZnS nanoparticle photoluminescence. The photoluminescence wavelength shifts based on their composition, from 400 nm to 537 nm. The intensity has been normalized for better visualization on the graph.

Electro-optical properties of NPs like photoluminescence and absorption are sensitive to surface ligands and pH of solution. Due to their small size and enhanced

---

* V. Maheshwari, S. Shivakumara and R. Saraf, *unpublished work*.

photoluminescence compared to bulk, NPs are also used as biological tags in hybridization of DNA and staining of cells for imaging.

In polyelectrolytes their deposition on substrates and morphology in solution is highly sensitive to ionic strength, pH, concentration and solvency. The control on morphology is used for mineralization and assembly of NPs and wires. Polyelectrolyte vesicles are fabricated as drug delivery systems, where the drug is released on changes to pH and ionic strength of solution.

Self-assembly observed in these systems is a manifestation of high surface to volume ratio i.e. large interface with a small size. Commonly observed self-assembly processes are: the layer-by-layer (l-b-l) assembly of oppositely charged polyelectrolytes, hybrid polyelectrolyte-NPs structures, linear assembly of NPs by dipole-dipole interaction, core-shell structures in amphiphiles and block-copolymers. These have been widely used for fabrication of hybrid structures consisting of polyelectrolytes, NPs and organic dyes, and their applications have been shown in solar cells, interparticle tunneling for spintronics, biomemtic structures similar to bones and shells, memory devices and humidity sensors.

Electron tunneling

The core working principle of the proposed device is electron tunneling, a quantum mechanical phenomenon observed ubiquitously in electronic nanodevices. In tunneling, electrons (e^-) have a finite probability of crossing thorough an energy barrier. The probability of tunneling is always non-zero irrespective of the barrier magnitude (energy) and its width. A simple illustration of Fig. 3. shows an electron confined in a potential well can tunnel through a separating energy barrier, and crossover to another potential well. Tunneling is the direct result of treating electrons as a quantum mechanical particle with analysis based on the Schrödinger wave equation, hence electron with wave-particle duality. The wavefunction of the electron extends into the barrier, allowing it to tunnel across it to the next potential well. Probability of tunneling decays exponentially with the magnitude and the width of the energy barrier. Tunneling assemblies consist of conductors/electrodes separated by a dielectric medium (energy barrier), the impetus for tunneling results from the applied bias to the assembly and the response is measured as current in the system. Observed tunneling effects and applications include the electron gun of a field emission scanning electron microscope (FESEM), enzyme activity and kinetics based on electron transfer reactions, charge delocalization in polymer molecules like DNA and scanning tunneling electron microscope (STM). Tunneling devices have been assembled as memory elements by using a dielectric medium (i.e. the barrier energy) with properties sensitive to electric field strengths. Humidity sensors based on tunneling have been demonstrated which function by altering the tunneling distance due to changes in humidity.

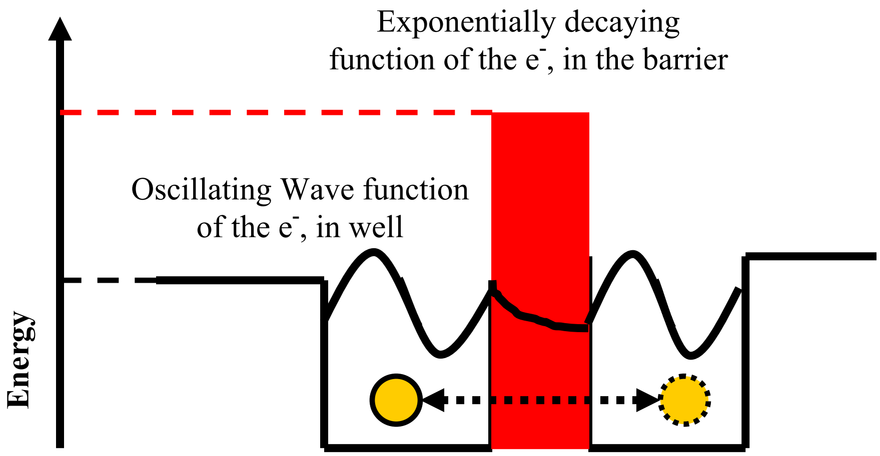

Figure 3. Electron tunneling between two energy wells, separated by a high energy barrier. The wave function of the electron extends in the barrier and results in tunneling of the electron to the other well

1.2 Research an 'electro-optical device: tactile sensor'

The goal is to develop a large area tunneling device with assembly of NPs and PE to sensitively capture the changes in local strain. Changes in strain from applied stress will result in modulation of the tunneling barrier width, the PE layers; this will be expressed in tunneling current, the measured output. As strain is directly proportional to stress, the sensitivity to strain will enable the measurement of stress variations. The motive is to present this as an ELECTRONIC SKIN, providing the sensation of touch.

Sense of touch: introduction and design challenges

The sensation of touch, one of our five basic senses, is primarily the determination of stress distribution over the area of physical contact between skin and the object surface.[1] Skin, with an average area of 1.8 m^2 is the largest of sensory interfaces and complements our vision and sound enabling us to interact our with surroundings. It gives us the ability to feel: sense texture and compliance of surfaces by touch. Artificial skin in the same capacity with application as an interface is a critical component to advance noninvasive surgical procedures which for example give surgeons the "touch sensation"[2-6] to decipher cancer tissue[5] and gallstone[3]; develop humanoid robots[7,8] that can sense shapes,[9,10] textures,[11,12] hardness[13] and manipulate complex objects,[10] which are not readily possible by vision alone. Currently touch (or tactile) sensors are usually made as a micro-electromechanical system composed of micro-machined deformable components[14] or by integrating strain sensitive materials, such as magneto-resistive ceramics,[15] piezoelectric polymers,[16,17] and strain sensitive conducting elastomers.[18] However, for large area devices, ~1 cm^2 or larger, the spatial resolution for stress distribution is, at best, in the ~2 mm range[18] compared to the ~40 µm on the surface of a human finger.[19] The height resolution for a human finger is ~2 µm[20] and the sensitivity or minimum stress that a human finger applies to sense texture and shape is ~ 10-40 KPa.[21]

The motivation is to achieve a performance comparable to human skin for the proposed electronic skin, the optimism to achieve this arises from the exponential sensitivity of tunneling to modulation of strain, hence the stress.

Design and working principle

A nanoparticle based tunneling device works on the principle that current through it is exponentially sensitive to the magnitude of energy barrier between the NPs and the physical distance between them. Hence the current can be modulated by increasing the electric field (voltage bias) across the NPs, which increases the energy of the electrons and hence lowers the energy barrier or by decreasing the barrier width by reducing the separation between the NPs. Thus, by applying stress we can reduce the physical separation between NPs, resulting in modulation of tunneling current. Further the device needs to be large-area and flexible with ease of assembly to function effectively as an artificial skin. To achieve high spatial resolution the device needs to have a discrete pixilated structure, with each pixel unit responding to the local stress profile.

The structure of the device that accomplishes this goal consists of the following characteristics:

1. To achieve tunneling between physically separated conductors with sensitivity to modulation of their separation distance, assembly of multiple layers of conductors each separated from the other by a thin dielectric barrier layer with thickness in nanometers will be fabricated. The layered structure will be assembled using the well known layer-by-layer self assembly method, l-b-l is a robust method to deposit desired number of nanometer thin layers of polyelectrolytes on a large area substrate. Results from characterization of the device suggest that the dielectric layer thickness should be less than 10 nm to achieve measurable response in current with applied bias in the range of 10-30 volts (V). The magnitude of current should be high for two reasons: (a) For accurate measurement using standard current meters, i.e. sensitivity to stress levels applied by human fingers. (b) The absolute variation in current to changes in local stresses should be large enough to be registered with the current meter, i.e. resolution of the device in measuring stress modulation.
2. A nanoparticle layered structure will lead to a discreet configuration of the device with current in each unit i.e. nanoparticle, modulated by the local stress profile. Discreetness in structure will enable the measurement of stress distribution from the current map of the device, with high resolution (benchmark is human skin). Dimensions of the units will determine the resolution of the device in measuring the stress profile. Hence we plan to fabricate each conductor layer as a self-assembled layer of nanoparticles, providing the necessary discreetness to obtain the mapping and resolution in stress profile.

3. The spatial resolution of skin is ~ 30-40 μm. The current will be measured by electrodes placed on the device, therefore for fast read out and mapping they will have to be patterned with a comparable resolution. However since our device is composed of NPs, theoretically its resolution can be in the nanometer range. Two issues are posed by this: (a) Patterning of electrodes will require lithography and a read out system with fast through put and accuracy, to measure and map the current response to applied stress profile. A significant technological and cost requirement is placed to achieve this, as for a 1”x1” device with a 40 μm resolution the required electrode will have 180,000 patterned discrete cells with an electronic system for their read out. (b) The true resolution of the device will be limited by the size of the electrodes. To over-come this challenge we plan to introduce layers of semi-conducting NPs in the device, these will function both as a conducting tunneling layer and emit light in response to conduction of current, a phenomena known as electroluminescence (EL). EL in the visible spectrum occurs due to the combination of electron current (in the conduction band) and hole current (in the valence band). EL is observed for semi-conductor NPs with a bandgap in the visible region. The phenomenon is similar to photoluminescence, the emission of light when electrons excited to the conduction band on absorption of photons decay back to the valence band by emitting a photon. For EL, the emitted light intensity is proportional to the magnitude of current passing through the NPs and is determined by the magnitude of the limiting current (hole or electron). The proposed architecture will allow the measurement of the device response from both current mapping and by imaging of the emitted light, i.e. EL.

A CCD can be used to directly image the light profile from the device in response to the applied stress distribution giving us a corresponding stress image.

4. Mineralization of NPs directly on PE chains will simplify the assembly of the device, resulting in a single step deposition process for the device. The mineralization process will be critically determined by the morphology of PE chains in solution, and hence an understanding of both the morphology and factors influencing it is required to successfully accomplish the NP mineralization.

The structure of the device as detailed is presented in Fig. 4 below. It consists of alternating conducting layers of metallic gold (Au) nanoparticles and semiconducting CdS nanoparticles. The layers of NPs are separated by a thin dielectric barrier (5-12nm), made of polyelectrolyte layers.

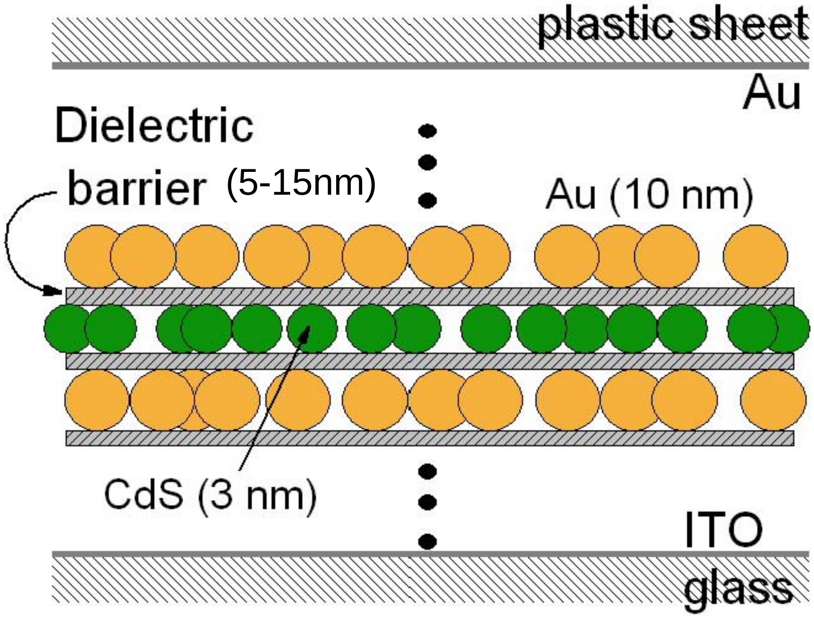

Figure 4. Schematic of the proposed architecture for the device. Metallic (Au) and semiconducting (CdS) nanoparticle assembled in structured layers separated by a dielectric barrier.

The critical components for assembly of the device with proposed architecture and its functioning are as follows:

1. The synthesis, characterization and assembly of metallic (Au) and semiconducting (CdS) nanoparticles, in the proposed device architecture. Specifically synthesis of CdS NPs is performed, while for Au NPs a standard product, commercial sources are used. In this regard it is necessary to develop an understanding of the principles for synthesis and methods for characterization of both metallic and semi-conducting nanoparticles.
2. For assembly of NPs in the device architecture of layers with each separated from the other by a thin dielectric barrier, the l-b-l assembly of polyelectrolytes is used. l-b-l will be used both to deposit the NPs and to develop the dielectric barrier with controllable thickness. An understanding of the principles for l-b-l assembly, with emphasis on the factors controlling the interaction of PE with its surrounding, leading to their assembly, morphology and coverage of deposition is required to assemble the device structure.
3. The device is based on electron tunneling, with NP layers functioning as the conducting moieties and layers of PE functioning as the barrier. The optimization of performance in terms of current and EL response of the device will require an understanding of the principle of tunneling and the parameters controlling its response.
4. Finally testing of the device is performed with measurement of current and EL in response to applied bias and loading. The characterization was performed on a home built set-up that can apply bias voltage to the device under controlled

loading, and measure the response by monitoring the current and electroluminescence.

Presented is a sequential review on each of these aspects for device assembly and characterization.

1.3 Tunneling

A core concept of quantum mechanics is the wave-particle duality, which presents the treatment of matter as both particles and waves to develop a theoretical understanding of their properties. The correlation between this duality is given by the De Broglie relationship which relates the momentum of a particle to its wavelength:[22]

$$\lambda = h/p$$

Where λ, is the wavelength of particle, h, is the Plank's constant and has a value of 6.626068×10^{-34} m^2 kg/s and p, is the momentum of the particle

Besides atomic and sub-atomic particles like electrons, neutrons, dimers and small clusters, recently fullerene molecules with their size of 1 nm (order of magnitude larger than atomic particles) exhibited the wave-particle duality.[23] The concept of duality in behavior is also exhibited by electrons which results in their ability to tunnel through an energy barrier, behaving as waves. Curiously, the phenomenon of tunneling was first developed to explain the alpha decay of a radioactive nucleus in 1928.[24]

Consider the quantum mechanical problem of a particle tunneling through an energy barrier (see Fig. 5). The behavior of the particle as a quantum mechanical object is governed by invoking the Schrödinger equation,[22] the fundamental equation which predicts the evolution and behavior of quantum mechanical systems. The particle by this equation is characterized by its wavefunction ψ(r,t), and its probability density at any point in space is given by $|\psi|^2$. Hence it has both the wave (wavefunction) and particle nature (probability density).

The time independent Schrödinger equation is:

$$\frac{d^2}{dx^2}\Psi(x) = \frac{2m}{\hbar^2}\left((V(x)-E)\Psi(x)\right) \tag{1}$$

for the case of tunneling through an energy barrier as shown below,

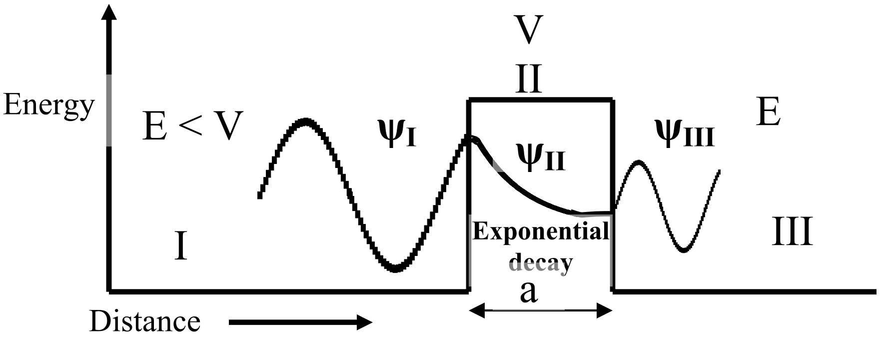

Figure 5. Schematic of an electron tunneling thorough an energy barrier. The electron in region I and III has purely kinetic energy, E. The regions are separated by a barrier with potential energy of V, V>E. The width of the barrier is 'a'.

The particle in region I and III has purely kinetic energy E, these regions are separated by an energy barrier, II of width 'a' and potential energy V, V > E. The solution of the Schrödinger equation for the system with the particle in region I results in an oscillating wavefunction for the particle in region I and III, and an exponentially decaying wavefunction in the barrier, II. The probability of particle tunneling to region

III is characterized by the transmission coefficient (T), the ratio of probability density function corresponding to its wavefunction in these regions, ψ_{III} and ψ_I,

$$T = {|\Psi_{III}|^2} \big/ {|\Psi_I|^2} \tag{2}$$

$$T = 1 \big/ \left(1 + D\sinh^2(\alpha a)\right) \tag{3}$$

$$D = V^2 \big/ 4E(V - E) \tag{4}$$

$$\alpha = 8\Pi m(V - E) \big/ h^2$$

m is the mass of the particle.

For aα >> 1 we have

$$T = T_o \exp(-2a\alpha) \tag{5}$$

$$T_o = 16E(V - E)/V^2 \tag{6}$$

The phenomenon described above resulting in a finite probability for the particle crossing through a higher energy barrier is tunneling. The finite probability arises as the particle wavefunction extends in the high energy barrier region. It depends exponentially on the width, a, of the barrier and the magnitude of the barrier energy relative to particle energy (V-E). The solution discussed above is for the case of pure tunneling.

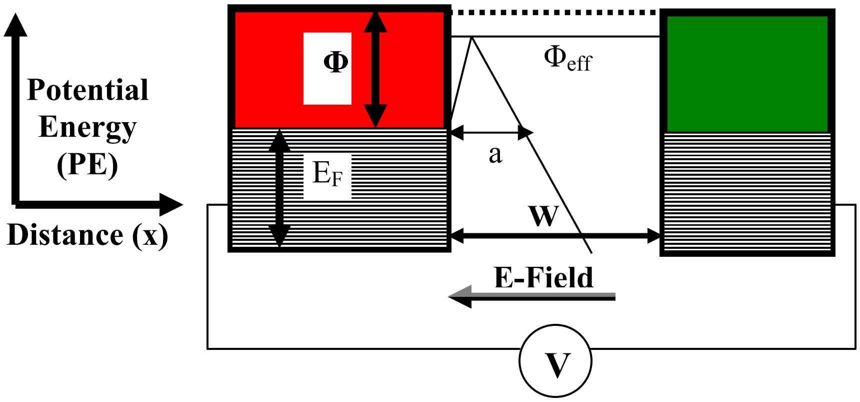

Figure 6. Two metal surfaces with Fermi energy E_F and ionization potential Φ, separated by a vacuum barrier of width W. The metal surfaces are biased by a voltage V, resulting in a uniform field in the barrier.

Consider the case of electrons tunneling between separated metal electrodes with an applied bias, Fig. 6. For the case of electrons in a metal, their energy is the Fermi energy (E_F) and outside in vacuum it is $E_F + \Phi$ (Φ, ionization potential of the metal). Hence the energy barrier for the electrons to leave the metal surface is Φ (neglecting the space charge developed on the metal surface when it is ionized). In the presence of an external electric field and considering the contribution from image charges on the metal surface, its vacuum energy is modified to

$$PE(x) = E_F + \Phi - e^2/(16\Pi\varepsilon_o x) - exE \qquad (7)$$

Here $e^2/(16\Pi\varepsilon_o x)$ is the contribution from image charges, exE is the potential energy (PE) of electron in external electric field E, e is the charge on electron, ε_o is the dielectric constant of vacuum and x is the distance along the line of separation between the two metal surfaces.

Solving the equation for maximum in PE(x) we get the effective barrier height Φ_{eff}[22] as

$\Phi_{eff} = \Phi - [e^3E/(4\Pi\varepsilon_o)]^{1/2}$ (8)

and the barrier width as

$a = \Phi/(eE)$ (9)

The tunneling probability for the electron is given by:

$P = K\exp(-E_c/E)$ (10)

here, $E_c = [8\Pi(2m\Phi_{eff})^{1/2}\,\Phi]/(eh)$ is defined as the critical field for tunneling and K is a constant. The tunneling current density is then given by[22]

$J = A_o\exp(-E_c/E)$ (11)

here, A_o is the total electron density or pathways for tunneling. A more rigorous analysis gives the tunneling current as

$J = A_oV^2\exp(-E_c/E)$ (12)

Equation (12) is the classical Fowler-Nordheim equation for tunneling.[25] The tunneling characteristics of a device should be governed by this equation. The current flow through the device will be the result of electrons tunneling sequentially through each dielectric barrier with the adjacent layers of NPs acting as the potential wells (see Fig. 7).

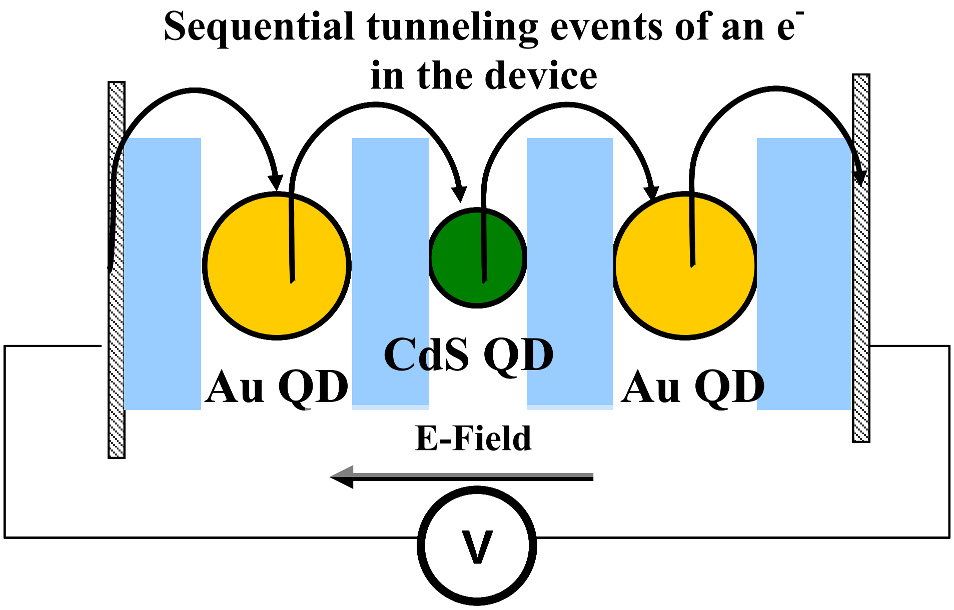

Figure 7. Schematic of sequential tunneling events thorough layers of NPs separated by dielectric barriers of PE layers. External electric field results from the applied bias V. The electron tunnels through the PE layers from one NP to next, resulting in flow of current.

The ability of the electron to leave the metal surface depends on the magnitude of the energy barrier and the ionization potential Φ. In tunneling, since the phenomenon is with an electron of lower energy, the width for tunneling is equally important. In the case of thermionic emission (TIE) of electrons from the metal surface, the thermal energy (kT, k is the Boltzmann's constant) of the electrons becomes greater than the barrier, allowing them to escape from the surface. Unlike tunneling, in thermionic emission the electron leaves the surface only when its thermal energy is greater or equal to Φ. The probability in thermionic emission is given by

$P(KT) = B_oT^2\exp(-\Phi/kT)$ (thermionic emission equation) (13)

The equation results from considering the Boltzman energy distribution of electrons in a metal as a function of temperature. The distribution gives the probability of having electrons with energy greater than ionization potential Φ, as these will be the one that will escape the metal surface.

Similar to the case of tunneling, in thermionic emission also the presence of an external electric field reduces the effective energy barrier for tunneling to Φ_{eff}; this is known as the field assisted thermionic emission (FATE). The modified equation for FATE is[24]

$$P(kT) = B_oT^2\exp(-\Phi_{eff}/kT) \qquad (14)$$

The equation presents the dependence of emission of electrons on both temperature and applied electric field. There is a possibility of current in the device being governed by FATE rather than just tunneling.

Tunneling applications include the scanning tunneling microscope[26] (STM) and FESEM. Devices have been fabricated which exploit the sensitivity of tunneling to barrier properties; these include memory storage media,[27] tactile sensors[28] and humidity sensors.[29] Charge transfer along DNA chains resulting from the hopping of electrons and holes between bases, is a tunneling phenomena.[30,31] Enzyme reaction pathways have a critical electron transfer step which are a result of tunneling of electrons between molecules.[32,33] Active sites on catalysts investigated by STM reveal that local changes in electronic structure alter the tunneling characteristics resulting in their catalytic activity.[34,35] Tunneling is also the working principle for the tactile device with its sensitivity arising from the exponential dependence of tunneling on the magnitude of barrier energy and its width.

1.4 Polyelectrolyte: layer by layer assembly and mineralization

A layer by layer assembly process has been used to fabricate the composite device structure, with polyelectrolytes as the dielectric and semi-conducting and metallic NPs as the intermediate layers. The assembly process also provides the ability to control the thickness of the dielectric, i.e. separation between the tunneling layers with nanometer scale precession.

l-b-l is a widely used method for fabrication of uniform thin films of polyelectrolytes on charged surfaces. The films are made by alternating exposure of a charged substrate to a solution of polycation and polyanion polyelectrolytes. Each exposure deposits a reproducible quantity of polyelectrolyte on the surface and reverses the surface charge priming it for next cycle of deposition[36]. The thickness of each layer is in the sub-nanometer to nanometer range and can be controlled by the number of layers deposited, the ionic strength of PE solution and the solvent quality. The robustness of this process is the reproducibility of each cycle in the thickness of layer deposited, the ability to deposit multiple layers with no restriction in their numbers, no structural limit on the size of substrate for deposition making it ideal for large area device fabrication, deposition on geometric features like NPs,[37] spheres,[38] cubic crystals[39] and nanotubes[40].

Recent research on l-b-l assembly has focused on expanding the technique to include biopolymers like DNA and proteins[41], NPs[42-44], clay minerals[45], carbon nanotubes[40,46] and second harmonic generation with non-linear optical polyelectrolytes.[47] The structure of the film is completely determined by the sequence of deposition and the type of moiety used in the process, allowing the fabrication of hybrid structures with multiple species like the ones mentioned above and a well defined spatial morphology as determined by the sequence of deposition. The only restriction is for the moiety to be charged and in solution. The process has been used to assemble hybrid structures with layered architecture consisting of Au NPs and PE. The assembled composite films are mechanically robust to strain loading with structural integrity. The films can be floated and transferred to other surfaces while maintaining their structure.[48] Applications of the process have been demonstrated in the areas organic-inorganic hybrid structures,[45,49] membranes,[48] conducting layers,[50] drug delivery,[39,41] light emitting films[51] and enzyme active films.[52]

Multilayer films of polyelectrolytes are fabricated by their absorption on oppositely charged surface. A schematic of the process is presented in Fig. 8. Each exposure results in deposition of a thin layer of oppositely charged polyelectrolyte with charge reversal on the surface (each deposition step is followed by a washing step, not shown in Fig. 8.). Reversal of the charge is critical for depositing of the next layer. Unlike small molecules where each has to be bonded to the substrate, the use of polyelectrolytes is advantageous as adhesion of the depositing chains requires only a certain number of ionic bonds to the underlying substrate. The driving force for polyelectrolyte deposition on the substrate is the electrostatic attraction and the hydrophobic nature of polymer-polymer contact.[53-55]

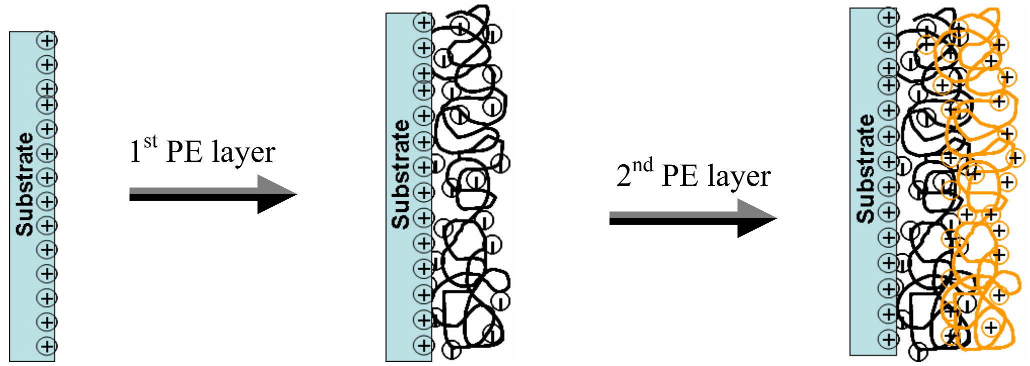

Positively charged surface

Exposure to anionic PE solution

Exposure to cationic PE solution

Figure 8. Deposition of oppositely charged PE on a charged surface by sequential exposure to PE solutions. Each exposure results in deposition of a PE layer with multiple bonding sites and a reversal of surface charge.

Structure of the polyelectrolyte multilayers

The PE layers are diffused in concentration with interpenetration up to 3-4 layers. The deposition of PE chains in diffused morphology with loops and dangling chains, allows the interpenetration, further since the chains are anchored by limited bonds to the surface, local rearrangement is possible to minimize inter-chain repulsion and maximize contact with oppositely charged PE chains.[36,54,56] The interpenetrated layer morphology has been determined by neutron scattering and X-ray reflectivity.[36,56]

The reversal of surface charge by the next depositing PE layer is critical for continuity of deposition, and is achieved by the electrostatic attraction between the layers and the hydrophobic interactions between the PE chains. The local rearrangement of the PE chains mentioned above also helps to minimize electrostatic interaction between the intra-layer chains. The limit of deposition in each layer is reached when electrostatic repulsion and steric hindrance with the already deposited PE limit further chains from solution to adhere to surface. The initial 3-4 layers of PE on the substrate act to stabilize the charge density to an equilibrium value as determined by the PE layers rather than substrate charge density. After the charge density has reached initial equilibrium, the sequential deposition of PE results in linear increment in thickness of the film.[54]

Factors controlling the deposition of polyelectrolyte layers

The ionic strength / salt concentration have the greatest influence on the thickness of depositing PE layers. The concentration of solution (usually in the mM range), molecular weight of the PE, time for deposition (usually greater than 20 minutes) and drying steps after washing, do not influence the thicknesses of deposited layers appreciably. Increasing the salt concentration shields the electrostatic repulsion between the PE chains by charge compensation, leading to thicker layers. The thickness of the deposited layers increases linearly with salt concentration. The extent of the increase in thickness also depends on the counter ion of the salt used. The less hydrated ions bind more strongly to the PE chains resulting in increased shielding and thicker layers of deposition. The observation is seen for both cationic and anionic PE.[54] Extreme salt concentrations result in desorption of the PE layers, because of the shielding of electrostatic attraction between the PE layers deposited on the substrate.[54,56] An alternative for reducing the electrostatic repulsion between the PE chains is to make the solvent poor (more hydrophobic), which reduces the charge density on the PE chains due to lesser dissociation of the ionic groups along the PE chain.[54,57]

Mineralization: Introduction

The assembly process of the device can be simplified by incorporating the functionality of PE (dielectric) and NP layers in a single composite structure of NPs mineralized on PE chains. The composite structure will have the functionality of both, NPs, required as tunneling bases and the PE, as a dielectric tunneling barrier. The mineralization process will need to produce monodisperse NPs for efficient device performance. The underlying morphology of PE will critically govern the size and monodispersity of the NPs and their subsequent processing for device fabrication. Mineralization of semiconducting NPs on PE will be performed, this will subsequently be extend to Au NP mineralization and combining of the two processes for synthesis of a single hybrid structure consisting of both CdS and Au NPs and PE .

The exquisite control of mineralization mediated by macromolecules in nature[58,59] is an attractive bio-mimetic[60] process that has attracted great interest as an approach to synthesize nanostructures and concomitantly assemble them to make well formed micro/macro structures. In this process metal ions selectively saturate sites on the macromolecular template and are subsequently condensed forming a mineralized macrostructure. Organization of the structure is governed by morphology of the template and its interaction with the metal ions. Nanoparticles result from the nanoscale morphology of the template and their relative concentration. Recently, polynucleotides,[61,62] proteins,[63] block copolymers,[64,65] polyelectrolytes,[66] amphiphiles[67,68] and lipids[69,70] have been shown as molecular scaffolds to mineralize and self-assemble nanoparticles into ordered lattices,[71,72] wires,[73-75] and helical ribbons.[76]

Polyelectrolyte: Morphology

The problem of a charged polyelectrolyte globule in a poor solvent can be treated on the lines of the classical problem of a charged droplet.[77] A charged water droplet in air disintegrates into smaller droplets when its charge exceeds a critical value (Q_{crit}). This critical value is determined by the balance of surface energy (S) and electrostatic energy (Ese). The surface energy and the electrostatic energy are given by:

$$S = 4\prod\gamma R^2 \quad (15)$$

$$Ese = Q^2/\varepsilon R \quad (16)$$

Balancing S and Ese, the Q_{crit} scales to $R^{3/2}$.

Since R is proportional to $N^{1/3}$(the number of molecules in droplet), Q_{crit} scales as $N^{1/2}$. Here γ is the surface tension, ε is the dielectric constant of the media, Q is the charge and R is the radius of the droplet. If the charge on the droplet exceeds Q_{crit} its energy equilibrium is a set of smaller droplets with a charge less than Q_{crit}.

In a similar manner for a charged polyelectrolyte chain in poor solvent its configuration is governed by the interaction between Ese, S and hydrophobic chain segments. The interaction transforms the chain from a single collapsed globule to smaller beads. Being on a chain, the beads are interconnected by chain segments, forming a 'Necklace of Beads'.[77-79] The morphology is schematically depicted in Fig. 9.

The morphology of PE is sensitive to the ionic strength, pH and the quality of solvent.[79-81] Increasing the ionic strength reduces the repulsion between the charged segments leading to more condensed morphology with larger beads. pH affects the morphology by altering the charge density along the PE chains. Acidic pH for a polycationic PE increases its charge density, increasing the segmental repulsion and the morphology transforms to a more extended configuration with smaller size beads. The solvent quality has a similar effect on PE: decreasing charge density as the hydrophobicity of solvent increases; the PE chains can then collapse to a more compact structure, resulting in larger bead size which reduces hydrophobic interaction with the solvent.

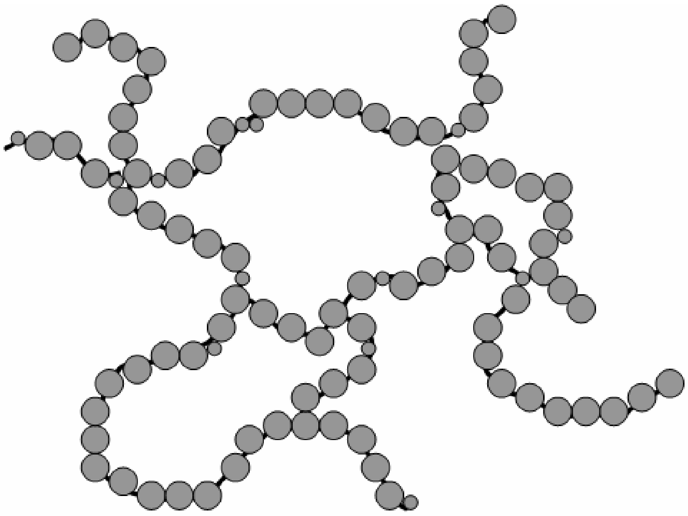

Figure 9. A schematic of a beaded chain morphology resulting from the electrostatic and the hydrophobic interactions between the chain segments and counter ion condensation.

PE morphology in solution is critical for applications involving solution processing which include l-b-l deposition, mineralization and self-assembly of NPs and nanowires. The beaded chain morphology is used to achieve NP mineralization yielding monodisperse NPs on PE chains. The motivation is to simplify assembly of device from individual steps of PE and nanoparticle deposition to a single step with deposition of these hybrid multifunctional PE-nanoparticle composite.

1.5 Nanoparticles

Nanoparticles are spherically confined nanoscale materials with their electro-optical properties strongly dependent on their size (quantum size effects). Limited dimensionality of the material alters its electro-optical properties as the density of states and the spatial length scale for electronic motion are reduced as determined by the physical size of the material.[82-85] Bulk state is characterized in metals by overlapping valence and conduction bands partially filled with electrons, while semiconductors have filled valence band separated from an empty conduction band by a bandgap of energy E_g. The difference results in distinct properties for their respective NPs like luminescence, size dependent bandgap in semiconducting materials[82,84,85] and plasmon absorption for metallic NPs.[83] The difference in band structure leads to their distinct properties hence each is discussed separately to obtain a better understanding of their characteristics.

Semiconducting nanoparticles

Semiconductors with their bandgap (direct bandgap materials) in visible region of light spectrum are of interest as they emit visible light; hence their photoluminescence (and electroluminescence) is visible to human eye and can be imaged using a CCD, requiring no sensitivity in ultra-violet or infrared region. Group II-VI semiconductors such as cadmium sulfide (CdS), cadmium selinide (CdSe) and zinc sulfide (ZnS) with their E_g in visible region are widely used materials in this regard.[82,85,86]

Size effects

On irradiation of a semiconductor with light of energy hν > E_g, (h, Planck's constant; ν, frequency of light) an electron from the valence band (the highest occupied molecular orbital, HOMO) is excited to the conduction band (the lowest unoccupied molecular orbital, LUMO), leaving an electron vacancy in valence band. The vacancy behaves as a pseudo positively charged particle, hole and has the same charge as the electron and its own effective mass. The electron-hole pair (exciton) interacts, similar to a hydrogen atom and its spatial separation (Bhor radius, r_b) is given by the modified Bhor model as:

$$r_b = \varepsilon h^2/\Pi m_r e^2 \qquad (17)$$

Here r_b, is the Bhor radius, m_r, is the reduced electron-hole mass. Quantum size effects are observed when the size of NP become smaller than Bhor radius.[86,87] The result is confinement of the exciton, similar to the quantum mechanical problem of a particle in a box and the energy levels of exciton are given by

$$E_n = h^2n^2/(8mr^2) \qquad (18)$$

Here r, is the radius of the NP and E_n is the energy corresponding to quantum number n. The effective bandgap energy for NP is then given by the modified term

$$E_g = E_g\,(\text{bulk}) + h^2n^2/(8m_r r^2) - 1.8e^2/(4\Pi\varepsilon r) \qquad (19)$$

The last term is the columbic attraction between the electron-hole pair in the material. The equation describes the effect of size on the bandgap (bg) for semiconducting NPs, the bg energy increases as $1/r^2$ from the confinement of the exciton and decreases as 1/r from the electrostatic attraction term. For strong confinement $r < r_b$ the $1/r^2$ term dominates leading to a rapid increase in $E_{g.}$[86,87] The plot of E_g as a function of size for cadmium sulfide NPs is present in Fig. 10, as simulated from equation (19), a rapid increase in E_g due to quantum confinement is observed below the Bhor radius, 5 nm for CdS.

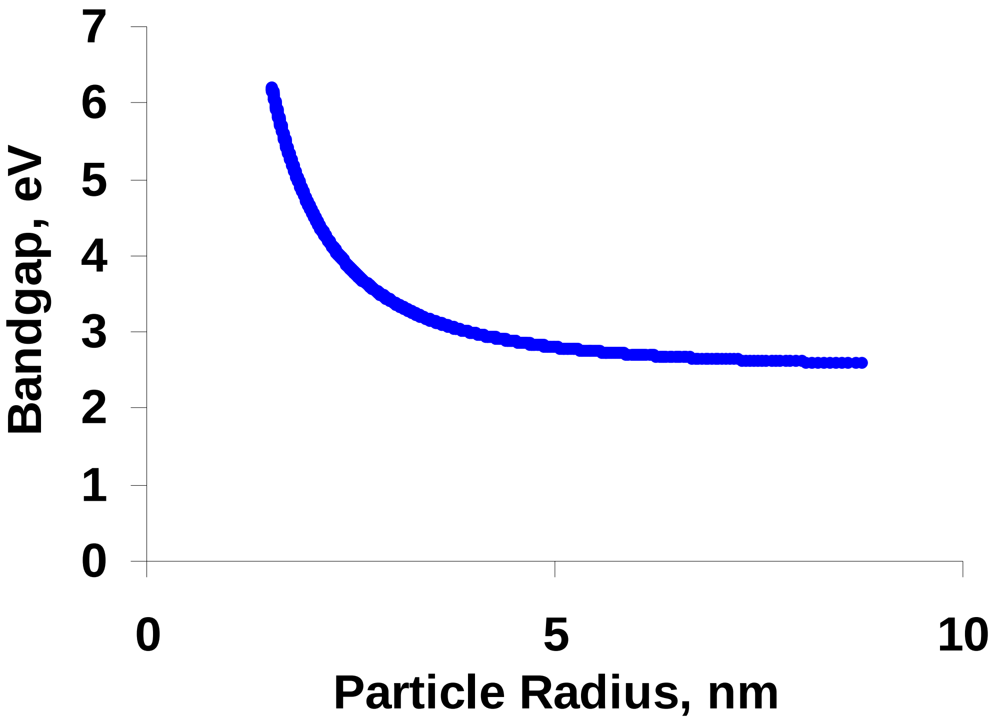

Figure 10. The increase in bandgap as a function of size for CdS as predicted from equation 19. Below the Bhor radius of 5 nm, we observe the quantum size effects of increasing E_g with decreasing size.

The observed effect of the increase in E_g is blue shifting of the absorption and emission spectra for NP with decreasing size, as predicted by equation 19. The shift in E_g allows the control of luminescence spectra based on size of NP (Fig. 10).[82,88,89] Further due to strong coupling of exciton, the strength of absorption and quantum efficiency of emission in NP is higher than bulk state material.[87,90] The bandgap structure of NPs is also critically determined by their composition due to their nanoscale volume, small amount of doping elements can alter their bandgap structure significantly changing the E_g

and the luminescence characteristics.[82,91] Examples include doping with manganese, europium, synthesis of compound NPs like zinc/cadmium sulfide. In comparison to organic dyes NPs have reduced bleaching because of their stable crystalline structure, making them attractive bio-labels for imaging and tagging.[88,92,93]

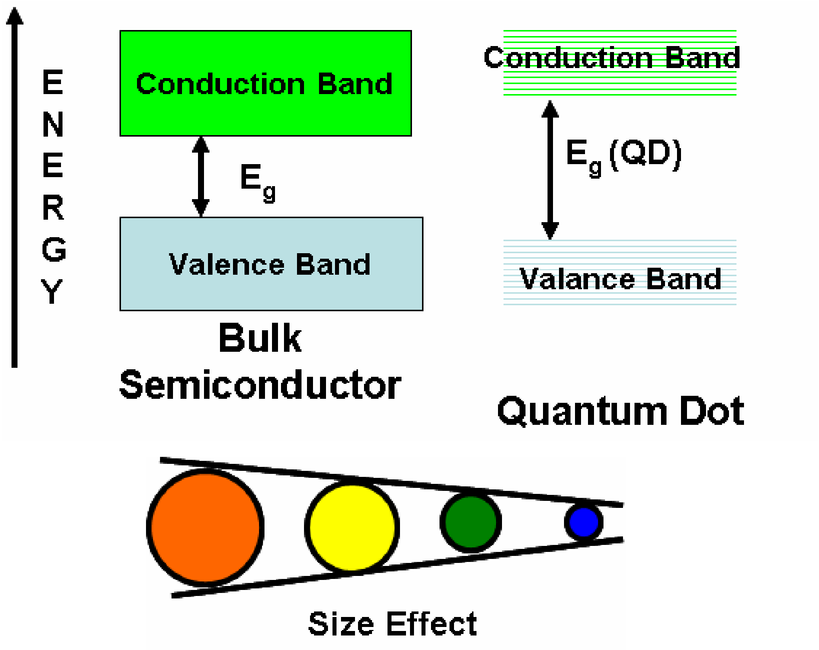

Figure 11. The blue shift in bandgap energy E_g from the bulk state to NP and the effect of size on NP emission characteristics.

Synthesis routes for semiconducting nanoparticles

The common routes for synthesis use variety of bottom-up approaches for controlling and confining the size of NPs. The synthesized NPs should be crystalline with high purity and monodispersity to achieve high quality of response in applications. Control over these parameters is important for NPs as their properties are sensitive to composition and size, critically determining their response in applications. Capping agents are commonly used to arrest their growth and stabilize them from aggregation.

Thiols with their affinity for Cd and Zn are widely used as capping agents, solution of Cd^{2+} in presence of thiol (RS^-) reacted with sulfur source like Na_2S, results in formation of thiol capped NPs. The ratio of thiol to Cd/Zn determines the size of NPs and their functionality can be controlled by the functional group (R) on thiol.[94,95]

Synthesis in nanoscale restricted environment like reverse micelles, membranes, zeolites and glasses also results in NPs with their size and distribution determined by the synthesis environment.[96-99] Particularly reverse micelles have been widely investigated due to wide variety of available systems (eg. AOT) and their functionality. The size is controlled by the ratio of surfactant to water, as this determines the number and size of micelles and hence the concentration of reactants present in them for formation of NPs.

Highly monodisperse and crystalline NPs are synthesized by using organometallic precursors in a coordinating solvent which also acts as the surfactant. The method requires high temperature (200°C – 300°C) and an inert atmosphere. The NPs are formed by nucleation of seeds which can be grown to desired sizes by controlling the time and temperature of reaction. A variety of NPs CdE (E= S, Se, Te) have been synthesized by this method, yielding high quality product and with the ability to synthesize large quantity of NPs.[100] The method has been further extended to yield shapes and morphologies like core shell NPs, nanorods, tripods, and triangles.[101-103] Synthesis of core-shell structures, with a high dielectric layer (eg. ZnS) covering the core NP (CdSe) results in impassivation of the core surface to surface effects.[82,91] The high dielectric shell renders them robust to changes in environment as the exciton is restricted to the core and does not interact with the surrounding, this results in high quantum efficiencies for luminescence and reduces bleaching. The core-shell structure is also critical for retaining their high luminescence through further modifications of the surface layer with bio-molecules for biocompatibility, and on exposure to pH and ionic strength changes in biological systems.[88,89,104]

Mineralization on morphological assemblies of polynucleotides, proteins, block copolymers, polyelectrolytes, amphiphiles, bacterial membranes and lipids has been used to synthesize and structure NPs[66-68,75,76] into ordered lattices, wires, and helical ribbons.[45,66,76,105] The process leads to a single step synthesis and assembly of NPs and has generated interest due to its bio-mimetic nature with ability to assembly inorganic-organic hybrid structures similar to bones and shells. Monodispersity in NP size distribution in these processes is yet to be achieved.

Semiconducting nanoparticle applications

NPs find applications in variety of fields due to their characteristics of photoluminescence, electroluminescence and effective control of absorption and emission color by size and doping. They have been used as labels for staining of cells by modifying their surface with biological target molecules like proteins.[93,104] NPs with different sizes modified with target DNAs have been used as color labels in hybridization of DNA.[62,106] They have also been used with organic dyes and in conducting polymers to assemble solar cells,[107] lasers,[108] multi color emission LEDs and electroluminescent devices.[109-114]

The nanoscale size of particles results in a very small capacitance ($C= 4\varepsilon\varepsilon_o\Pi r$) for them, which leads to high energy for charging each electron to the NP (equation (20)).[115] Hence observation of quantization of electron charging is possible in NPs.

$$E = e^2/C \tag{20}$$

The effects are observed for $E > 100$ kT.

Here r, is the radius of the particle, e is the electron charge, ε is the relative dielectric constant of the particle, ε_o is the dielectric constant of vacuum, T is the temperature and E is the charging energy.

Quantization of charging energy has been used for demonstrating single electron transistor using a NP.[116-118] Further due to the prominent observation of tunneling at these scales spintronic devices have been demonstrated with NPs.[117,119-121]

In summary, the attraction in use of semiconducting NPs lies in their luminescence properties which allow control on their color of emission by varying the size and composition. Their small scale size leads to observable size quantization effects like increase in E_g, quantization of charging energy, tunneling and self-assembly using physical and chemical interactions.

Gold nanoparticles

Metallic NPs have long been studied due to their colorful colloidal solutions. Their quantum confinement results in observance of size effects like quantization of charging states, high surface area results in improved catalytic activity and appearance of size dependent plasmon absorption results in their unique color. Metallic NPs are different from semiconducting NPs due to their band structure which does not have the energy separation, bandgap (E_g) between valence and conduction band states required for photoluminescence.

Gold NPs in particular have been used as pigments since the 17th century in glass due to their wine-red color; this observance of color in NPs arises from their plasmon absorption. The phenomenon was explained by Mie theory, solving the Maxwell's equation for absorption and scattering of electromagnetic radiation by spherical particles.[83] For NPs much smaller than the wavelength of absorption the extinction coefficient κ, for N particles of volume V is given by

$$\kappa = \left[\left(18\Pi N V \varepsilon_m^{3/2}\right) \Big/ \lambda \right] \left(\varepsilon_2 \Big/ \left((\varepsilon_1 + 2\varepsilon_m)^2 + \varepsilon_2^{\,2} \right) \right) \qquad (21)$$

Here λ is the wavelength of absorbing light, ε_m, the dielectric constant of surrounding medium (assumed to be frequency independent) and ε_1 and ε_2 represent the real and imaginary parts of the frequency dependent dielectric function for the material. The condition of plasmon absorption is fulfilled when $\varepsilon_1(\omega) = -2\varepsilon_m$ where ω is the angular frequency of light.

The above formulation treats the dielectric function to be size independent with dipole approximation. For particles with sizes less than 20nm the dipole approximation is valid, but the bandwidth of absorption is observed to be inversely proportional to the size of NPs (size <20nm). The dependence arises from the dielectric function being size dependent.

Dielectric function of the electrons in NPs can be written as the sum of interband transition term $\varepsilon_{IB}(\omega)$ and the free electron response term $\varepsilon_D(\omega)$ (the Drude term). The Drude term is

$$\varepsilon_D(\omega) = 1 - \omega_p^2/(\omega^2 + i\gamma\omega) \qquad (22)$$

Here $\omega_p = [ne^2/(\varepsilon_o m_{eff})]$, n is the free electron density, e is the electron charge, ε_o is the permittivity of vacuum, m_{eff} is the effective electron mass and γ is a damping constant related to the lifetime of all electron scattering process: electron-electron, electron-phonon, electron-defect and electron-surface.

For a small particle (< 20 nm) the surface term dominates the scattering process and γ is given by

$$\gamma = \gamma_o + AV_f/r \tag{23}$$

Here γ_o is the bulk damping coefficient independent of surface scattering, V_f, is the velocity of electrons at Fermi level, A is a constant detailing the scattering process and r is the radius of particle.

The model correctly predicts the size dependence (1/r) of the bandwidth of absorption of NPs with size < 20 nm. At larger sizes the dipole approximation is no longer valid and higher order terms which are size dependent need to be considered, resulting in the size dependence of the plasmon absorption wavelength.[83]

Gold nanoparticle applications

Metallic NPs with observable quantum size effects are of great interest with possible applications in optical storage,[83,122] solar energy[107] and as catalyst due to high surface to volume ratios and tunneling sensitive surface states.[35,123] Au NPs, due to their nanoscale size, have also been coupled with biological systems to make bio-electronic devices.[28,124] Single electron charging effects are observed at room temperature in very small NPs (1-2 nm) due to very small capacitance ($4\Pi\varepsilon_o r$) resulting in high charging energy ($E = e^2/C$),>100kT. The high charging energy results in observance of coulomb blockade and oscillation which have been demonstrated as single electron transistors.[115,125] The plan is to use them as discreet metal moieties for conduction in the device, resulting in high resolution of current mapping to applied stress profile.

Tactile sensor[*]

2.1 Materials and synthesis

The three components critical for the assembly of device are:

1. Synthesis of water stabilized CdS nanoparticles with both anionic and cationic functionality. The NPs should be monodisperse in size distribution to ensure uniform deposition, discreetness in structure and invariability of device response with intense electroluminescence output.
2. Commercially available Au nanoparticles with anionic functionality are used for device assembly. The function of Au NPs is as discreet metallic moiety for tunneling of electrons (current).
3. Assembly of device components in the proposed architecture is accomplished by using the layer-by-layer assembly technique for deposition of PE.

Synthesis of anionic and cationic semiconducting nanoparticles

Cationic and anionic CdS NPs are synthesized using functionalized thiols as capping agents. Synthesis is performed in an aqueous medium at room temperature and under an inert nitrogen atmosphere (N_2).

The procedure is similar for anionic and cationic synthesis except for the functionality of capping thiol. For anionic NPs 3-mercaptopropionic acid (MPA), and for cationic NPs cysteamine hydrochloride (CSA), are used as capping agents. Characterization of NPs is performed by absorption and emission spectroscopy. The characterization provides a

---

[*] Excerpts in this chapter are taken from reference 28.

qualitative analysis of the monodispersity in size distribution, average size and emission wavelength for the NPs.

Chemical structure of MPA, M_w = 106.41

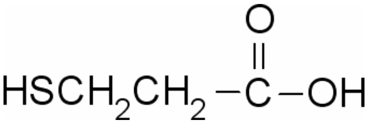

$$HSCH_2CH_2-\overset{\overset{\displaystyle O}{\|}}{C}-OH$$

Chemical structure of CSA, M_w = 113.81

$H_2NCH_2CH_2SH \cdot HCl$

Synthesis procedure:

In 50 ml of deionized water (DI water), under constant stirring and N_2 atmosphere, 1 ml of MPA (density 1.21 gm/cc) is added and allowed to stir for 5 hours. To this solution 40 mg of cadmium perchlorate hydrate ($Cd(ClO_4)_2.6H_2O$) is added and stir for 12 hours. 10 ml of sodium sulfide (Na_2S) solution (6.4 mg of Na_2S in 10 ml of DI water) is added drop wise to it under dark conditions, the solution immediately turns light yellow due to formation of CdS NPs.

For synthesis with CSA an identical procedure is followed. In 50 ml of DI water under N_2 atmosphere, 0.6 gm of CSA is dissolved for 5 hours, to this 20 mg of $Cd(ClO_4)_2.6H_2O$ is added, after stirring overnight 5 ml of Na_2S solution (6.4 mg of Na_2S

in 10 ml of DI water) is added drop wise under dark with constant stirring. Appearance of yellow color signifies the formation of CdS NPs.

The absorbance and photoluminescence characteristics for the anionic NPs (MPA functionalized) are presented below; similar results are obtained for cationic NPs (CSA functionalized), hence are not shown here.

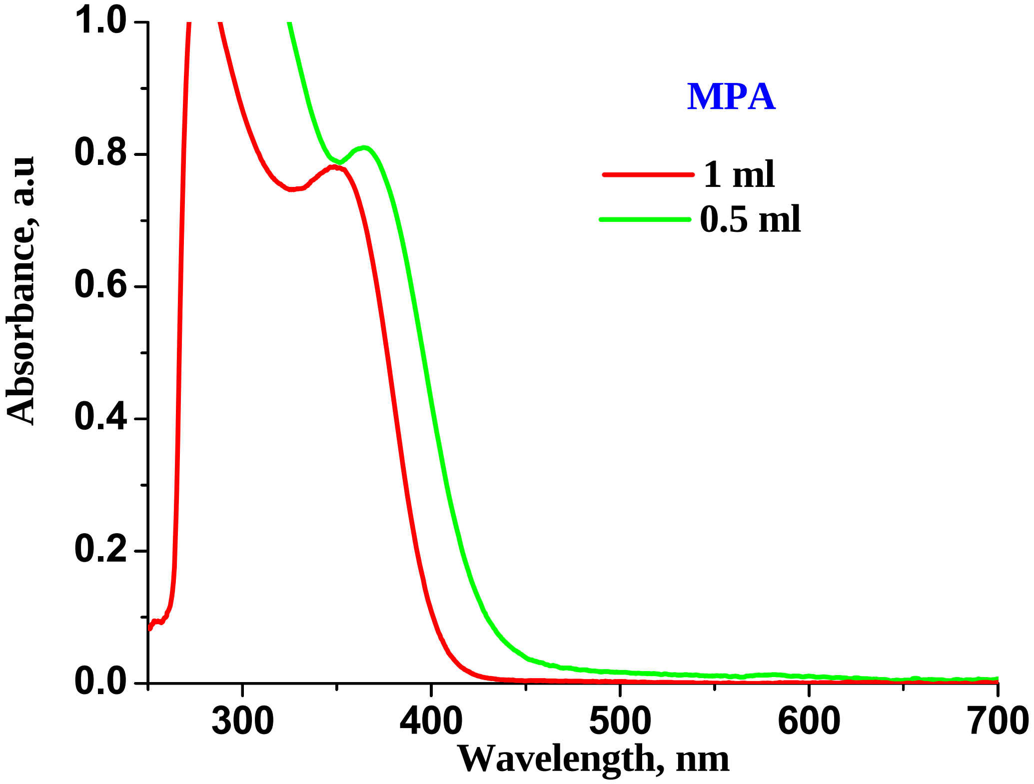

Figure 12. The absorption spectra of MPA-CdS NPs, synthesized with two different MPA concentrations. The edge of absorption corresponds to the bandgap energy E_g. Decreasing the MPA concentration leads to larger size CdS NPs.

The absorption spectrum (as seen in Fig. 12) shows a bandgap E_g of 3.0 eV for synthesis with 1 ml of MPA. The presence of excitonic peak and the sharpness of the spectra indicate narrow size distribution, with a particle size of less than 3 nm. Decreasing the MPA concentration increases the size of NPs, leading to a lower E_g of

2.85 eV. The corresponding size distributions as calculated from the absorption spectra are shown in Fig. 13.[133]

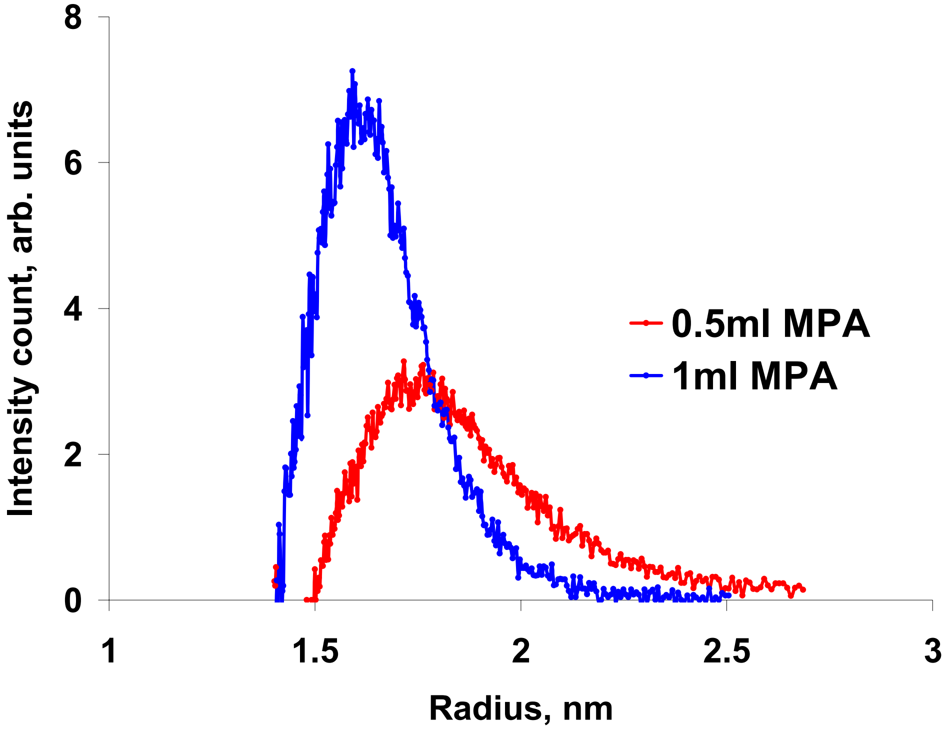

Figure 13. Synthesis with 1 ml MPA yields a particle size of 3.2 nm, and with 0.5 ml the size increases to 3.6 nm (diameter). Narrow size distribution is observed for both conditions.

The photoluminescence spectra of the CdS NPs synthesized with 1 ml of MPA is presented in Fig. 14. The NPs show peak emission at 537 nm with a broad spectrum ranging from 450-620 nm. The red shift and broadness of emission spectrum compared to the absorbance spectra i.e. stokes shift, results from surface trap states governing the emission characteristics. The invariance of emission spectra to excitation wavelength ranging from 380-410 nm indicates the monodispersity in NPs size distribution. Similar trends and results are observed for synthesis with CSA.

From the above analysis of NP synthesis, it can be concluded that:

1. Synthesis of both anionic and cationic CdS NPs with a narrow size distribution has been performed. The monodispersity in size distribution is characterized by the sharpness in the absorbance spectra with the presence of excitonic peak and the invariability of the emission spectra to excitation wavelengths.
2. The NPs have emission in the yellow region of the visible light spectrum with maximum intensity at ~537 nm. Hence this will be the color of emission from the device.
3. The synthesis provides the desired semiconducting NPs as needed for device fabrication.

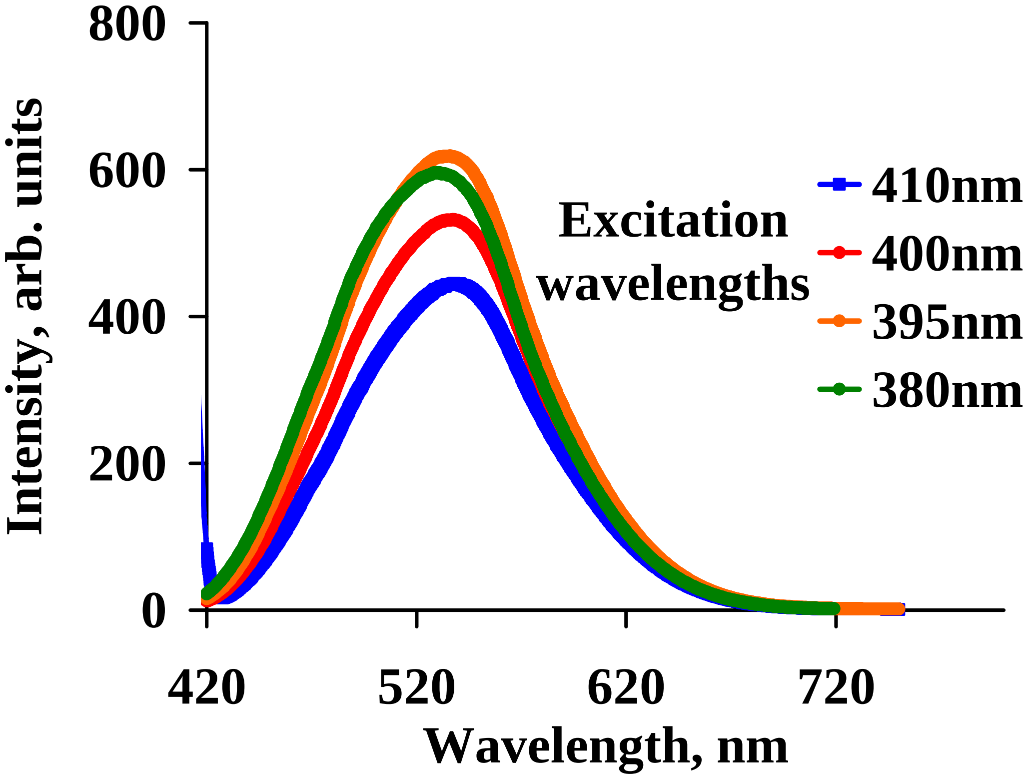

Figure 14. Emission spectra of CdS NPs synthesized with 1 ml MPA. The peak emission is at 537 nm and is invariable to the excitation wavelength. The highest intensity in emission is observed for the excitation wavelength of 395 nm

Gold nanoparticles

Commercially available monodisperse, anionic, 10 nm Au NPs are used as discreet metallic moiety for tunneling of electrons (current) in the device. These are purchased from BBI International and are citrate functionalized.

Polyelectrolyte's for assembly of the device

1. Poly(allylamine hydrochloride) (PAH) of molecular weight 15,000 Daltons is used as the cationic PE.

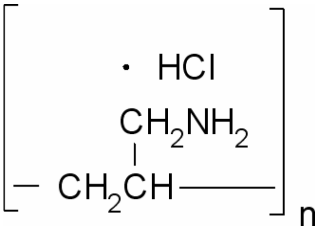

2. Poly(styrene sulfonate) (PSS) of molecular weight 70,000 Daltons is used as the anionic PE.

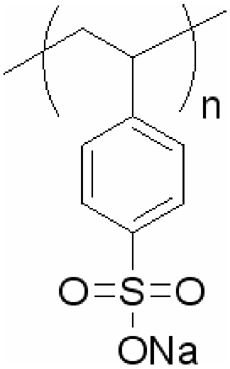

2.2 Device assembly

The device is assembled on 1"x1" glass substrates, coated with a thin transparent conducting layer of indium tin oxide (ITO). The slide is made negatively charged by treatment with piranha solution (30% H_2O_2 and 70% H_2SO_4), after a thorough cleaning with alcohol and sonication. Subsequently the layered architecture is assembled in the following fashion.

1. The piranha solution treated negatively charged substrate is dipped for 30 minutes in the anionic PAH solution followed by a thorough wash with DI water to self-assembly the first monolayer of the dielectric. The PAH solution used is 0.1% (by weight) in DI water.

2. The next monolayer of anionic PE is self-assembled by dipping the substrate in 0.1% (by weight) solution of PSS, with deposition time of 30 minutes. The substrate is again washed thoroughly with DI water after the deposition.

Steps 2 and 3 are repeated to self-assemble the desired number of dielectric (or PE) layers on the substrate.

3. Commercially purchased anionic Au NPs (10 nm) are deposited onto the device with top layer functionality being the cationic PAH. High density discreet deposition of NPs is achieved in 18 hours.

4. CdS NPs synthesized with either MPA or CSA are used to deposit the active electroluminescent layer onto the oppositely charged device layer, PAH for MPA and PSS for CSA. High density of deposition is observed in 2 hours.

Each deposition step is performed at room temperature and is followed by a thorough wash with DI water.

The devices are fabricated by assembling 3-5 alternating bi-layers of PAH-PSS, these together constitute the dielectric layer (DE); this is followed by deposition of a layer of Au NPs. A layer of dielectric is again deposited on top of Au NP layer. Following this a layer of CdS nanoparticles is deposited. The sequence is repeated to assemble the final device structure DE-Au-DE-CdS-DE-Au-DE-CdS-DE-Au-DE. The first NP layer to be deposited is Au followed by CdS, both anionic and cationic CdS have been used for fabrication of devices with qualitatively the same results. The final device has 3 layers of Au NP, interlaid by 2 layers of CdS NPs.

2.3 Device structure analysis

The discreetness and density of deposition for the NPs is characterized by performing atomic force microscopy (AFM) and X-ray photoelectron spectroscopy (XPS) on the samples. Fig. 15 presents the AFM phase images for the layers of NPs deposited in device fabrication. Discreetness of structure is observed in each layer with high density of NP deposition. The thickness of a single bi-layer of DE (PAH-PSS) is ~2-2.5 nm from AFM analysis. Hence a separation of ~8-10 nm is obtained between the Au and CdS NP layers for a four bi-layer DE deposition between the nanoparticle layers.

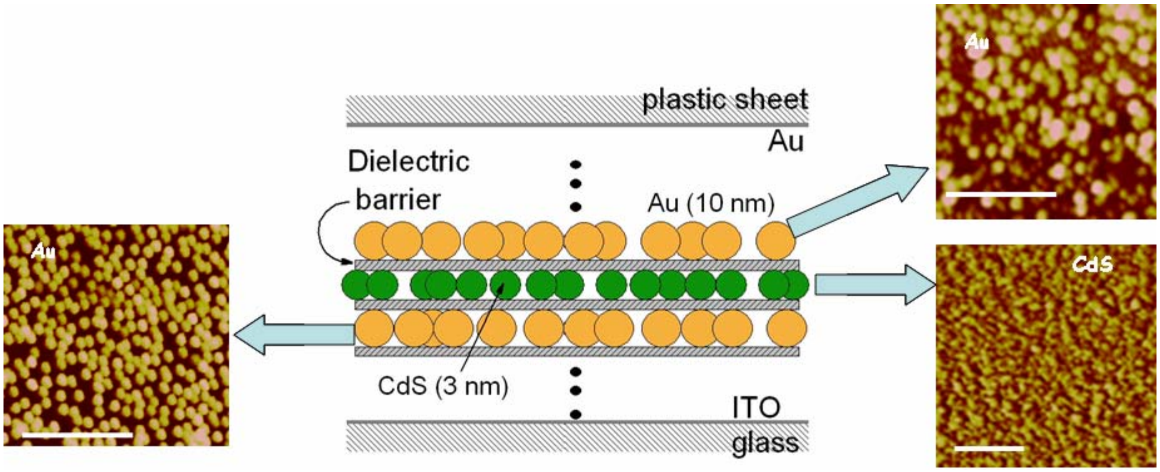

Figure 15. AFM characterization of the deposited NP layers for device fabrication. Phase images are shown for the 1st, 2nd and the 3rd layer of NPs deposited. The scale bar in each image is 50 nm.

To confirm the deposition, XPS analysis is performed on the device subsequent to deposition of the NP layers. The XPS spectrum of Fig. 16 confirms the deposition of Au and CdS in the first and second layer of NPs respectively (the intermediate dielectric layer is a single PAH-PSS layer). The penetration of the X-ray beam being ~6-8 nm allows the observance of Au NP layer even after the deposition of CdS layer (3 nm) and the intermediate dielectric ~2-2.5 nm. Experiments with larger DE thickness subdue the signal from underlying NP layers. Further a complete device with 4 bi-layers (PAH-PSS) of DE between each NP layers has a thickness of ~100-120 nm as confirmed by topography scans obtained using a profile-meter.

Following the analysis, the fabrication of devices with the desired layered architecture is confirmed. The response from the device will be critically determined by the density in NP deposition and the spacing between NP layers due to the inter-laying DE. The spacing between the NP layers can be controlled with nanometer scale precision by modulating the number of inter-laying dielectric (PE) layers. The ability to control the thickness of DE gives us the means of controlling device response by tailoring the separation between NP layers.

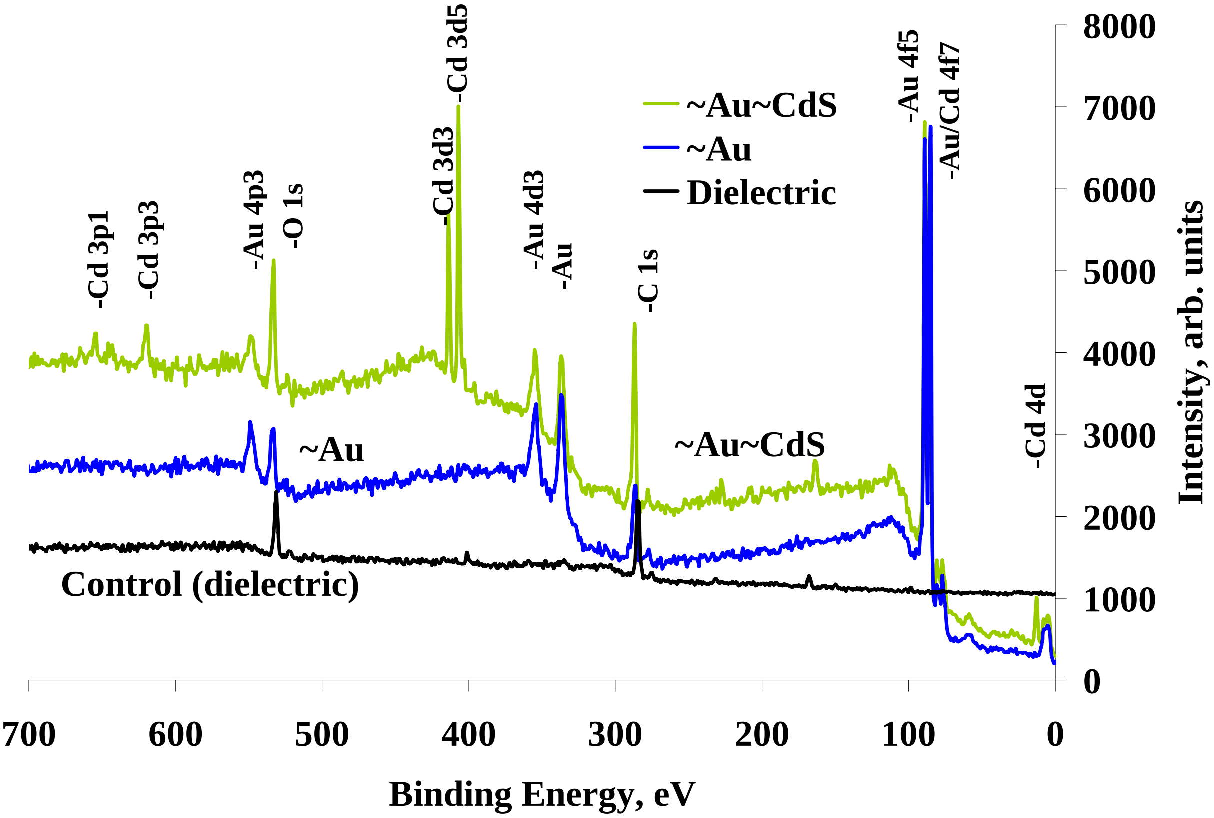

Figure 16. XPS characterization of the NP layers in the device. The presence of Au and CdS is confirmed by the elemental peaks. The control dielectric shows no trace of either.

2.4 Device testing and analysis

Following the successful assembly of the device its performance is measured to quantify the response and more importantly to ascertain the principle governing its response.[28]

2.4.1 Setup

The device response is measured using a set-up presented in Fig. 17. With applied bias and stress loading the performance of the device is characterized by measuring the current and electroluminescence response. A gold electrode (optically flat disc of Au) placed on the device functions as the top electrode and the bottom ITO layer is the other electrode. A load cell connected to a stepper motor is used to apply pressure to the device by pressing against the Au electrode. The electroluminescence output is measured by placing a photomultiplier tube (PMT) directly below the device (Fig. 17).

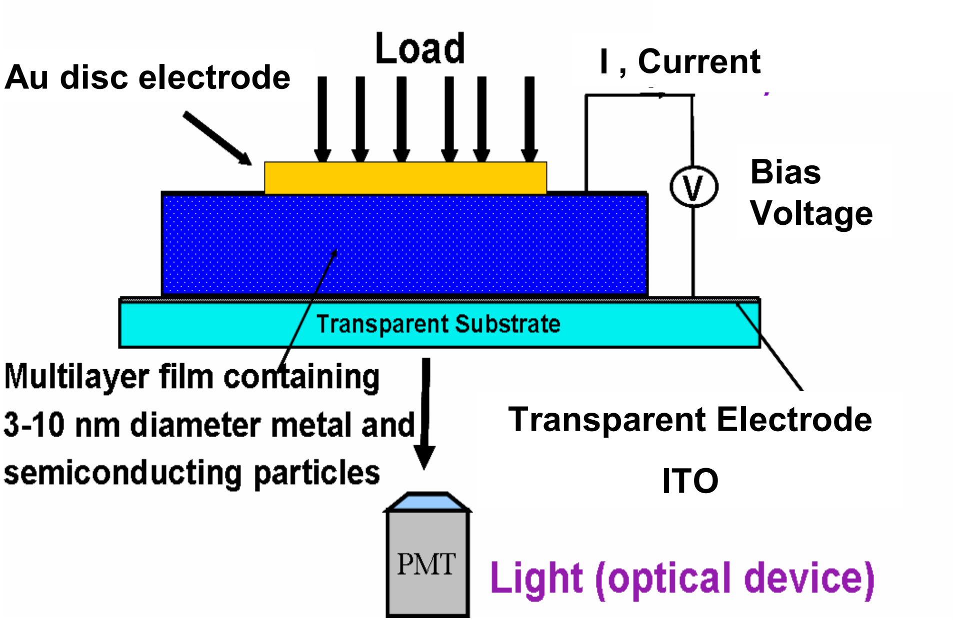

Figure 17. Schematic of set-up to measure the electrical (current) and optical (light) response from the device under bias, to applied stress.

2.4.2 Device response: voltage and loading effects

Following the assembly, the device response is measured by the current (the current density J, in milli-Amphere/cm^2, mA/cm^2, is plotted) and EL intensity (I_{EL}) response to varying bias under constant loading, and to varying loads under constant bias. I_{EL} results reported in this section (2.4) are normalized to intensity (in arb. units) per pixel of the CCD camera used for stress imaging (section 2.4.4). Results from devices with varying DE layer thickness lead to the conclusion that 8-layer device have the closest measurable response to human skin as a tactile sensor. The analysis of effect of DE thickness on device response is presented in the next section.

In this section presented is the analysis of the results for 8-layer device, i.e. the inter-laying DE between the NP layers is composed of 4 layers of PSS and 4 of PAH (4 bi-layers). The results are presented in Fig. 18 a,b,c&d.

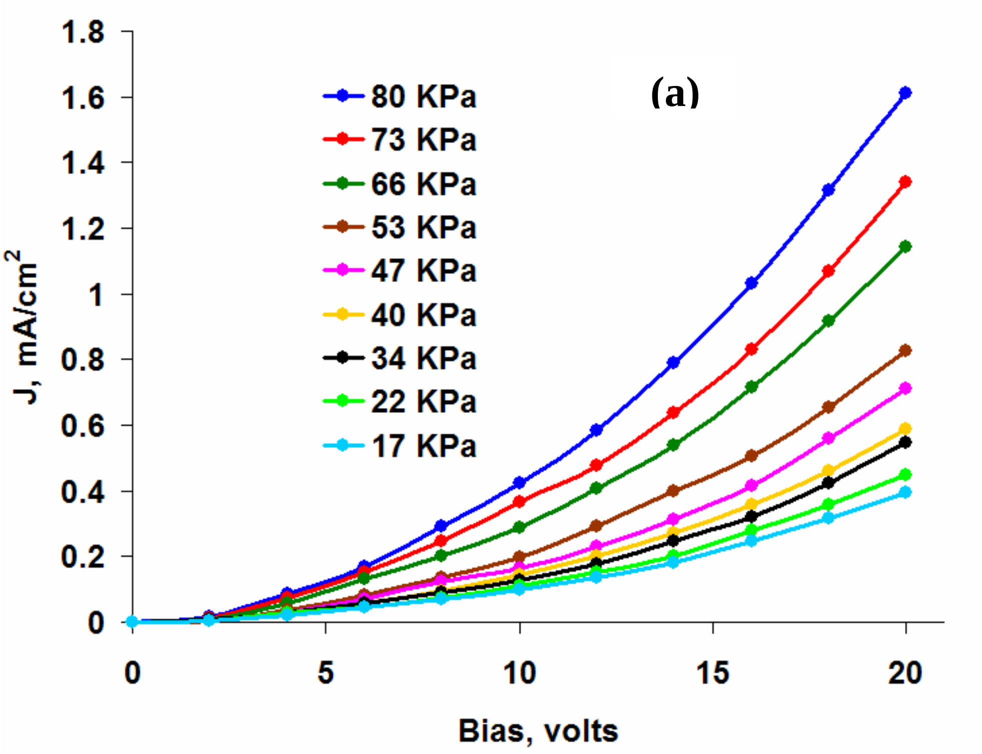

Figure 18a. Current density (J, mA/cm^2) response of the device to bias (V); J vs V with increasing loads.

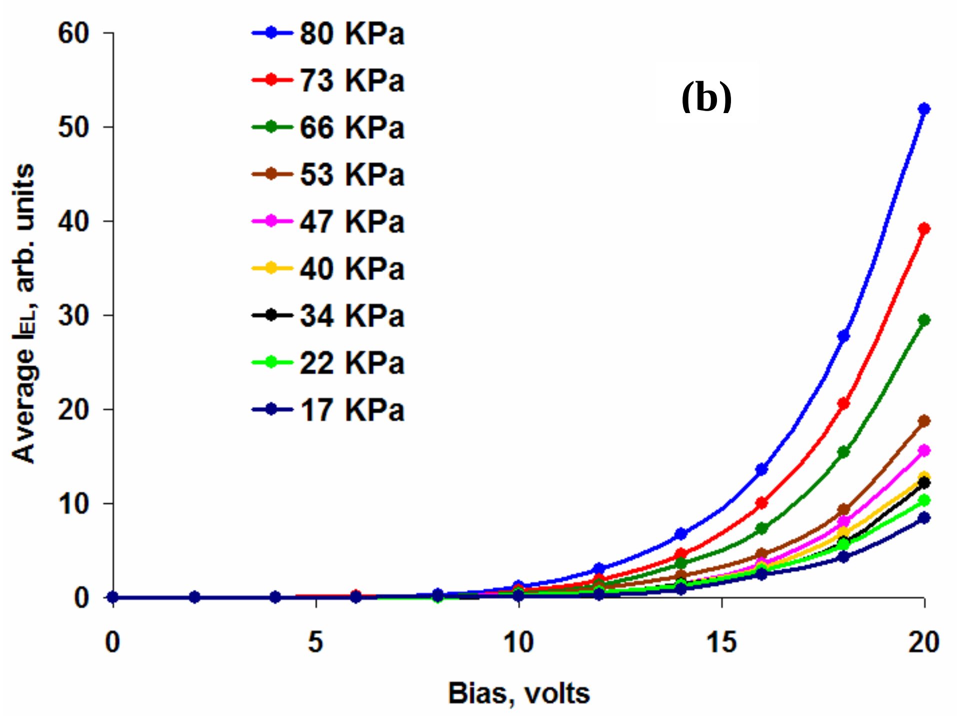

Figure 18b. EL (I_{EL}, arb. units) response of the device to bias (V); J vs V with increasing loads.

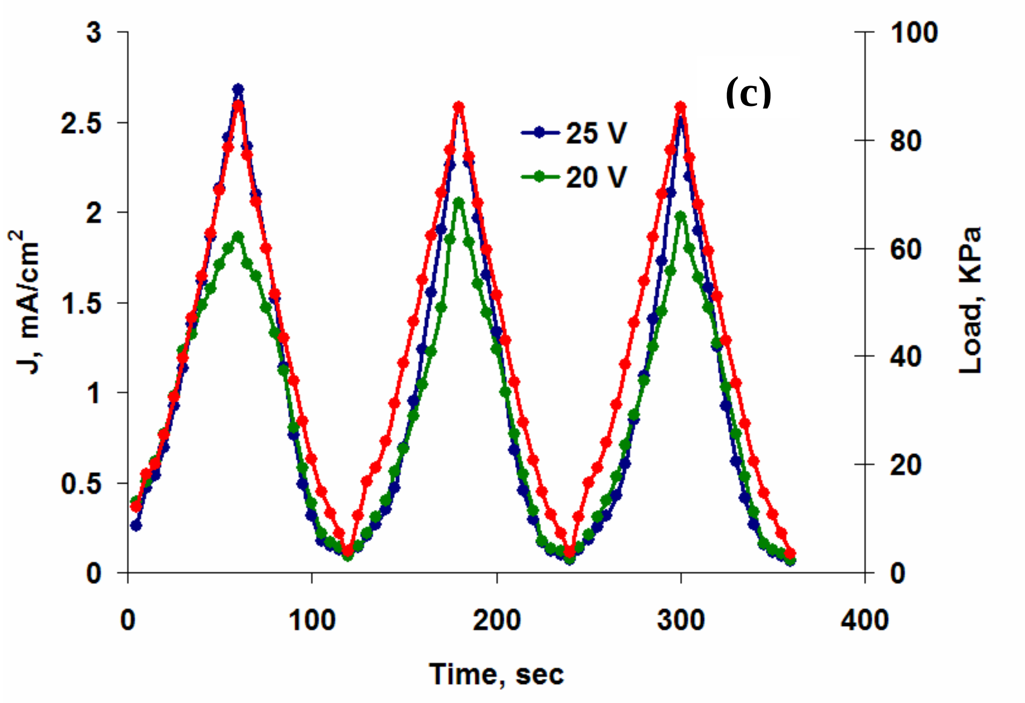

Figure 18c. Current density (J, mA/cm^2) response of the device to cycling loading at constant bias; J vs Load.

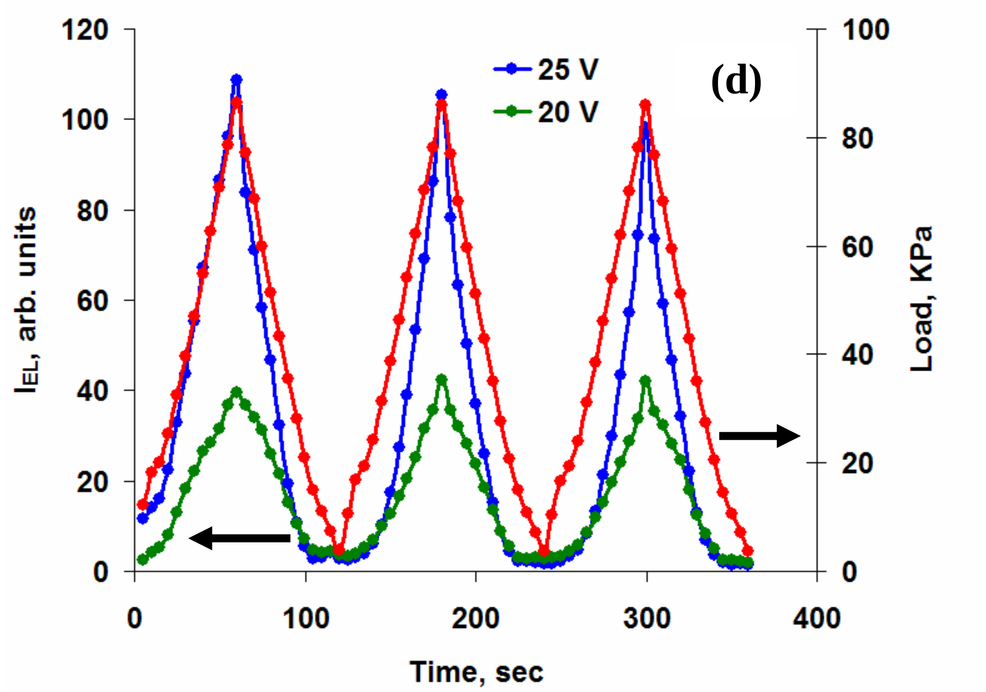

Figure 18d. EL (I_{EL}, arb. units) response of the device to cycling loading at constant bias; J vs Load.

Figure 18. Current density (J, mA/cm^2) and EL (I_{EL}, arb. units) response of the device to applied load (KPa) and bias (V); (a) J vs V with increasing loads. (b) I_{EL} vs V with increasing loads (C) J vs Load, with cycling loading at constant bias (d) I_{EL} vs Load, with cycling loading at constant bias.

Figs. 18 a&b show the nonlinear dependence of J and I_{EL} to applied bias, a threshold of ~8 V is observed in I_{EL}. The increase in J and I_{EL} with load suggests the modulation of DE thickness (i.e. tunneling barrier) with stress, resulting in increased current (J) and electroluminescence (I_{EL}) at higher stresses (load).

For cyclic loading of the device at constant bias we observe that both J and I_{EL} response follow the loading cycle, Figs. 18 c&d. At low bias a non-linear increase in J and I_{EL} is observed, where as they increase linearly at high bias and loads. The device is robust under cyclic loading, with same quantitative response in each cycle.

From these results it can be concluded that:

1. The device is indeed sensitive to both applied stress (load) and bias with a non-linear response in J and I_{EL}. The results are in agreement with the tunneling mechanism proposed for working of the device.
2. The robustness of the device in structure is inferred from its consistent response under cyclic loading.
3. The current and EL response are sufficiently high enough to be measured with a current meter and PMT.

2.4.3 Theoretical model for device response

The current, J and electroluminescence, I_{EL} are the two output parameters that are characterized in response to external stimuli of bias (Voltage, V) and stress (σ, Kilopascals, KPa). Both J and I_{EL} result from the flow of electrons across the device cross-section, i.e. through the layers in the device. Current is directly the sum of total electrons flowing in response to applied stimuli across the device. The electroluminescence however is specifically due to the tunneling of electrons through the NP layers (the EL active semiconducting layer), a fraction of these tunneling electrons result in EL through recombination with holes. The recombination factor is governed by the ratio of electron and hole current through the semi-conducting NPs and is a material property, hence the tunneling current and EL should be linearly proportional given a constant bias. Higher bias leads to increase in both electron and hole current, therefore increasing the efficiency of recombination or EL. The emission characteristics of the EL light will be governed by the nature of the CdS layer, i.e. wavelength of emission, activation voltage and efficiency. The EL phenomenon is similar to photoluminescence except that the activation in EL is provided by applied bias rather than illuminating photons as in PL. Since J will be sum total of all electrons flowing across the device, including tunneling electrons through CdS layer, it will also govern the behavior of EL.

Focusing on contribution to J, consider the pathways for flow of electrons in the device. As discussed, tunneling of electrons through the NP layers is proposed to be the central mechanism governing the response of device as a tactile sensor. The tunneling current $J_{tunnleing}$, a result of field assisted electron tunneling (i.e., Fowler-Noedheim tunneling) will depend exponentially on the separation between the NP layers and the applied bias.

$$J_{tunneling} = P\exp(-aK/V) \qquad (24)$$

Here, ‘a’ is the (vertical) inter-particle distance, ‘K’ is a critical field for activated tunneling that depends on the work functions of the particles, and ‘P’ at constant temperature is proportional to V^2 and the number density of carriers for conduction.

The device is composed of polyelectrolyte layers functioning as dielectric, since these are hydroscopic materials absorbed water will be present, resulting in mobility for the ions in the PE layers (H^+, OH^-, Na^+, Cl^-). Application of bias will lead to ionic currents due to mobility of these ions. The ionic current is termed as ionic leakage-current, $J_{leakage.}$

$$J_{leakage} = V/R, \qquad (25)$$

Here, ‘R’, the ohmic resistance, is proportional to the distance between the electrodes. A three parameter (i.e., R, aK, and P) fit for the current (J) vs bias (V) set of data, with a corresponding straight line due to leakage I-V, is an excellent match to experiment for the whole range of V and σ studied (Fig. 19). The three fitting parameters are self-consistent as applied stress increases (Fig. 20); R from the fit linearly decreases with σ implying the film deforms linearly. The estimated resistivity of ~ 1.6×10^8 Ω-m is reasonable for ion conductivity in PSS and PAH under ambient humidity.[33] The linear decrease in aK with σ indicates that the interparticle spacing (i.e., a) also decreases linearly with σ which is consistent with linear deformation of overall thickness. Assuming a (at $\sigma = 0$) ~ 5 nm, the critical field K of ~ 10^9 V/m is reasonable.[24,25] As P depends on the carrier density, at fixed V, the linear increase in P may be attributed to a linear increase in the number of percolating channels between the electrodes as the film is deformed. Consistent with the Fowler-Noedheim eq., $P \sim V^2$ (at constant load) for the complete range of operating conditions at bias greater than 8 V (Fig. 21a). Curve-fit in Fig. 19 indicates that the tunneling process becomes important beyond ~8V (indicated as a box). Electroluminescence will occur only when tunneling through CdS occurs. Hence the electroluminescence intensity, I_{EL}, should be measurable above the bias of ~8±1V; this is consistent with the I_{EL} measurements (Fig. 18b). At high bias the linear dependence between J and I_{EL} (Fig. 21b) is consistent with the proposed mechanism, i.e. EL is directly proportional to the tunneling current. Higher bias leads to a greater efficiency for EL from tunneling current.

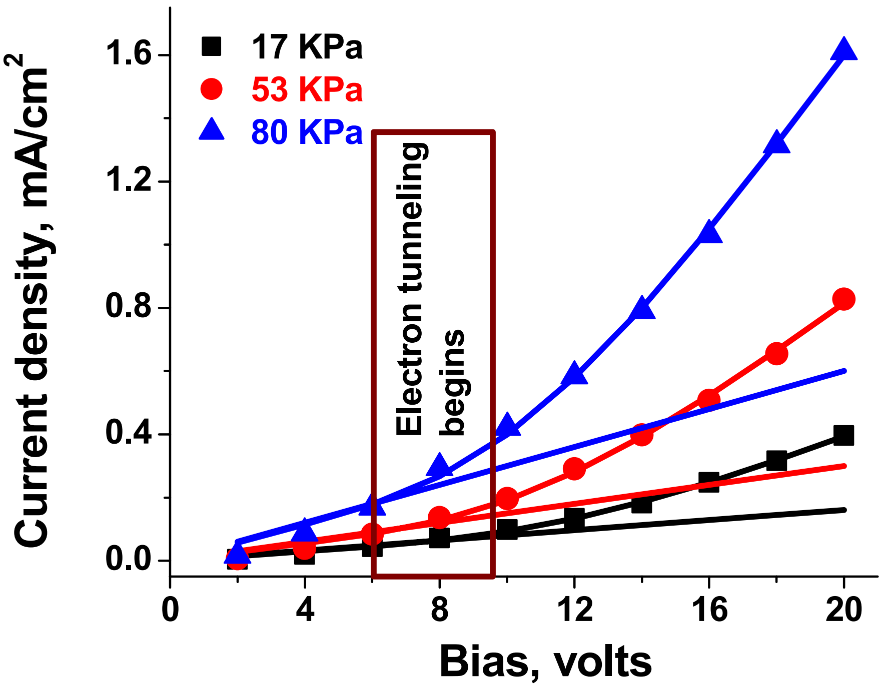

Figure 19. J-V data points for three σ. The fitted line is based on the model, combining charge transport by electron tunneling and ions. The straight lines correspond to $J_{leakage}$. The box indicates the expected onset of electroluminescence.

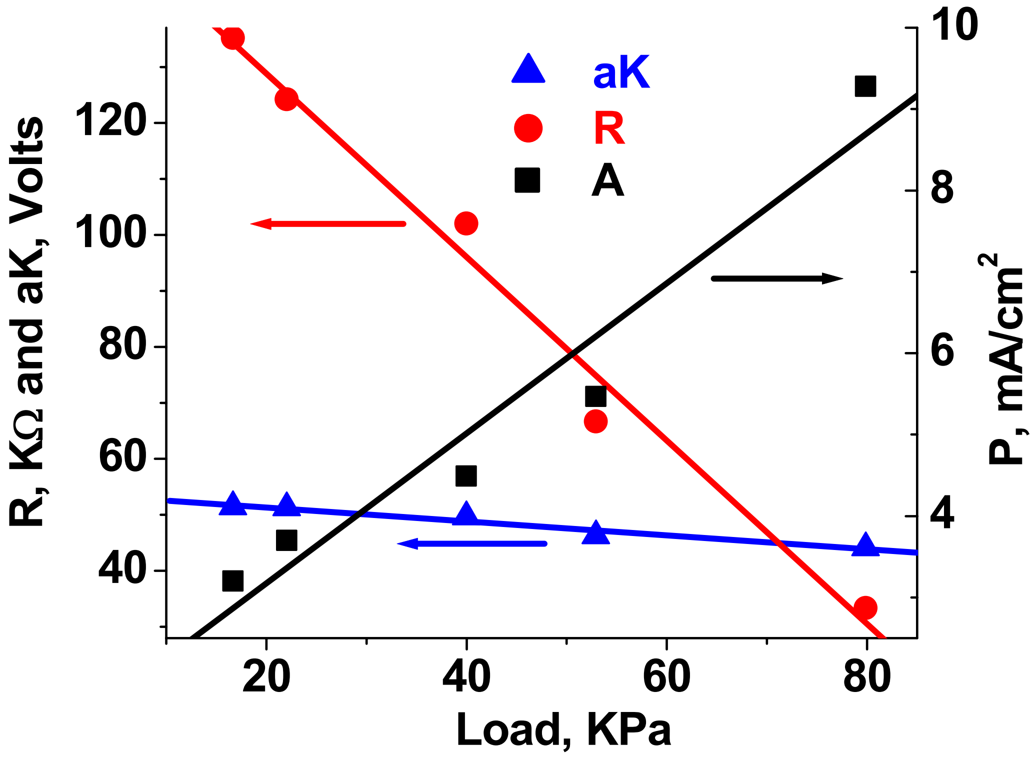

Figure 20. The three fitting parameters estimated from fitting the J-V curve show linear dependence indicating the deformation is linear with respect to load.

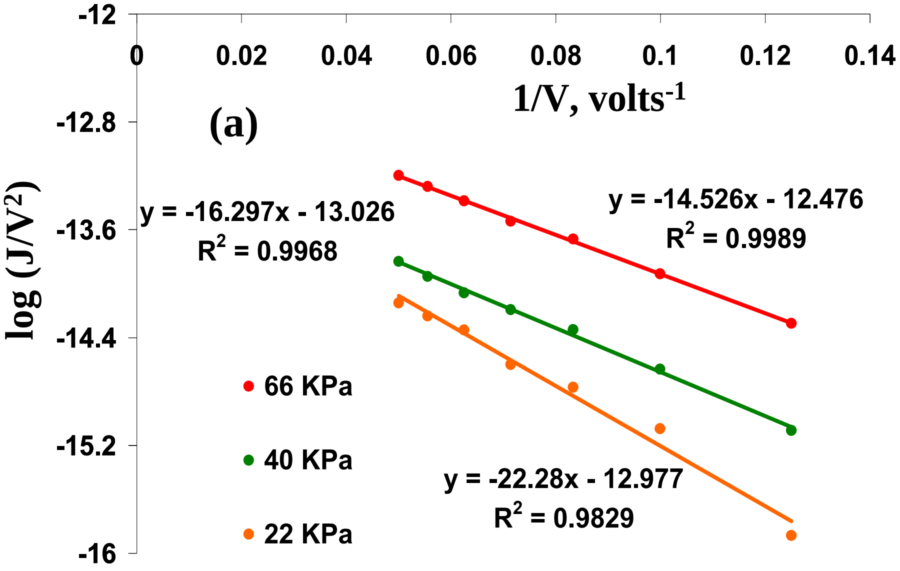

Figure 21a. For bias of greater than 8 V, P varies as V^2 at constant load, consistent with the Fowler-Noedheim tunneling equation.

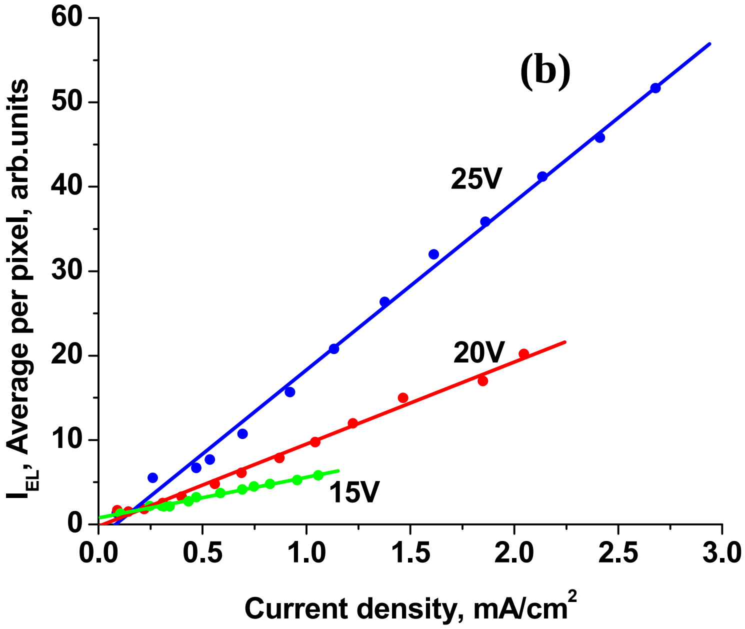

Figure 21b. Comparison of electronic (i.e., current) and optical (i.e., electroluminescence) signals: I_{EL} is linearly proportional to J.

Figure 21. (a) For bias of greater than 8 V, P varies as V^2 at constant load, consistent with the Fowler-Noedheim tunneling equation. (b) Comparison of electronic (i.e., current) and optical (i.e., electroluminescence) signals: I_{EL} is linearly proportional to J. Each data point is at fixed bias with varying σ. The slope at the three bias are, 6.0, 10.5, 19.0 (arb.units) cm^2/mA. The efficiency of the device to convert current to electroluminescence increases with bias as indicated by the slope.

2.4.4 Tactile sensing

The tactile sensing capabilities of the device are measured with the setup shown in Fig. 22, the EL output from the device is directly focused on a CCD to capture the stress image resulting from pressing of the object used in tactile sensing.

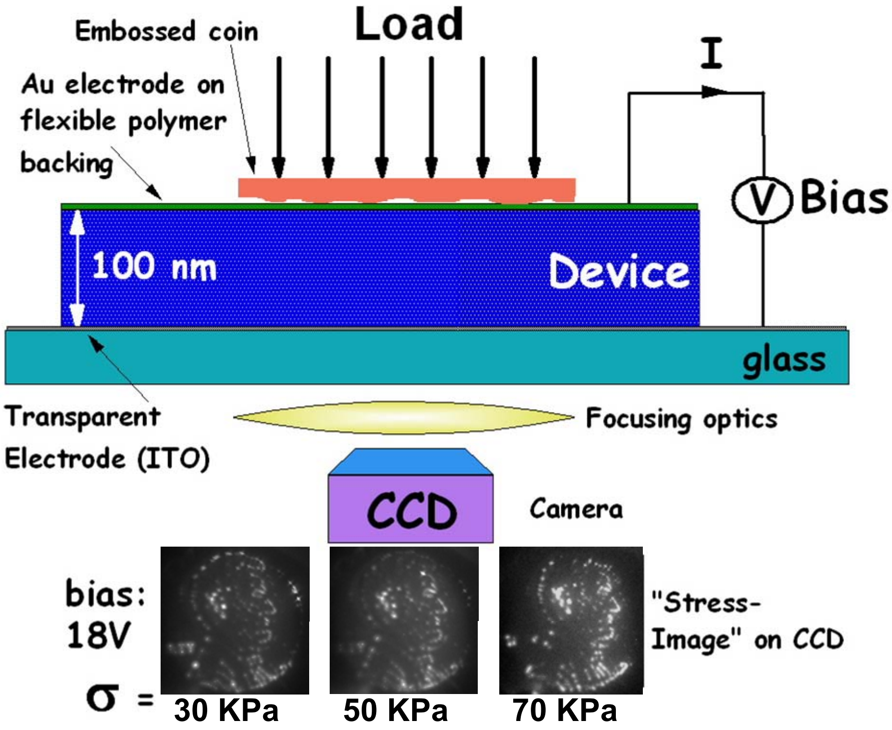

Figure 22. Schematic of the set-up to image texture of a metal coin, also shown are the pressure images taken with a CCD camera at three different compressive stresses. The diameter of the coin is ~2 cm and the device is a 2.5 cm square. The bias between the flexible Au electrode and the ITO electrode is fixed at 18V.

Figure 23. The electroluminescence image on the CCD camera corresponding to a 1.12 cm diameter quartz disk pressing the top electrode. (a) At $\sigma = 40$ KPa. (b) At $\sigma = 100$ KPa, the image appears defocused due to a tilt in the camera.

The EL profile of an optically flat, 1.12 cm diameter quartz disk is imaged by pressing on the top electrode (Fig. 23). Uniform light illumination across the disc indicates continuous load distribution and continuity in device structure. The average I_{EL} per pixel is limited to application of loads of 80 KPa for uniform electroluminescence from the tactile object as at higher loads the edges are enhanced due to "square-edge-punch" stress concentration.[126] The stress concentration is seen on imaging the optically flat quartz disc where at higher loads (σ) the edges become prominent, Fig. 23 b.

The electroluminescence intensity, I_{EL}, should be measurable above the bias of ~8±1 V. I_{EL} reported is intensity (in arb. units) per 16x16 μm pixel of the CCD camera. The noise level based on imaging a blank sample (i.e., dark current) is 1 arb. unit.

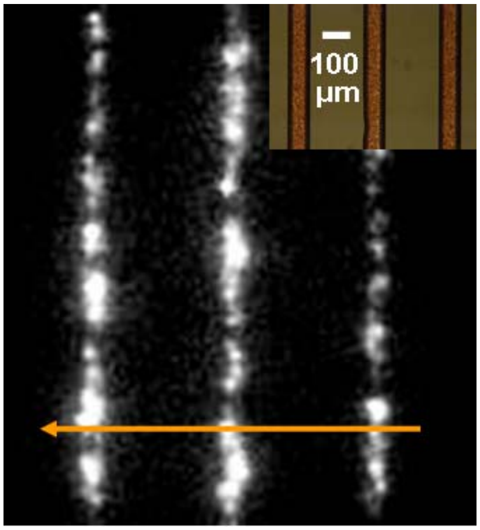

Figure 24. Comparison between optical microscope (inset) and pressure image (at V = 18 V and σ = 40 KPa) of a TEM Cu grid, the horizontal line in pressure image is the I_{EL} scan shown in Fig. 25.

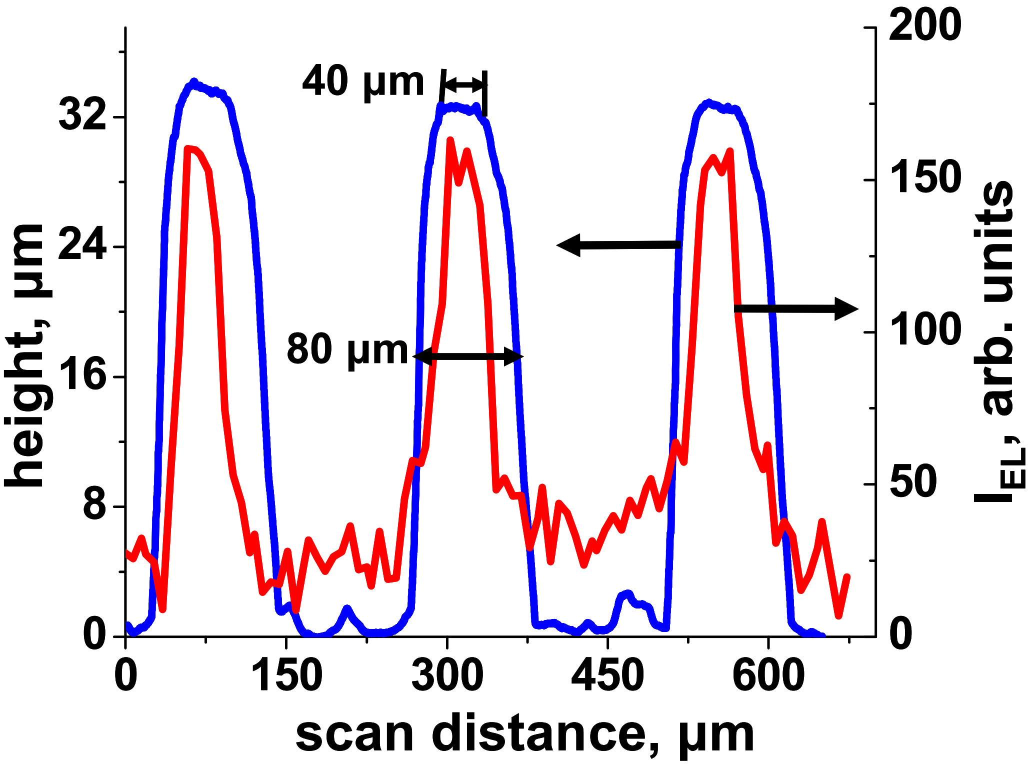

Figure 25. Comparison between the topographic and I_{EL} scan across the TEM Cu grid shown in Fig. 24. The flat top of 40 µm of the Cu lines on the grid is clearly visible in the I_{EL} scans.

To assess the capabilities of the device for measuring surface topography/texture a TEM specimen holder (i.e., a Cu grid, from Electron Microscopy Sciences) and a US one cent coin was pressed against the flexible Au electrode of the device, and the electroluminescent light from the device focused on the CCD camera below the ITO/glass substrate (Fig. 22). The embossing of President Lincoln’s head on the coin is apparent in the stress image obtained on the CCD. The overall intensity of the “stress-image” increases with average stress, σ, (Fig. 22). The TEM grid lines have a trapezoidal cross-section with a top base of 40 µm that is in contact with the device, a width of 80 µm at half height, and inter-line spacing of 230 µm (Fig. 24 inset & Fig. 25). Lines of the Cu grid (seen in the optical microscope image) are clearly resolved in the stress-image (Fig. 24). Comparison between the topography and I_{EL} scan of the TEM Cu grid (Fig. 25) shows that the flat surface of 40 μm line width in contact with the device is well resolved leading to a lateral spatial resolution of at least 20 μm.

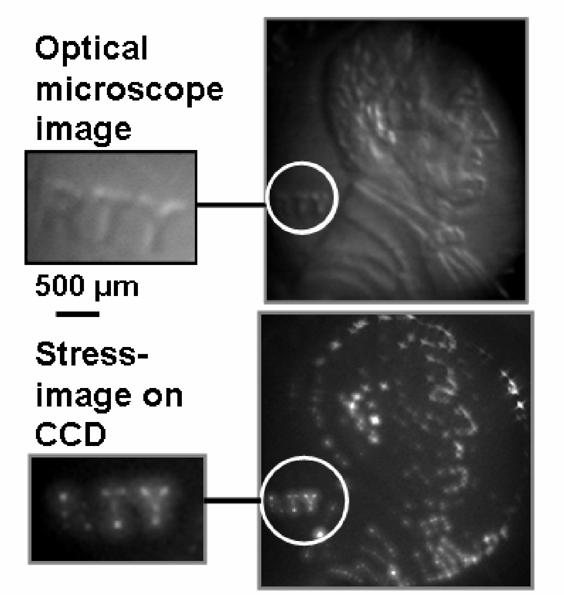

Figure 26. A comparison between optical microscope and pressure image (at V = 18 V and σ = 30 KPa) of the coin showing the finer structure. The magnified image shows the letters 'RTY' of the word 'LIBERTY' on the coin.

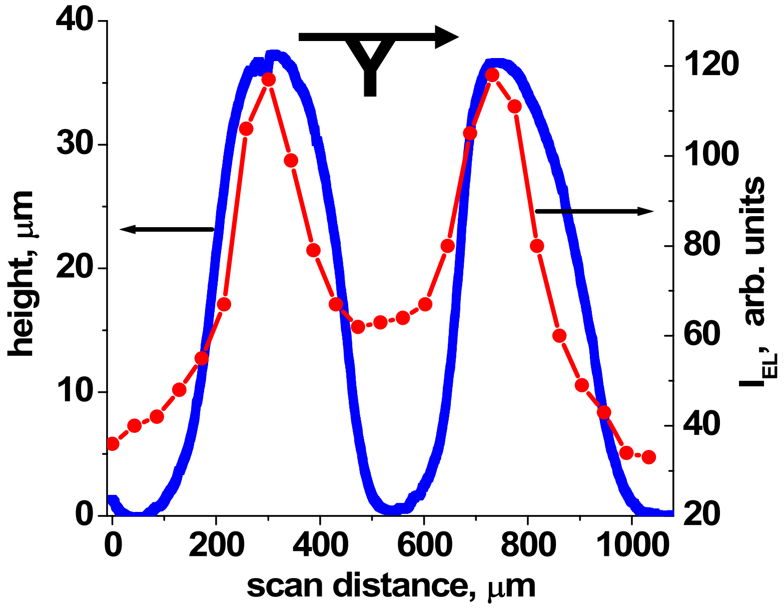

Figure 27. A comparison between topographic scan and I_{EL} scan across the letter 'Y' of LIBERTY. The scan is along the upper edge of the 'V' in the letter.

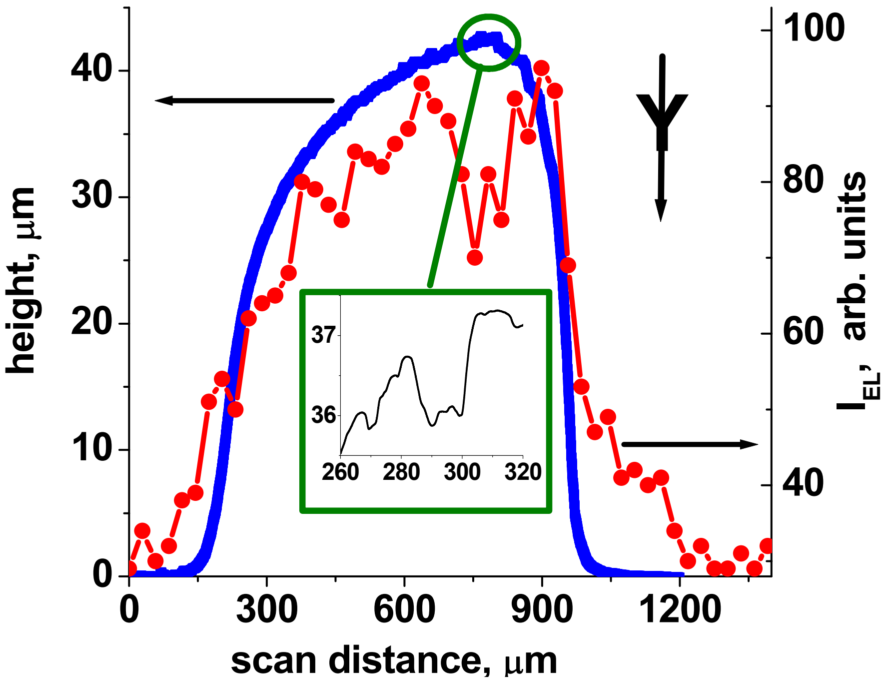

Figure 28. A comparison between topographic scan and I_{EL} scan down across the letter 'Y' of LIBERTY. The scan is along the vertical line in the letter 'Y'. The inset shows the local roughness of the coin.

The remarkable correspondence between the optical microscope image and the "stress image" seen in Fig. 22, 26, 27 & 28 indicates that the variation in stress distribution caused by embossing on the US one cent coin leads to significant change in local current density, which in turn is manifested as modulation in I_{EL}. The device can decipher fine features, such as wrinkles of the clothing of President Lincoln and the letters 'TY' in 'LIBERTY' observed in the optical microscope and stress-image (Fig. 26). As the electroluminescence intensity from the device is virtually continuous, the resolution of the stress image is determined by the optics and the CCD camera. For the CCD with a 512x512 array of ~16 μm pixels, the I_{EL} is well over noise level (Figs. 25, 27 & 28) indicating that the electroluminescence is enough to achieve lateral spatial resolution of at least ~20 μm (as the area of chip and disk are comparable). However, stress will be "smeared" due to thickness of the flexible Au electrode, leading to larger resolution. Furthermore, from Fig. 27 & 28, height modulation of ~10 μm is measurable, indicating the device is fairly deformable. The high compliance is perhaps due to some interpenetration among the nanoparticle layers. The inset in Fig. 28 shows that the embossing is rough at the micron scale. The local roughness will cause non-uniformity in the surface charge distribution leading to "hot-spots" of high electric field strength. The "pointillist" pressure-images are attributed to these hot spots.

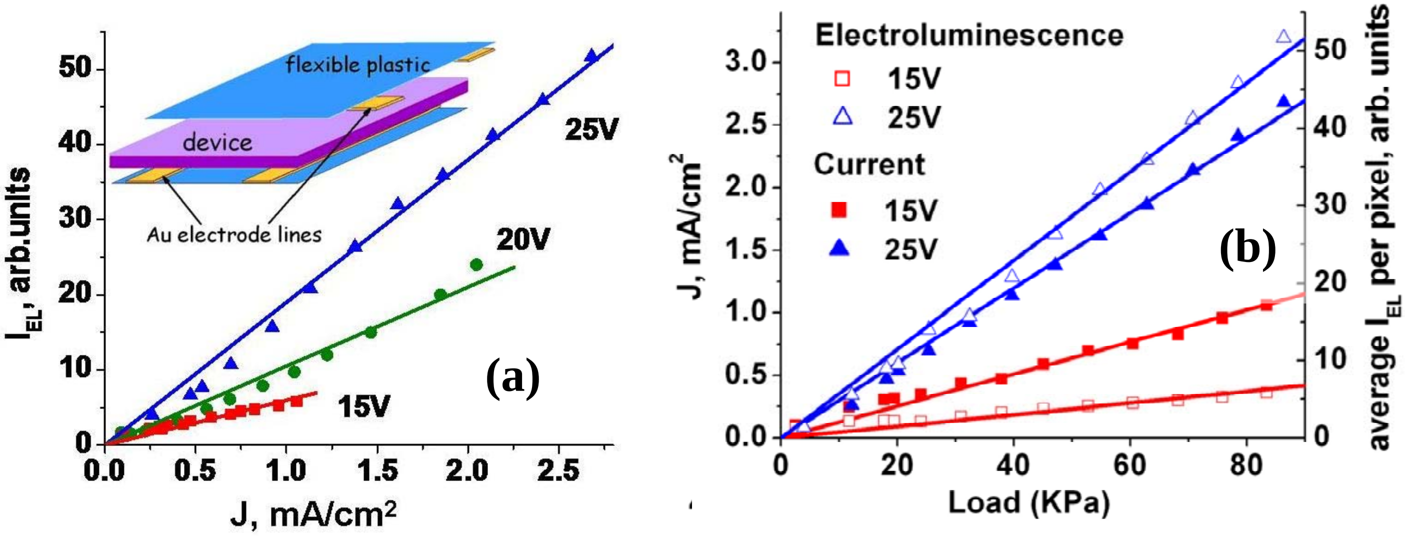

Figure 29: Comparison of electronic (i.e, current) and optical (i.e. electroluminescence) signals: (a) I_{EL} is linearly proportional to J. Each data point is at fixed bias with varying σ. The slope at the three bias are, 6.0, 10.5, 19.0 (arb.units) cm^2/mA. The efficiency of the device to convert current to electroluminescence increases with bias as indicated by the slope. (b) Both J and I_{EL} increase linearly with load for the entire range studied. The change in slope as bias increases from 15 to 25V for J and I_{EL} is 2.34 and 7.63, respectively.

Relationship between the optical (i.e., I_{EL}) and electronic (i.e., J) signal from the device pressed by the quartz disk is linear (Fig. 29a), implying that the stress image from either signal would be similar. Above, we have demonstrated the tactile sensor principle by measuring I_{EL}. Extension to a fully electronic device by measuring I, required for certain applications (such as surgery), is possible using standard microelectronic circuitry. For example, an electronic device could be made by self-assembling the multilayer thin-film between mutually perpendicular parallel lines of Au (electrodes) on flexible plastic backing (i.e., flex-circuit). The stress distribution would be imaged by mapping J at the "intersection points" of the top and bottom electrode lines (similar to a display device). Both I_{EL} and J increase linearly with σ, however the sensitivity to bias for the optical device is larger (~3-fold) implying the latter has a larger dynamic range (Fig. 29b). For I_{EL}~ 5 (corresponding to signal-to-noise of 5) the sensitivity of the optical device is ~9 KPa at a bias of 25V. Assuming a minimum measurable current signal of 1 nA for the electronic device proposed in the inset of Fig. 29(a), for the intersection point of ~20 sq. μm[127] a sensitivity of ~10 KPa would be possible. As the resolution of 20 μm is comparable to the CCD pixel size used in the optical device, a spatial resolution of ~50 μm at a sensitivity of 10 KPa should be possible for the electronic device.

There are two practical advantages of the described tunneling-based device compared to the reported tactile imaging devices based on deformable membranes or stress sensitive materials. First, we achieve high sensitivity because tunneling depends exponentially on displacement (i.e., strain). Second, the self-assembly process involves no complex lithography making it easier to build the device directly on surfaces of large area and complex shapes.

2.4.5 Conclusion

The successful assembly of a tactile device with resolution and sensitivity comparable to human skin has been presented. The device architecture of layered assembly consisting of metallic and semiconducting NPs with spacing dielectric layers has been successfully fabricated using the l-b-l approach. The method allows easy fabrication of the device on large area substrates and complex shapes (no physical limit is placed on the size of the substrate). The structure and uniformity of device layers is confirmed by AFM and XPS. The deposition is uniform with high density and discreetness of NPs in the deposited layers. Nanometer scale spacing between the tunneling layers of NPs has been achieved in a simple fashion, and further it can be controlled with nanometer scale precision by varying the number of PE layers deposited as the dielectric barrier, since each PE bi-layer is ~2-2.5 nm thick.

Anionic and cationic CdS NPs with uniform size distribution required for intense EL response from the device have been synthesized. Their characterization from absorbance and emission spectroscopy shows a narrow size distribution with the excitonic peak signifying their uniform crystalline structure. Further successfully control of their size by varying the ratio of thiol (capping agent) to Cd has been achieved.

The current and EL response from the device to applied load and bias clearly show it has a sensitivity and resolution comparable to that of human skin. The device is robust under cyclic loading with stable response. The device response is a perfect fit to a three parameter model based on tunneling and ionic currents. The response and model are in agreement with the proposed modulation of the dielectric layer with stress loading, resulting in the current and EL response based on the local stress profiles. An electronic read-out for the device will have a similar response as measured by EL imaging due to the linear dependence between current and EL intensity.

2.5 Effect of dielectric barrier thickness

The polyelectrolyte layers function as dielectric barriers for tunneling of electrons between the nanoparticle layers in the device. The three parameter model suggests an exponential dependence of tunneling current, $J_{tunneling}$ on DE thickness and an ohmic dependence to ionic leakage currents, $J_{leakage}$. The effect of DE thickness on device response is characterized by varying the number of DE layers inter-laying the NP layers.

2.5.1 Results and discussion

The numbers of interlaying dielectric monolayers are varied from 6, 8 to 10 (a 6 layer DE is 3 each of PSS and PAH, between each NP layers) and the response of the device is characterized in terms of current and electroluminescence. All devices consist of 3 layers of Au and 2 layers of CdS nanoparticles. The device response current density (J, milli amp/cm^2) and electroluminescence intensity (I_{EL}, arb. units) are measured as a function of bias V between the bottom ITO and top Au electrode, under a uniform compressive stress σ. I_{EL} is reported as the average over the whole CCD area compared to per pixel as reported in section 2.4. The stress is applied by pressing an optically flat quartz disc on the flexible Au electrode (setup shown in Fig. 17).

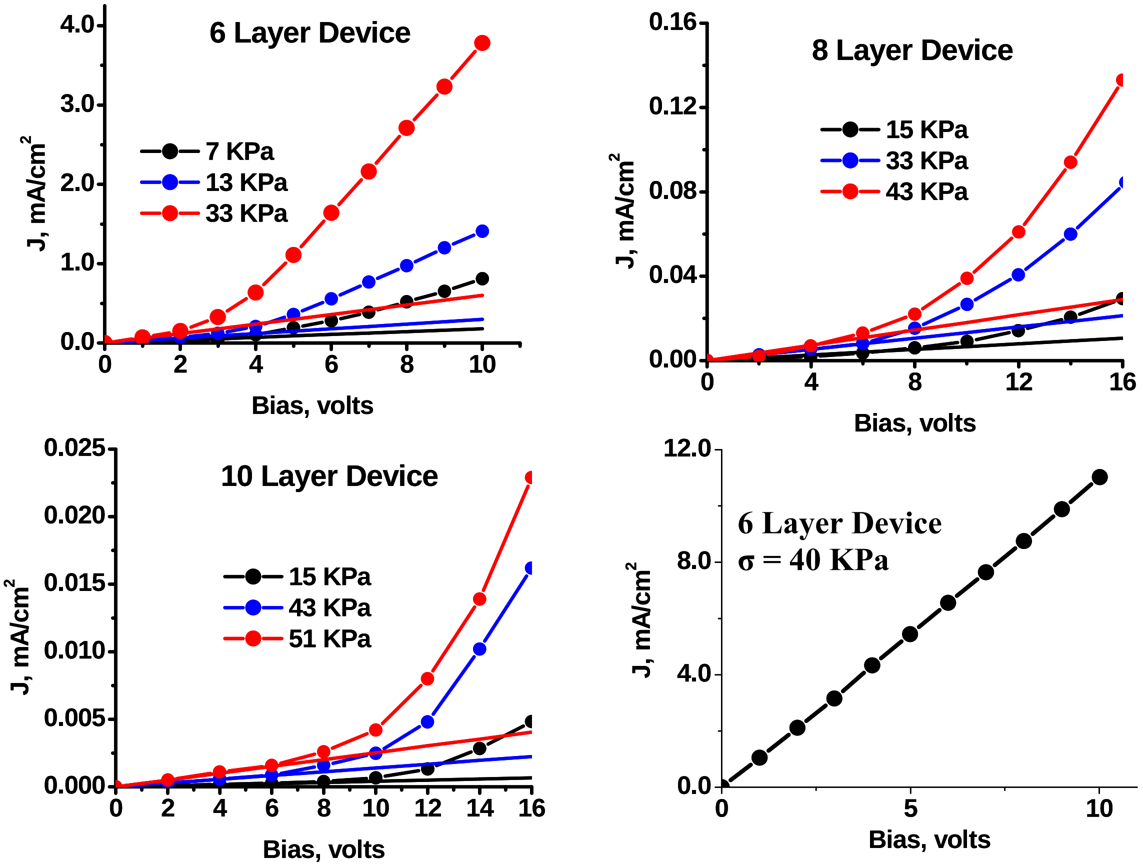

Figure 30 a, b & c. J-V data points for three σ. The fitted lines are based on the three parameter model, combining charge transport by electron tunneling and ions. The straight lines correspond to $J_{leakage}$. (a) 6 layer device response, (b) 8 layer device response and (c) 10 layer device response. (d) A reversible ohmic J-V response for a 6 layer device obtained at high load.

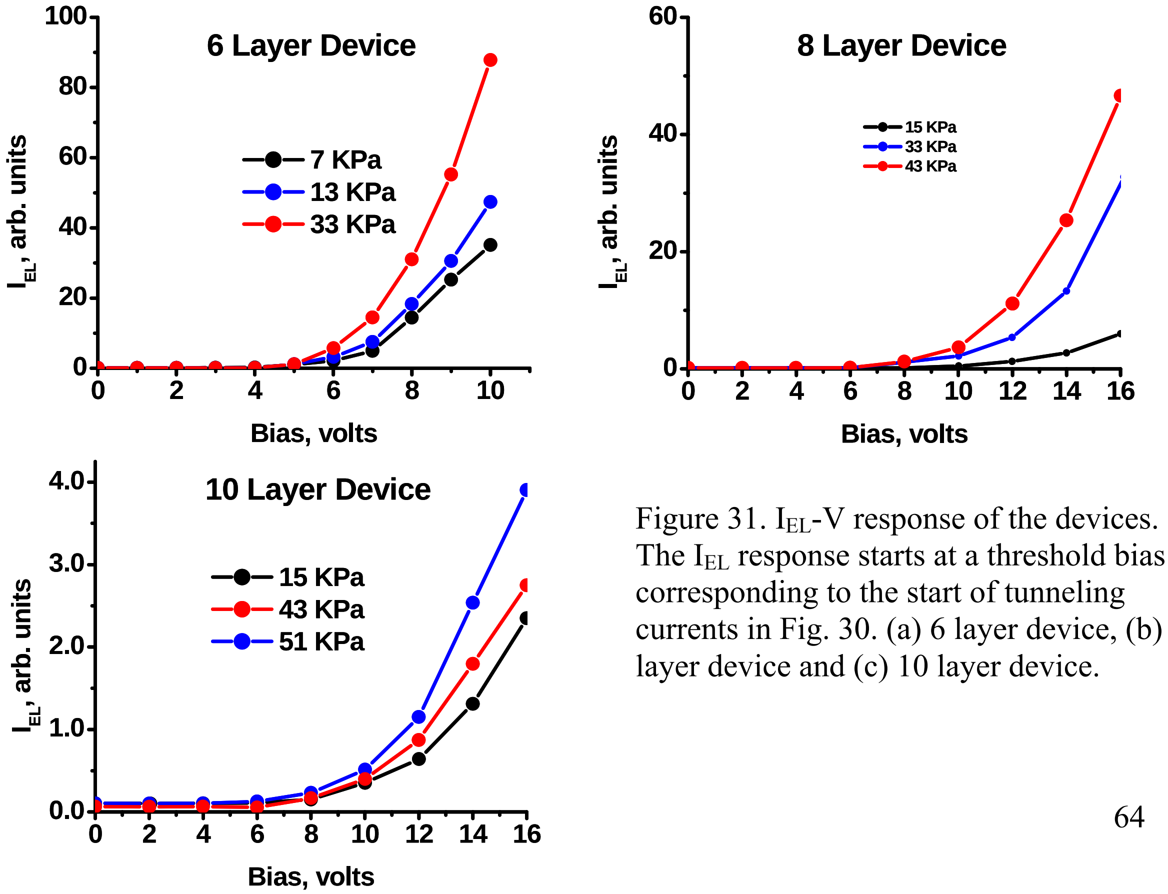

Figure 31. I_{EL}-V response of the devices. The I_{EL} response starts at a threshold bias corresponding to the start of tunneling currents in Fig. 30. (a) 6 layer device, (b) 8 layer device and (c) 10 layer device.

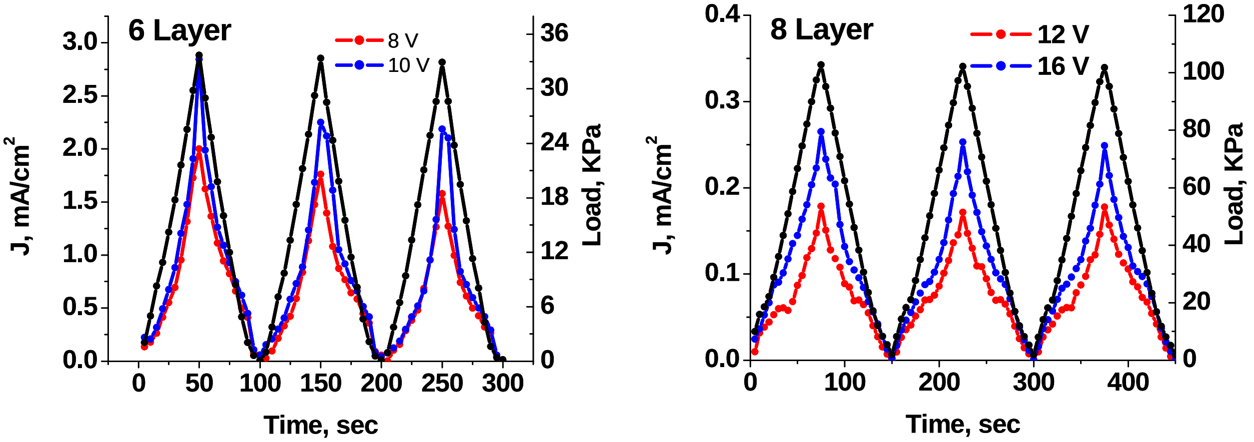

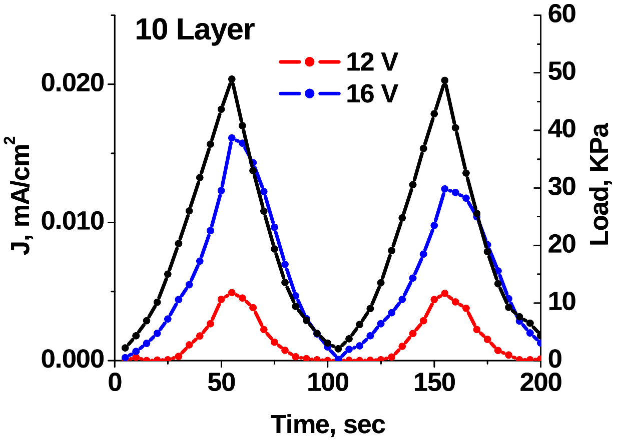

Figure 32. J-V response of the device to cyclic loading for different number of layers of dielectric: (a) 6 layer, (b) 8 layer and (c) 10 layer.

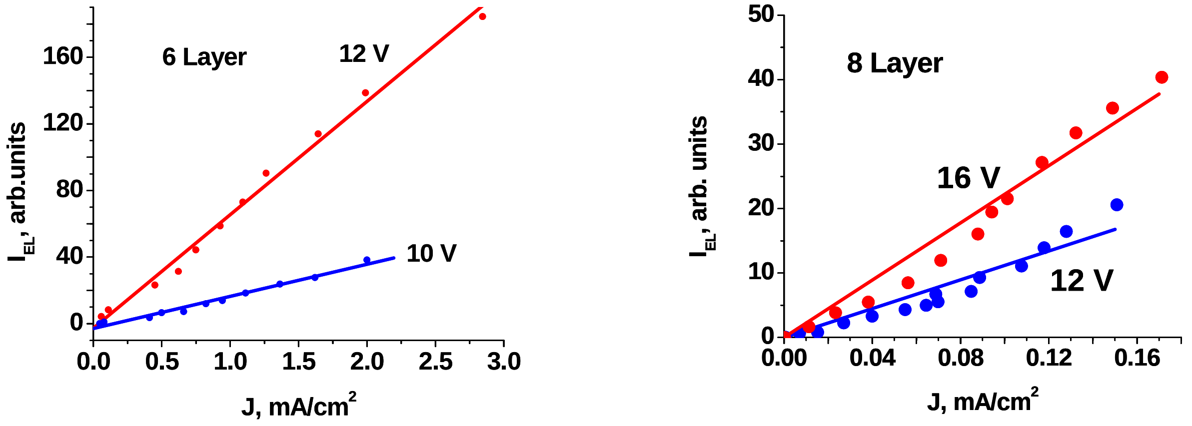

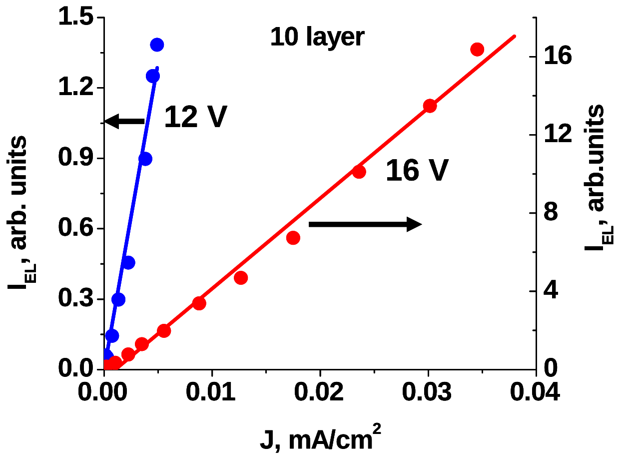

Figure 33. Comparison of electronic (i.e., current) and optical (i.e., electroluminescence) signals: I_{EL} is linearly proportional to J. Each data point is at fixed bias with varying σ. (a) 6 layer device, the two slopes are 17 & 66 (arb.units) cm^2/mA. (b) 8 layer device, the two slopes are 111.8 & 221.4 (arb.units) cm^2/mA (c) 10 layer device, the two slopes are 261 & 441.2 (arb.units) cm^2/mA. The efficiency of the device to convert current to electroluminescence increases with bias and number of DE layers as indicated by the slope.

The non-linear J-V response of the device is modeled as the sum of field assisted tunneling current, $J_{tunneling}$ given by the Fowler-Nordheim equation and leakage current, $J_{leakage}$ due to mobile ions present in the polyelectrolyte, the three parameter model. For the three data sets (6, 8 and 10 layers) the three parameter model (P, aK and R) is an excellent fit for the complete range of V and σ (Fig. 30 a, b & c), the straight lines show the corresponding leakage current. In the 8 & 10 layer devices tunneling currents start to dominate above 6-8 V as indicated by the increasing magnitude of difference between total current, J and leakage current, $J_{leakage}$. Measurable electroluminescence, I_{EL} resulting from purely tunneling current is observed above 6-8 V (Fig. 31 a, b & c), consistent with the domination of tunneling current above 6-8 V. The threshold for tunneling is reduced to 4 V for the 6 layer device, due to decreased barrier width, i.e. thickness of dielectric layers, for tunneling.

Consistent with increasing thickness of the dielectric layer i.e. larger R and barrier for tunneling, for identical bias and similar stresses the 10 layer device shows the lowest J and $I_{EL,}$ while the 6 layer device shows the highest. The 6 layer device is limited to stresses of 33 KPa, above which the response becomes ohmic (Fig. 30 d), this behavior is reversible. There is no observed electroluminescence for the ohmic response. The conjecture is that at larger stresses interpenetration of nanoparticle layers and formation of percolating channels lead to the ohmic response. The ohmic behavior occurs readily for the 6 layer device due to smaller separation between the nanoparticle layers. J decreases by more than two orders of magnitude on increasing the separation from 6 to 8 layers, on increasing to 10 layers J reduces further by an order of magnitude compared to the 8 layer device.

Stress cycles at constant bias show that J traces the load cycle, with nominal hysterisis (Fig. 32 a, b & c), indicating the robustness of device under continuous use. A linear behavior for J Vs I_{EL} is observed for the three devices (Fig. 33 a, b & c), at high bias and loading where the current is largely by tunneling. The linearity is due to I_{EL} being a result of tunneling current through CdS nanoparticle layers. Increasing the bias improves the efficiency of I_{EL} (i.e. conversion of current to electroluminescence), as observed from the larger value of slopes in these curves. The 10 layer device shows the highest efficiency for I_{EL} signifying greater transport through CdS layers, due to increased thickness of dielectric layer tunneling between the adjacent nanoparticle layers becomes the dominating transport mechanism.

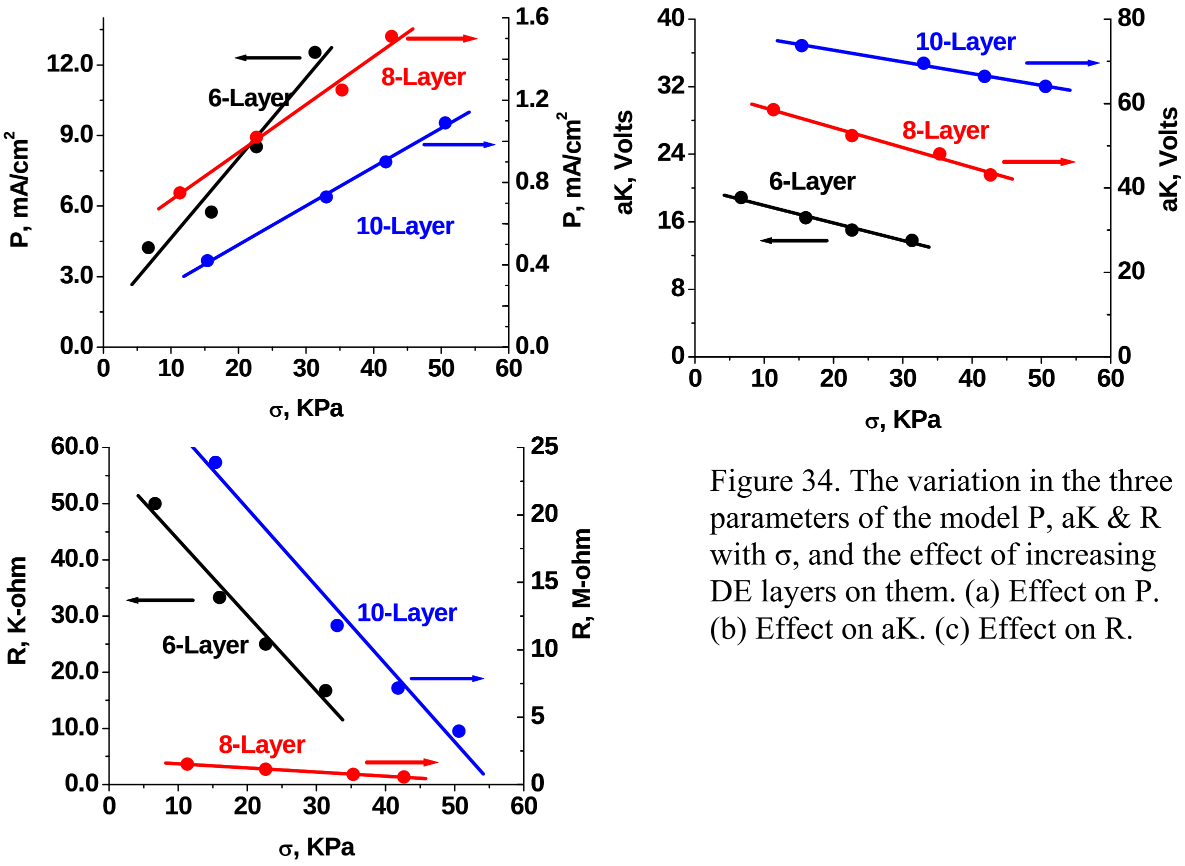

Figure 34. The variation in the three parameters of the model P, aK & R with σ, and the effect of increasing DE layers on them. (a) Effect on P. (b) Effect on aK. (c) Effect on R.

No. of DE Layers	P (mA/cm^2) σ (KPa)	aK (volts) σ (KPa)	R (ohm) σ (KPa)
6	$P = 0.0003\sigma + 0.0012$	$aK = 20 - 0.2072\ \sigma$	$R = 57091 - 1348\ \sigma$
8	$P = 2x10^{-5}\sigma + 0.0005$	$aK = 63.7 - 0.4717\ \sigma$	$R = 2x10^{6} - 30731\ \sigma$
10	$P = 2x10^{-5}\sigma + 0.0001$	$aK = 78.2 - 0.2771\ \sigma$	$R = 3x10^{7} - 577698\ \sigma$

Table 1. The linear relationship between the three parameters P, aK & R and stress (σ) for the 6, 8 & 10 layer devices.

The modeled parameters P, aK and R for the 6, 8 & 10 layer samples are self-consistent with varying σ (Fig. 34 a, b & c). P, signifying the electron density and no. of channels for tunneling increases linearly with increasing loads for the three samples. The increase in P can be attributed to increase in number of pathways for tunneling, as increasing σ presses the layers closer activating more particles as tunneling channels. The linear fits for P (Fig 34 a & Table 1) show that at σ = 0 KPa, the channels progressively decrease from 0.0012 to 0.0005 to 0.0001 mA/cm^2 with increasing DE layers 6, 8 & 10 respectively (Table 1). The decrease in initial active channels can be attributed to the increase in separation of nanoparticle layers. Further the rate of increase in P with σ is $3x10^{-4}$ $mA/(cm^2KPa)$ for 6 layer and this decreases by more than an order of magnitude to $2x10^{-5}$ $mA/(cm^2KPa)$ for 8 & 10 layers (Table 1). Similar rates of increase for the 8 & 10 layer device are consistent as the rate should not depend on the separation between the nanoparticle layers.

No. of DE Layers	I_{EL} (arb units) Vs J (mA/cm^2) Efficiency (10 V)	I_{EL} (arb units) Vs J (mA/cm^2) Efficiency (12 V)	I_{EL} (arb units) Vs J (mA/cm^2) Efficiency (16 V)
6	17	66	-
8		111.8	221.4
10	-	261	441.2

Table 2. Efficiency of the tactile sensor devices in conversion of current (J) to electroluminescence (I_{EL}).

The parameter 'aK', is the product of distance for tunneling between nanoparticle layers 'a', and the critical field for tunneling 'K'. K being a material characteristic should be identical in the three cases, as Au and CdS nanoparticles are used in all. The linear decrease in aK with σ for each device (Fig 34 b) is a result of compression of DE layers, reducing the distance for tunneling between the nanoparticle layers. The range of linearity observed corresponds to a change of ~30% for the 6 and 8 layer device and ~15% for the 10 layer device in aK. a_o, signifying the distance for tunneling between nanoparticle layers at $\sigma = 0$ KPa, increases by more than 3 times from 6 to 8 layer separation (20 to 64), where as from 8 to 10 layer the increase is only 1.25 times (64 to 78) (Table 1). R, the ohmic resistance due to presence of mobile ions in the device decreases linearly with applied σ (Fig 34 c).The fits show a significant increase in R_o (resistance at $\sigma = 0$) with increasing layers (Table 1). This is consistent with much higher efficiency of I_{EL} for the 10 layer device, as higher R_o results in increased transport of electrons through tunneling between the nanoparticle layers. Compared to the linear decrease in R with σ, the effect on $J_{tunnleing}$ is product of a linear (P) and exponential (aK) factor, this leads to the observed linearity in J and I_{EL} at high bias (cyclic loading plots, Fig 33 a, b & c) with dominant $J_{tunneling}$ currents over $J_{leakage}$.

2.5.2 Conclusion

The thickness of DE determines the separation between nanoparticle layers (the tunneling barrier), hence controlling $J_{tunneling}$. The magnitude of both $J_{tunneling}$ and I_{EL} for identical bias and loading decreases with thickness of DE layer, achieved by increasing the number of polyelectrolyte layers from 6 to 8 & 10. The efficiency of electroluminescence I_{EL} increases with thickness of dielectric layers (Table 2), signifying increasing dominance of tunneling transport through the CdS nanoparticle layers. At σ = 0 KPa, the 6 layer device shows significantly higher channels for tunneling (P) and a much lower width of tunneling barrier (a) in comparison to the 8 & 10 layer devices. The rate of increase in the channels for tunneling is 15 times higher in the 6 layer device compared to the 8 & 10 layer devices. The difference in 8 & 10 layer devices is coherent with increase in thickness of the DE barrier, as seen by the similar rate of increase in number of channels with σ and the increase in tunneling distance. Further the six layer device is limited to stresses of 33 KPa and bias of 10 V, above which ohmic response is observed, a result of formation of percolating channels for flow of leakage current. The conjecture is that the characteristics of the 6 layer device are due to the decrease of tunneling distances which lead to easy formation of continuous conducting channels on loading. The limitation in bias is expected due to a reversible break down resulting from absorbed water; the exact reason is not clearly understood.

The tactile sensor device presented here with its characteristics controlled by the thickness of polyelectrolyte layers and its functionality a result of its composition, presents an avenue to assemble quantum devices using ionic self assembly. The effect of DE thickness leads to a range of response from the device in terms of J, current and EL, electroluminescence. The DE thickness affects the bias and stress (loading) stimuli range to which the device can respond with acceptable magnitude. The results show that for a low load application the 6-layer device is more effective due to higher magnitude of response, similarly for very high loads we expect a 10-layer device will be used to avoid an ohmic response due to formation of percolating channels. The 8-layer device has the sensitivity comparable to human skin, with a measurable response under similar stress stimuli as used for tactile sensing by human skin.

2.6 Polyelectrolyte mineralization[*]

The assembly process for the device as described above consists of self-assembling four distinct materials in a layer-by-layer fashion. The materials are polyelectrolytes PAH (cationic due to amine functionality) and PSS (anionic, due to sulfonate functionality), metal nanoparticles (Au, 10 nm) and semi-conducting nanoparticles (CdS, ~3 nm). The process can be simplified by incorporating the functionality of PE (dielectric) and NP layers in a single composite structure of NPs mineralized on PE chains. The composite structure will have the functionality of both, NPs required as tunneling bases and the dielectric as tunneling barrier. The mineralization process will need to produce monodisperse NPs for efficient device performance. The underlying morphology of PE will critically govern the size and monodispersity of the NPs and their subsequent processing for device assembly. Mineralization of semiconducting CdS NPs on PSS is performed and based on the same concept a similar process for synthesizing Au NPs on PAH is also realized.

2.6.1 Concept: semiconducting nanoparticle synthesis

The template for mineralization is the “necklace-of-bead” morphology that PSS spontaneously forms under certain conditions in dilute solution, where the chains agglomerate to form microns long nanofibrils composed of nodular nano-sized beads sown together by polymer strands[78-80] (see Fig. 35). In the described process the nanoparticles are mineralized and stabilized in these beads.[128] Interestingly, the mineralization process can be repeated over three cycles by recharging the source

---

[*] Excerpts in this section are taken from reference 128. Copyright 2006 American Chemical Society.

compounds followed by precipitation in the beads without changing the polymer solution. The size of the particles after each precipitation process is identical. The final product is a stable nanofibrilar composite. The process is particularly robust as the size of the nanoparticles for a given polymer/solvent system is invariant over a broad range of concentration of the source salt relative to the polymer, molecular weight of the polymer, and reaction temperature. The particle size can be changed by using water/organic mixtures as the solvent. At a pH of < 1.0 and > 12.0 the polyelectrolyte chains do not form necklace-of-bead because they are neutral and highly charged respectively, under these conditions the mineralized CdS particles are in micron range and highly polydispersed.

2.6.2 Synthesis of semiconducting nanoparticles on polyelectrolyte 'polystyrene sulfonate'

$Cd(ClO_4)_2.H_2O$ is added to a 0.1% solution of PSS of molecular weight $5x10^5$ Daltons, at a molar ratio of 0.25 Cd^{2+} relative to $–SO_3^{-1}$, followed by stirring to form a clear solution. $Cd(ClO_4)_2$ has very low solubility in water, its dissolution in presence of PSS indicates strong interaction between Cd^{2+} and $–SO_3^{-1}$ groups on the PSS chains. CdS is formed by adding Na_2S to the solution of PSS-Cd at a relative molar ratio of 0.7 to Cd^{2+}, in dark and under N_2 atmosphere. The solution immediately turns light yellow indicating the formation of CdS nanoparticles. Further cycles of CdS synthesis are performed by repeating the procedure by adding fresh $Cd(ClO_4)_2.H_2O$ to the same solution.

2.6.3 Results and discussion: semiconducting nanoparticles

A step by step characterization of the process is performed using AFM, absorbance spectroscopy and TEM. The concept of the process is proposed from the analysis of the results and control experiments.

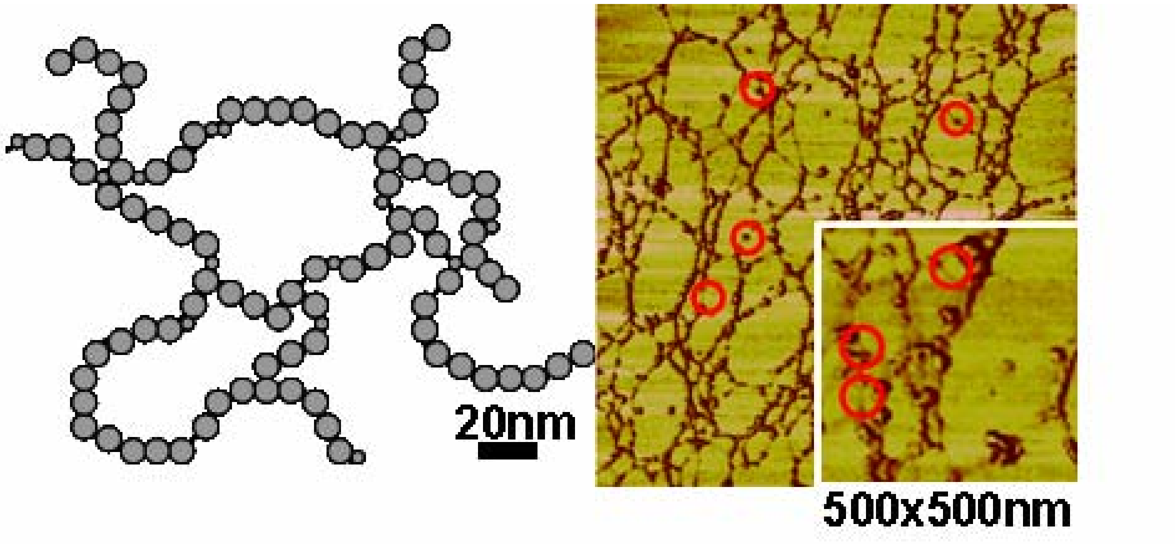

Figure 35. AFM image of pure PSS chains deposited from solution with schematics to aid the explanation of observed structure. Observed is the beaded necklace morphology. The main AFM image is 2 x 2 μm and the magnified one is 500 x 500 nm.

Fig. 35 is an AFM phase image of pure PSS deposited on a silica chip by dipping in a 0.1% PSS solution for 15 minutes, followed by immediate washing and air-drying. The morphology of the polymer chains on the chip should represent a close picture of their morphology in solution, as the chip is hydrophobic and the immediate washing and drying steps followed by AFM analysis should restrict the influence of substrate, mobility of the chains and the available time for their rearrangement on the substrate. The PSS chains form a necklace-of-beads, of typically 8-12 nm beads “stitched” together by polymer “tie” segments seen as fibrils between the beads, as marked in the AFM image (see Fig. 35). Fig. 35 also shows a schematic of the observed beaded structure morphology. Beaded morphology arises due to interactions between the hydrophobic parts of the chains and the long range columbic interaction among the ions on the chain and the counter-ions in the solution.[77-80]

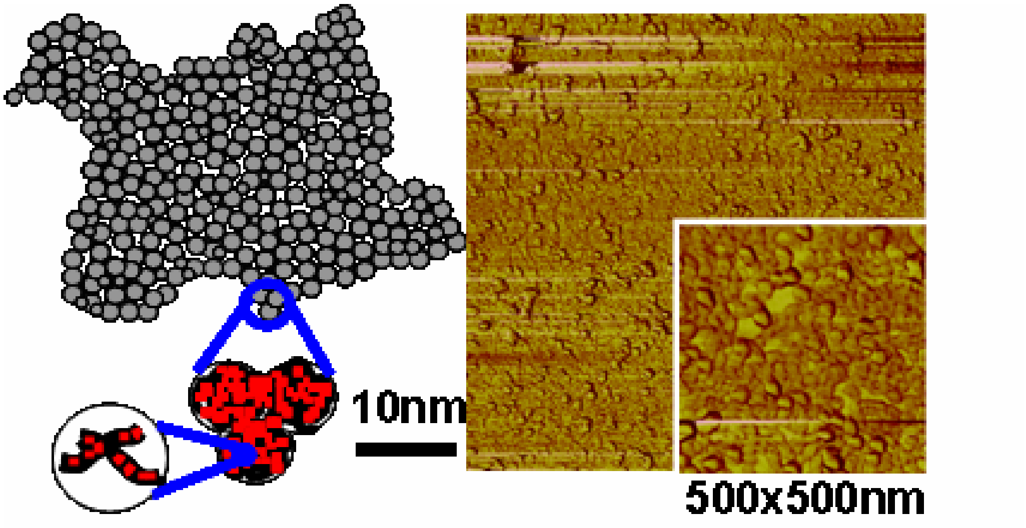

Figure 36. AFM image after adding $Cd(ClO_4)_2$ salt to PSS, with schematic to aid the explanation of observed structure. Observed is the collapsed beaded morphology. The main AFM image is 2 x 2 μm and the magnified one is 500 x 500 nm. The "red" dots are Cd^{2+}.

On addition of $Cd(ClO_4)_2$ at half the stoichiometric ratio relative to $–SO_3^-$ in PSS, the open necklace structure collapses to a densely packed agglomeration of beads as observed by AFM, shown in Fig. 36. The collapsed structure occurs due to ionic cross-linking of PSS chains within and among the beads, by electrovalent bonding between the divalent Cd^{2+} and $–SO_3^-$ ions on the polyelectrolyte. The case is similar to the binding of Cd^{2+} with $–COO^-$ in poly(acrylic acid).[129] In contrast, addition of a non-chelating ion (such as monovalent Na^+) only shields the negative charge on the PSS chain, resulting in a collapsed non-beaded structure.[78,130,131]

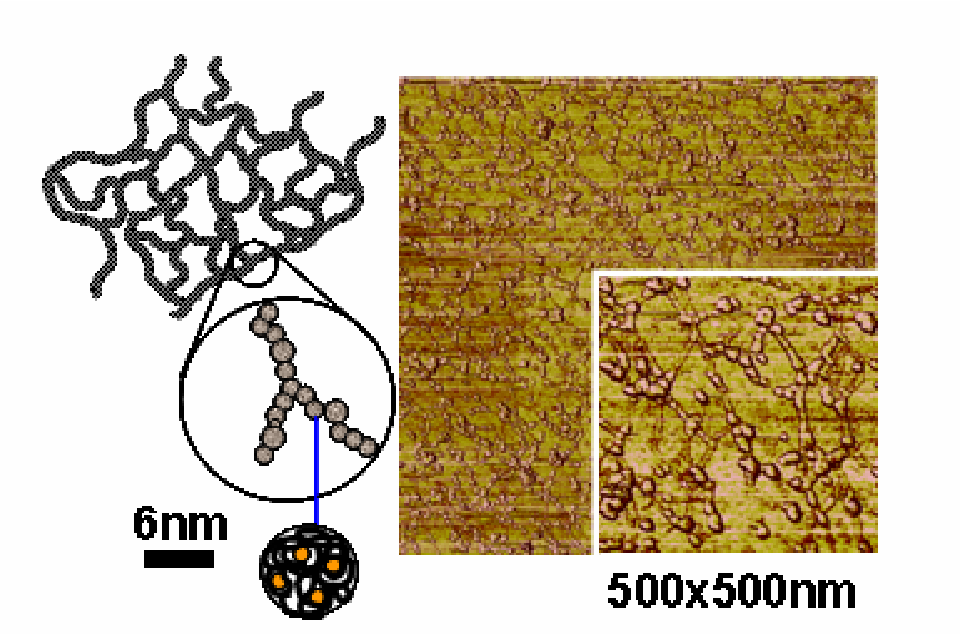

Figure 37. AFM image after addition of Na_2S to form CdS nanoparticles, with schematic to aid the explanation of observed structure. Observed is the continuous nano-fibril morphology. The main AFM image is 2 x 2 μm and the magnified one is 500 x 500 nm. The "golden" dots in the schematic represent CdS particles.

On addition of Na_2S to the Cd-PSS salt solution the necklace morphology reappears (see Fig. 37) similar to Fig. 35. However, the beads are not as discrete but form a continuous thick nano-fibril of width ~12 nm. TEM (see Fig. 38), where only the high-Z nanoparticles are visible, as CdS has a higher electron contrast than PSS (composed of carbon and hydrogen predominately) due to its higher atomic number, indicates that particles are imbedded in the nano-fibrils forming a necklace structure as schematically shown in Fig. 37.

The estimated diameter of the fibrils from TEM and AFM is 10-12 nm, while their length is in microns. As the Cd^{2+} forms CdS nanoparticles the ionic cross-linking density is diminished by more than an order of magnitude, causing the agglomerated beaded structure to exfoliate. Concomitantly, the $-SO_3^-$ ions that were electrovalently bound to

Cd^{2+} are released on formation of CdS. On further addition of $Cd(ClO_4)_2$, the unbounded $–SO_3^-$ serve as synthesis sites for the next cycle of CdS nanoparticles.

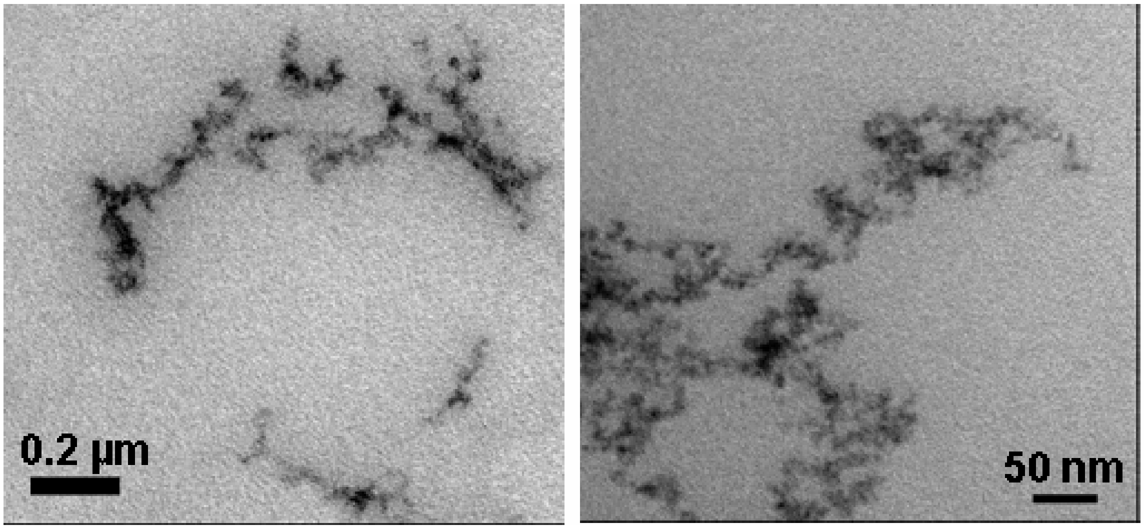

Figure 38. TEM image after the addition of Na_2S to form CdS nanoparticles. The high Z CdS nanoparticles appear as dark regions embedded in a light fibrillar structure formed by PSS.

To obtain a clear image of the nanoparticles, the CdS particles are extracted by adding dodecanethiol to the nano-fibril CdS/PSS composite suspension followed by 1 hour of sonication and subsequent removal of the particles by centrifuge-separation and re-suspension in heptane. As shown in Fig. 39a TEM image, the particles have a uniform size distribution, with diameter of ~4 nm. Fig. 39b shows a sharp excitonic peak in the UV-Vis absorption spectrum of the nano-fibril PSS-CdS composite, indicating a narrow size distribution of the CdS nanoparticles. The excitonic peak in Fig. 39b is invariant over first three cycles indicating that the size of the nanoparticles is invariant (as also confirmed by TEM). In the fourth cycle the absorption spectrum shifts to higher wavelengths and broadens, indicating formation of larger size particles with a broad size distribution. The highly blue shifted excitonic peak for synthesis in 95% DMF in water will be discussed later. For quantitative comparison of absorption spectra, all the samples are diluted to identical Cd^{2+} concentration.

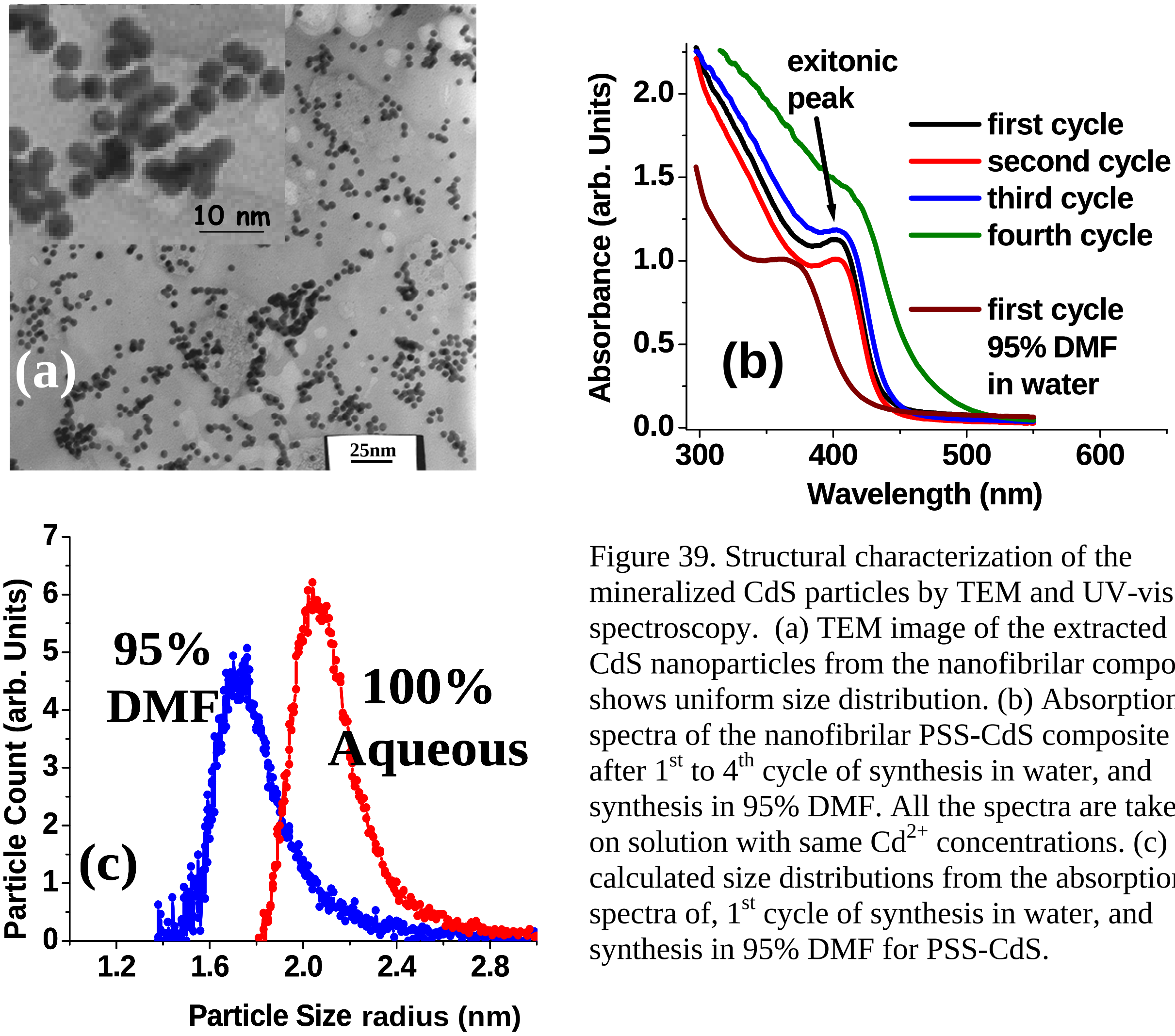

Figure 39. Structural characterization of the mineralized CdS particles by TEM and UV-vis spectroscopy. (a) TEM image of the extracted CdS nanoparticles from the nanofibrilar composite shows uniform size distribution. (b) Absorption spectra of the nanofibrilar PSS-CdS composite after 1st to 4th cycle of synthesis in water, and synthesis in 95% DMF. All the spectra are taken on solution with same Cd^{2+} concentrations. (c) The calculated size distributions from the absorption spectra of, 1st cycle of synthesis in water, and synthesis in 95% DMF for PSS-CdS.

The sharp exciton peak at 412 nm is characteristic of a narrow size distribution for semiconducting nanoparticles. The absorption edge at 435 nm, using the effective mass approximation[132] provides an estimated size of ~4 nm for the particles. For a dilute suspension of nanoparticles, Fig. 39c shows the calculated size distribution from the absorption spectra.[133] Although the synthesis is in “bulk” with no micellar morphology, the distribution in Fig. 39c is remarkably narrow, and the mean size of ~4 nm is consistent with TEM image in Fig. 39a. The second distribution in Fig. 39c corresponding to synthesis in DMF (95%) is discussed later. The ultimate molar yield of CdS after 3 cycles is about 0.75 times the sulfonate groups in PSS.

The robustness of the process in producing monodisperse particles is attributed to the following characteristics: (i) Decreasing the initial mole ratio of Cd^{2+} relative to $–SO_3^-$ from 0.25 to 0.025 does not change the size and distribution of the particles. (ii) Synthesis using PSS with 7 fold smaller molecular weight (i.e., $7x10^4$ Dalton) with similar necklace-of-bead morphology yields identical results. (iii) Decreasing the reaction temperature in the range of 24^OC to 6^OC with varying reaction times does not affect the nanoparticle distribution or size.

The critical role of beaded morphology is confirmed by two sets of experiments: (i) Synthesis using identical concentration and ratio of styrene sulfonate monomer (SSM)/$Cd(ClO_4)_2$ as PSS/$Cd(ClO_4)_2$ yields bulk CdS. (ii) Changing the pH of the PSS solution from 8 to <1 or >12 that disrupts the formation of necklace-of-bead morphology and results in highly polydispersed micron size particles of CdS.

The conjecture is that the size control and narrow distribution of CdS nanoparticles in the PSS template results from its nanoscale necklace-of-bead morphology. On addition of $Cd(ClO_4)_2$, the Cd^{2+} ions diffuse uniformly in the beads, reaching an equilibrium concentration. Subsequently on addition of Na_2S, its rapid diffusion into the nanoscale beads initiates a perfect heterogeneous nucleation of CdS from the Cd^{2+} ions present in the beads. The chelation of Cd^{2+} to $–SO_3^-$ groups on the polymer chain reduces the ion diffusion preventing large agglomeration of CdS. Each bead thus acts as a batch-reactor, leading to the uniform size of CdS nanoparticles and the beaded-necklace morphology. The reappearance of beaded-chain morphology in PSS-CdS nanocomposite at the end of synthesis allows for an identical second (and third) cycle of nanoparticle synthesis.

As noted above, an interesting characteristic of the mineralization process is its invariance of particle size distribution. To change the particle size, the morphology of polyelectrolyte superstructure needs to be altered significantly. As the necklace-of-bead morphology is highly sensitive to the quality of solvent,[80,134] the hydrophilicity of the solvent is decreased by replacing water with 95% aqueous solution of dimethylformamide (DMF), in the initial PSS solution. The result is 3.4 nm CdS nanoparticles as seen by the blue-shift in the absorbance spectrum of Fig. 39b, while the size distribution is still narrow as seen in Fig. 39c. The necklace-of-bead morphology for the DMF based system is highly collapsed with more dense beads due to decreased hydrophilicity of the solvent.[135]

2.6.4 Result and discussion: Au nanoparticles on Polyelectrolyte ‘Polyallylamine Hydrochloride’

The synthesis of Au nanoparticles is performed in a similar fashion, but as the polyelectrolyte PAH does not form a necklace of beads but has a morphology of small beads (1-2 nm in size) due to its lower molecular weight (70,000 Daltons instead of 500,000 Daltons of PSS) and greater flexibility of its backbone compared to that of PSS, a slightly modified scheme is followed.

For synthesis, 0.1% solution (by weight) of PAH (M_w of 70,000 Daltons) in DI water is mixed with gold salt $HAuCl_4$, ratio of Au to amine groups being 1:10. After stirring for 12 hours, the solution is added to DMF, bringing the final water content of the solution to 4%. The solution is then reduced with sodium borohydride ($NaBH_4$). The yellow PAH-Au solution immediately turns wine red indicating the formation of Au nanoparticles. The absorption spectrum (Fig. 40) which shows a surface plasmon absorbance peak at 530 nm, characteristic of Au nanoparticles confirms the formation of nanoparticles. For comparison Fig. 40 also shows the spectrum for commercially purchased Au 10 nm particles. In the PAH-Au nanocomposite also observed is the PAH absorbance peak at ~260 nm.

The TEM images show that Au nanoparticles are formed inside the PAH nanobeads (Fig. 41a). The amine groups bind with Au, confining them to the PAH nanobeads and restricting their size to nanometer scale on reduction with $NaBH_4$. For comparison TEM of commercially purchased 10 nm Au particles is also shown in Fig. 41b.

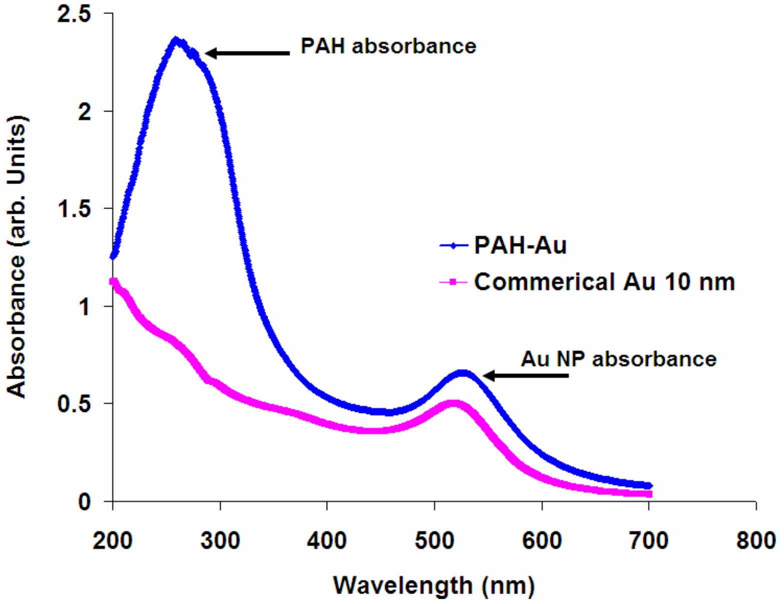

Figure 40. Absorbance spectra of PAH-Au nanocomposite and commercially purchased 10 nm Au nanoparticles. The surface plasmon absorbance of Au nanoparticles at ~530 nm is observed in both the samples. The nanocomposite also shows the PAH absorbance at ~260 nm.

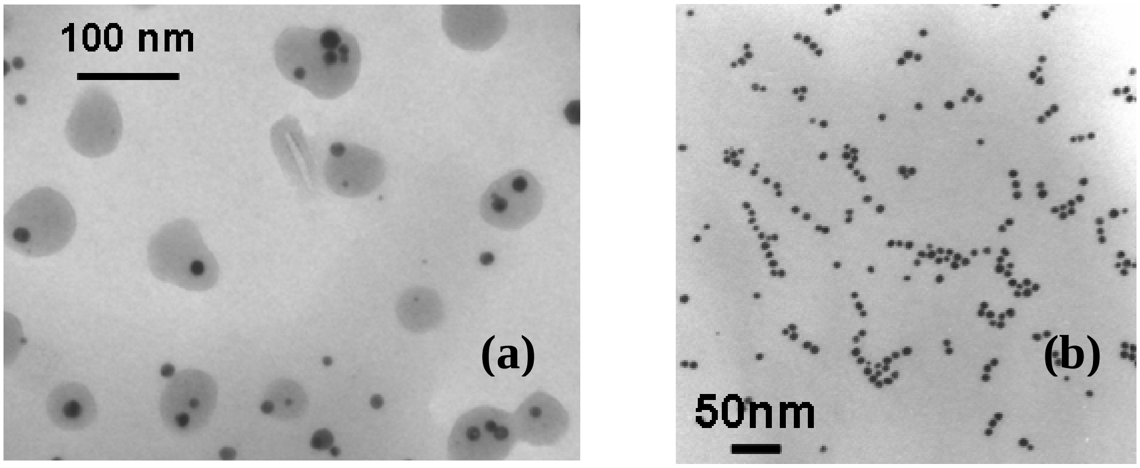

Figure 41. (a)TEM images of PAH-Au nanocomposite, the Au nanoparticles of ~10 nm are mostly confined to ~50 nm PAH beads. (b) Images of commercially purchased 10 nm Au nanoparticles.

2.6.5 Results and discussion: multi-composite of metal-semiconducting nanoparticles on polyelectrolyte

The goal of synthesizing a single composite consisting of the beads of PAH with Au nanoparticles, imbedded in a matrix of PSS with CdS nanoparticles is also achieved.

The structure of the multifunctional composite is synthesized with a modified scheme. 0.1% solution (by weight) of PAH (M_w of 70,000 Daltons) in DI water is mixed with gold salt $HAuCl_4$, ratio of Au to amine groups being 1:10. The solution is then mixed with DMF, to achieve a final water content of 2% in DMF. Reducing with $NaBH_4$ after stirring for 12 hours, results in formation of Au nanoparticles. To this solution is added a solution made in DI water consisting of 2% PSS (M_w of $5x10^5$ Daltons), with $Cd(ClO_4)_2.H_2O$ at a molar ratio of 0.25 Cd^{2+} relative to $–SO_3^{-1}$, increasing the final water content in DMF to 4%. The solution after stirring for 12 hours is reduced with Na_2S leading to the formation of CdS nanoparticles. The absorbance spectra (Fig. 42), which shows the signature of both Au and CdS nanoparticles with absorbance peaks at 530 nm and 420 nm respectively, along with absorbance at 260 nm from PSS and PAH confirms the formation of NPs. The structure of Au loaded PAH beads covered with PSS loaded with CdS is confirmed by TEM (Fig. 43). The beads ~800 nm in size have highly dense structure, which cannot be penetrated by the TEM electron beam (Fig. 43a). The solution is hence diluted to 50% water and subsequently imaged with TEM (Fig. 43b and its inset), the Au loaded PAH beads have a darker contrast due to high Z of Au, and are imbedded in lighter PSS-CdS matrix.

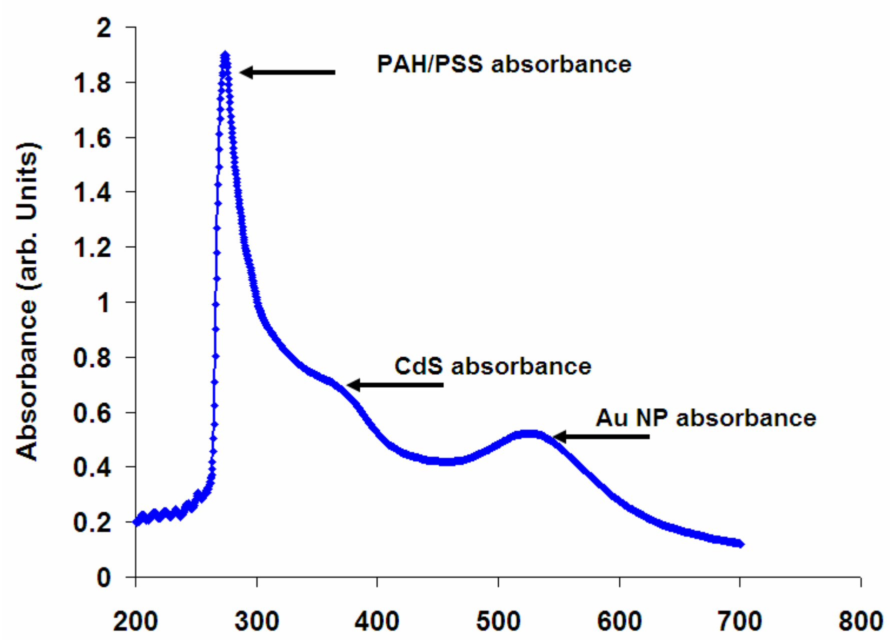

Figure 42. Absorbance spectra of PAH-Au core and PSS-CdS matrix nanocomposite. Observed is the surface plasmon absorbance of Au nanoparticles at ~530 nm and CdS nanoparticle absorbance due to bandgap at 420 nm. PAH and PSS absorbance is observed at ~260 nm.

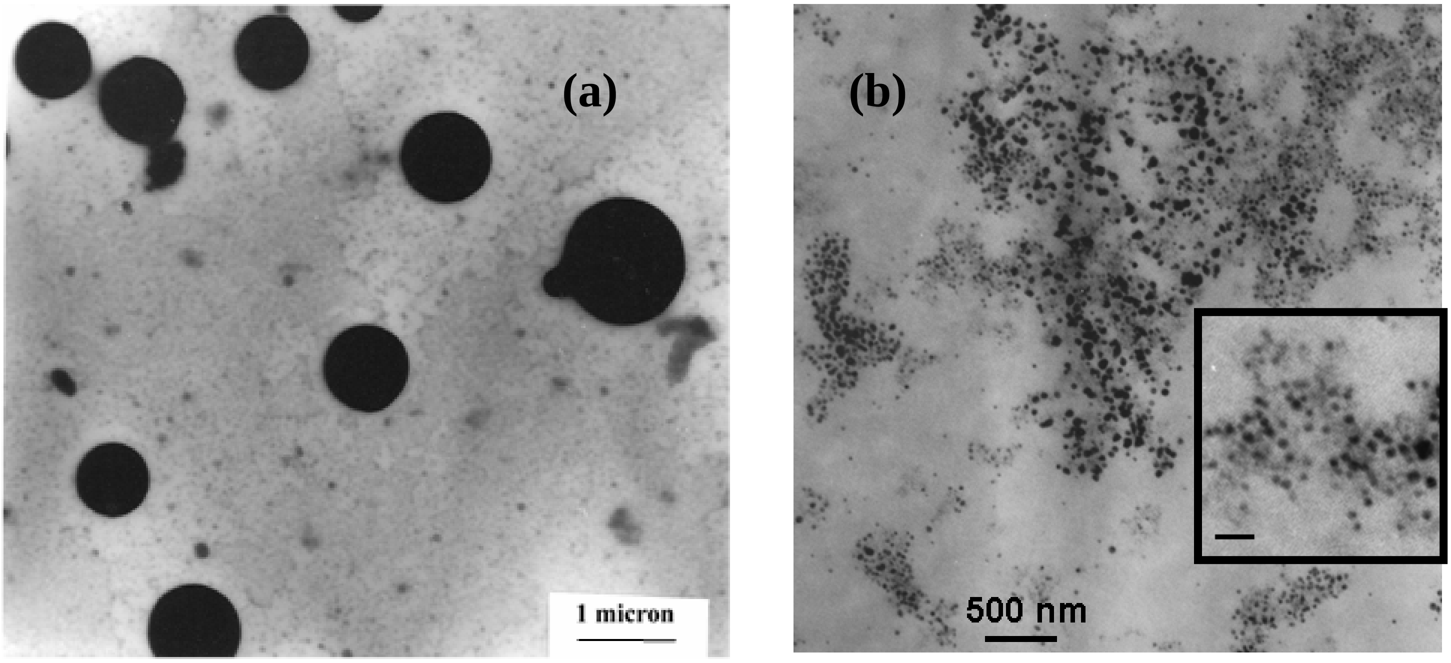

Figure 43. (a) TEM images of PSS-CdS-PAH-Au nanocomposite. Spherical, dense beads of ~800 nm are seen. (b) The exfoliated structure after addition of water shows PAH-Au beads imbedded in PSS matrix. The inset in (b) shows a magnified view of the exfoliated structure, the scale bar is 200 nm.

2.6.6 Conclusion

Synthesis through a robust and simple non-micellar route has been performed for mineralizing monodisperse CdS nanoparticles on a nanoscale superstructure (i.e., necklace-of-bead) of polyelectrolyte formed in dilute aqueous solutions. The size of particles synthesized in the nanosized beads is unchanged for a broad range of conditions, for a fixed polymer/solvent system. The size of the nanoparticles can be altered by changing the hydrophilicity of the solvent, such as by the addition of a polar organic solvent. On replacing pure water with 95% DMF the diameter of CdS particles is reduced from ~4 nm to 3.4 nm. The resultant mineralized nanofibrilar PSS/CdS composite is a stable suspension in solvent for over a week when stored in dark. The process is particularly robust to synthesize identical size monodisperse nanoparticles over three cycles of mineralization on the same polyelectrolyte solution to obtain highly filled nanofibrilar composite with a CdS to PSS-monomer molar ratio of ~0.75.

The approach is then extended for synthesis of Au nanoparticles in PAH beads. The result is a nanocomposite of PAH beads loaded with Au nanoparticles. Synthesis of the metal NP-polyelectrolyte and semiconducting NP-polyelectrolyte composite should simplify the fabrication of device by using the two functional materials instead of four separate species, significantly reducing the assembly time and effort. Further the nanocomposites should be interesting materials for application in bio-mimetics and for study of their optical, electronic and mechanical properties with possible applications in electronic devices, sensors, solar energy conversion and as imaging tags.

Conclusions

The successful assembly of a tactile sensor device based on electron tunneling, with its resolution and sensitivity comparable to that of human skin has been accomplished. The lateral and height resolution of 20 μm and 5 μm for its tactile sensing are akin to that of human skin, 40 μm and 2 μm, respectively. The achieved resolution is ~50 times better than current large area (greater than 1 cm^2) tactile sensors. The response is achieved at 9 KPa loading well within the 10 - 40 KPa range used by human finger for tactile sensing. For a signal to noise ratio of 5 in electroluminescence, the stress sensitivity of the device is 9 KPa. The device characteristics are presented by capturing the electroluminescence image from tactile sensing on a CCD camera. Fabrication of an electronic readout is achievable with similar quality of response.

The device is assembled with a layered architecture and is composed of nanoparticle layers separated by dielectric polyelectrolyte media. The device principle is based on electron tunneling. The exponential dependence of tunneling to the modulation in thickness of dielectric barrier by applied stress results in the tactile sensitivity of the device. The high resolution in tactile sensing arises from the discreetness in device structure with nanoparticles functioning as the base for tunneling electrons. The process of fabrication is based on self-assembly using layer-by-layer method of polyelectrolytes, requiring no complex lithography, making it easier to build the device on large areas and complex shapes.

A three parameter model based on the combination of electron tunneling currents and ohmic ionic currents is used to characterize the device response. The model is an excellent fit and is self–consistent in explaining the modulation of device response to applied loads. The effect of dielectric thickness is quantified by characterizing the device response for 6, 8 and 10 layer dielectric devices. The analysis presents that dielectric layer thickness can be used to control the range of stress magnitude to which the device has a measurable response. Separation of 6 layers (~7 nm) leads to significant interpenetration of nanoparticle layers. The 8 layer device resembles closely the human skin in its sensitivity of response and resolution for tactile sensing.

The assembly process is proposed to be simplified by combining the functionality of nanoparticles (the tunneling media) with polyelectrolytes (the dielectric) in a single composite material. Synthesis of monodisperse semiconducting CdS nanoparticles has been shown using the unique beaded-necklace morphology of polyelectrolyte. The nanoscale beads act as batch reactors leading to uniformity in size of nanoparticle. Three cycles of synthesis can be performed on the template yielding identical size particles in each cycle. The final product is a percolating nanofibrilar composite, comprised of polyelectrolyte and semiconducting nanoparticles. The size of the particles can be modified by altering the morphology of the polyelectrolyte. A similar modified approach has been used to synthesize gold nanoparticles in beaded polyelectrolyte morphology. Further the metal-semiconducting-dielectric functionality is combined in a single composite structure. These materials should simplify the assembly process of the device and present novel material for further electro-optical studies.

Future work

Tactile sensor

Development of the tactile sensor device now leads to future possibilities that are important for further advancing and improving the device capabilities. The areas for further concentration of research can be divided into two groups: fabrication and materials, and applications.

Fabrication and materials

The device has been assembled with semiconducting material cadmium sulfide, an important step is to study the effect of using other group II-VI semiconductors like CdSe, CdTe, ZnS and ZnO. The variation in bandgap of the semiconducting layer should affect the threshold bias for electroluminescence, the color of emission and its intensity (or efficiency). The goal is to make the electroluminescence intense enough to be visible to the human eye.

The device has been assembled using polyelectrolytes, which leads to ionic currents. The ionic currents reduce the sensitivity of the device to stresses as they vary linearly with loads compared to the exponential sensitivity of tunneling currents. Further ionic currents do not result in electroluminescence, reducing the efficiency of current to light conversion. Assembly of the layered structure using non-ionic species such as thiol, or molecular linkers should eliminate ionic currents increasing the sensitivity and efficiency of the device.

Applications

The device has been presented as a tactile sensor with capabilities akin to human skin in resolution and sensitivity. The next step is to use the device in robotic systems with an electronic readout interface, providing sense of touch to artificial intelligence systems. The sensor can also be used for pressure imaging in smart floors and housing giving a dynamic map of human activity leading to real time decisions on energy saving.

An important application is in the use of the device as a bio-imaging sensor. The resolution in microns should provide cell level imaging on tissue samples and with the ability to detect hardness difference, allowing cancer and tumor detection with ease and at high resolution without the need of bio-analytical methods. The use can be further extended to study the efficacy of drugs in treating tumors. The same concept can be extended in long term (and after considerable effort) to develop a non-invasive surgical probe to give surgeons the sense of touch inside human body.

Interactions in dielectric layers can be used to alter the tunneling characteristics of the device by changes in dielectric constant, modulus, and interface coupling with the nanoparticle layers. The sensitivity could lead to application in chemical detection and biomolecular sensing.

Temperature sensing using the effect of thermal activation on tunneling needs to be quantified for possible application of the device as a thermal sensor, increasing its multifunctional sense akin to human skin.

Polyelectrolyte mineralization: nanocomposite

The nanocomposite materials prepared using the polyelectrolyte template with synthesis of metallic and semiconducting nanoparticles on it, provides a multifunctional species for assembly of the device. Fabrication and characterization of a device using the nanocomposite needs to be performed. The materials need to be characterized, by studying their electro-optical response and as systems to model synthesis of more diverse composites.

References

1. G. Robles-De-La-Torre and V. Hayward, *Nature*, 2001, **412**, 445-448.

2. P. N. Brett and R. S. Stone, *Proc.Inst.Mech.Eng [H.]*, 1997, **211**, 309-316.

3. S. Matsumoto, R. Ooshima, K. Kobayashi, N. Kawabe, T. Shiraishi, Y. Mizuno, H. Suzuki, and S. Umemoto, *Surgical Endoscopy-Ultrasound and Interventional Techniques*, 1997, **11**, 939-941.

4. P. K. Plinkert, I. Baumann, and E. Flemming, *Laryngorhinootologie*, 1997, **76**, 543-549.

5. N. Sakai, M. Tatsuta, H. Yano, H. Iishi, and S. Ishiguro, *Gastrointestinal Endoscopy*, 2000, **51**, 69-73.

6. O. Tohyama, S. Maeda, and H. Itoh, *Ieee Journal of Selected Topics in Quantum Electronics*, 1999, **5**, 115-118.

7. P. Dario, E. Guglielmelli, and C. Laschi, *Journal of Robotic Systems*, 2001, **18**, 673-690.

8. Y. Okumura, T. Tawara, T. Furuta, K. Endo, M. Shimizu, M. Shimomura, and H. Kitano, *Advanced Robotics*, 2004, **18**, 699-710.

9. Y. B. Jia, *Ieee Transactions on Robotics*, 2005, **21**, 726-733.

10. M. Kaneko and K. Tanie, *Ieee Transactions on Robotics and Automation*, 1994, **10**, 355-367.

11. A. M. Okamura and M. R. Cutkosky, *International Journal of Robotics Research*, 2001, **20**, 925-938.

12. R. Tajima, S. Kagami, M. Inaba, and H. Inoue, *Advanced Robotics*, 2002, **16**, 381-397.

13. M. Shikida, T. Shimitzu, K. Sato, and K. Itoigawa, *Sensors and Actuators A-Physical*, 2003, **103**, 213-218.

14. J. Engel, J. Chen, and C. Liu, *Journal of Micromechanics and Microengineering*, 2003, **13**, 359-366.

15. R. D. Howe and M. R. Cutkosky, *Ieee Transactions on Robotics and Automation*, 1993, **9**, 140-151.

16. D. De Rossi, F. Carpi, and E. P. Scilingo, *Advances in Colloid and Interface Science*, 2005, **116**, 165-178.

17. C. Domenici and D. Derossi, *Sensors and Actuators A-Physical*, 1992, **31**, 97.

18. T. Someya, T. Sekitani, S. Iba, Y. Kato, H. Kawaguchi, and T. Sakurai, *Proceedings of the National Academy of Sciences of the United States of America*, 2004, **101**, 9966-9970.

19. J. W. Morley, A. W. Goodwin, and I. Darian-Smith, *Experimental Brain Research*, 1983, **49**, 291-299.

20. R. S. Johansson and R. H. LaMotte, *Somatosensory Reserach*, 1983, **1**, 21-31.

21. S. A. Mascaro and H. H. Asada, *Ieee Transactions on Robotics and Automation*, 2001, **17**, 698-708.

22. Kasap, O. P. Principles of Electrical Engineering Materials and Devices. Revised Edition, 151-288. 2000. Mc Graw Hill.

23. M. Arndt, O. Nairz, J. Vos-Andreae, C. Keller, G. van der Zouw, and A. Zeilinger, *Nature*, 1999, **401**, 680-682.

24. G. Gamow, *Nature*, 1929, **123**, 606.

25. R. H. fowler and Nordheim L., *Proceedings of the Royal Society of London Series A.*, 1928, **119**, 173-181.

26. G. binning, H. Rohrer, Ch. Gerber, and E. Weibel, *Physical Review Letters*, 1982, **49**, 57-61.

27. J. Y. Ouyang, C. W. Chu, C. R. Szmanda, L. P. Ma, and Y. Yang, *Nature Materials*, 2004, **3**, 918-922.

28. V. Maheshwari, R.F. Saraf, Science, 2006, 312, 1501-1504.

29. V. Berry and R. F. Saraf, *Angewandte Chemie-International Edition*, 2005, **44**, 6668-6673.

30. E. M. Conwell, *Proceedings of the National Academy of Sciences of the United States of America*, 2005, **102**, 8795-8799.

31. B. Giese, J. Amaudrut, A. K. Kohler, M. Spormann, and S. Wessely, *Nature*, 2001, **412**, 318-320.

32. D. N. Beratan, J. N. Onuchic, J. R. Winkler, and H. B. Gray, *Science*, 1992, **258**, 1740-1741.

33. H. Pelletier and J. Kraut, *Science*, 1992, **258**, 1748-1755.

34. U. Diebold, J. F. Anderson, K. O. Ng, and D. Vanderbilt, *Physical Review Letters*, 1996, **77**, 1322-1325.

35. M. Valden, X. Lai, and D. W. Goodman, *Science*, 1998, **281**, 1647-1650.

36. G. Decher, *Science*, 1997, **277**, 1232-1237.

37. N. Kato, P. Schuetz, A. Fery, and F. Caruso, *Macromolecules*, 2002, **35**, 9780.

38. M. Koetse, A. Laschewsky, B. Mayer, O. Rolland, and E. Wischerhoff, *Macromolecules*, 1998, **31**, 9316-9327.

39. F. Caruso, D. Trau, H. Mohwald, and R. Renneberg, *Langmuir*, 2000, **16**, 1485-1488.

40. J. H. Rouse and P. T. Lillehei, *Nano Letters*, 2003, **3**, 59-62.

41. G. Decher, B. Lehr, K. Lowack, Y. Lvov, and J. Schmitt, *Biosensors & Bioelectronics*, 1994, **9**, 677-684.

42. C. Y. Jiang, S. Markutsya, and V. V. Tsukruk, *Langmuir*, 2004, **20**, 882-890.

43. A. Mamedov, J. Ostrander, F. Aliev, and N. A. Kotov, *Langmuir*, 2000, **16**, 3941-3949.

44. J. Cho, K. Char, J. D. Hong, and K. B. Lee, *Advanced Materials*, 2001, **13**, 1076.

45. Z. Y. Tang, N. A. Kotov, S. Magonov, and B. Ozturk, *Nature Materials*, 2003, **2**, 413-428.

46. A. B. Artyukhin, O. Bakajin, P. Stroeve, and A. Noy, *Langmuir*, 2004, **20**, 1442.

47. K. E. Van Cott, M. Guzy, P. Neyman, C. Brands, I. R. Heflin, H. W. Gibson, and R. A. Davis, *Angewandte Chemie-International Edition*, 2002, **41**, 3236.

48. C. Y. Jiang, S. Markutsya, Y. Pikus, and V. V. Tsukruk, *Nature Materials*, 2004, **3**, 721-728.

49. D. Cochin, M. Passmann, G. Wilbert, R. Zentel, E. Wischerhoff, and A. Laschewsky, *Macromolecules*, 1997, **30**, 4775-4779.

50. D. M. DeLongchamp and P. T. Hammond, *Chemistry of Materials*, 2003, **15**, 1165-1173.

51. P. K. H. Ho, J. S. Kim, J. H. Burroughes, H. Becker, S. F. Y. Li, T. M. Brown, F. Cacialli, and R. H. Friend, *Nature*, 2000, **404**, 481-484.

52. G. Decher, M. Eckle, J. Schmitt, and B. Struth, *Current Opinion in Colloid & Interface Science*, 1998, **3**, 32-39.

53. A. V. Dobrynin, A. Deshkovski, and M. Rubinstein, *Macromolecules*, 2001, **34**, 3421-3436.

54. S. T. Dubas and J. B. Schlenoff, *Macromolecules*, 1999, **32**, 8153-8160.

55. M. muthukumar, *Journal of Chemical Physics*, 1987, **86**, 7230-7235.

56. M. Losche, J. Schmitt, G. Decher, W. G. Bouwman, and K. Kjaer, *Macromolecules*, 1998, **31**, 8893-8906.

57. A. V. Dobrynin, *Journal of Chemical Physics*, 2001, **114**, 8145-8153.

58. A. M. Belcher, X. H. Wu, R. J. Christensen, P. K. Hansma, G. D. Stucky, and D. E. Morse, *Nature*, 1996, **381**, 56-58.

59. G. Falini, S. Albeck, S. Weiner, and L. Addadi, *Science*, 1-5-1996, **271**, 67-69.

60. I. A. Aksay, M. Trau, S. Manne, I. Honma, N. Yao, L. Zhou, P. Fenter, P. M. Eisenberger, and S. M. Gruner, *Science*, 1996, **273**, 892-898.

61. A. P. Alivisatos, K. P. Johnsson, X. G. Peng, T. E. Wilson, C. J. Loweth, M. P. Bruchez, and P. G. Schultz, *Nature*, 1996, **382**, 609-611.

62. C. A. Mirkin, R. L. Letsinger, R. C. Mucic, and J. J. Storhoff, *Nature*, 1996, **382**, 607-609.

63. W. Shenton, D. Pum, U. B. Sleytr, and S. Mann, *Nature*, 1997, **389**, 585-587.

64. H. Colfen and M. Antonietti, *Langmuir*, 1998, **14**, 582-589.

65. L. M. Qi, H. Colfen, and M. Antonietti, *Nano Letters*, 2001, **1**, 61-65.

66. S. Minko, A. Kiriy, G. Gorodyska, and M. Stamm, *Journal of the American Chemical Society*, 2002, **124**, 10192-10197.

67. J. D. Hartgerink, E. Beniash, and S. I. Stupp, *Science*, 2001, **294**, 1684-1688.

68. M. F. Zhang, M. Drechsler, and A. H. E. Muller, *Chemistry of Materials*, 2004, **16**, 537-543.

69. J. H. Jung, Y. Ono, K. Hanabusa, and S. Shinkai, *Journal of the American Chemical Society*, 2000, **122**, 5008-5009.

70. B. M. Rabatic, M. U. Pralle, G. N. Tew, and S. I. Stupp, *Chemistry of Materials*, 2003, **15**, 1249-1255.

71. P. V. Braun, P. Osenar, V. Tohver, S. B. Kennedy, and S. I. Stupp, *Journal of the American Chemical Society*, 1999, **121**, 7302-7309.

72. S. W. Lee, C. B. Mao, C. E. Flynn, and A. M. Belcher, *Science*, 2002, **296**, 892-895.

73. J. Richter, M. Mertig, W. Pompe, I. Monch, and H. K. Schackert, *Applied Physics Letters*, 2001, **78**, 536-538.

74. T. Scheibel, R. Parthasarathy, G. Sawicki, X. M. Lin, H. Jaeger, and S. L. Lindquist, *Proceedings of the National Academy of Sciences of the United States of America*, 2003, **100**, 4527-4532.

75. H. Yan, S. H. Park, G. Finkelstein, J. H. Reif, and T. H. Labean, *Science*, 2003, **301**, 1882-1884.

76. E. D. Sone, E. R. Zubarev, and S. I. Stupp, *Angewandte Chemie-International Edition*, 2002, **41**, 1706.

77. Q. Liao, A. V. Dobrynin, and M. Rubinstein, *Macromolecules*, 2006, **39**, 1920.

78. A. Kiriy, G. Gorodyska, S. Minko, W. Jaeger, P. Stepanek, and M. Stamm, *Journal of the American Chemical Society*, 2002, **124**, 13454-13462.

79. L. J. Kirwan, G. Papastavrou, M. Borkovec, and S. H. Behrens, *Nano Letters*, 2004, **4**, 149-152.

80. A. V. Dobrynin, M. Rubinstein, and S. P. Obukhov, *Macromolecules*, 1996, **29**, 2974-2979.

81. A. V. Lyulin, B. Dunweg, O. V. Borisov, and A. A. Darinskii, *Macromolecules*, 1999, **32**, 3264-3278.

82. A. P. Alivisatos, *Science*, 1996, **271**, 933-937.

83. S. Link and M. A. El-Sayed, *International Reviews in Physical Chemistry*, 2000, **19**, 409-453.

84. R. rossetti, R. Hull, and L. E. Brus, *Journal of Chemical Physics*, 1985, **82**, 552.

85. Y. Wang and N. Herron, *Journal of Physical Chemistry*, 1991, **95**, 525-532.

86. A. L. Efros and M. Rosen, *Annual Review of Materials Science*, 2000, **30**, 475.

87. L. E. Brus, *Journal of Chemical Physics*, 1984, **80**, 4403-4409.

88. J. K. Jaiswal, H. Mattoussi, J. M. Mauro, and S. M. Simon, *Nature Biotechnology*, 2003, **21**, 47-52.

89. W. C. W. Chan, D. J. Maxwell, X. H. Gao, R. E. Bailey, M. Y. Han, and S. M. Nie, *Current Opinion in Biotechnology*, 2002, **13**, 40-46.

90. L. E. Brus, *Journal of Chemical Physics*, 1983, **79**, 5566.

91. M. A. Hines and P. Guyot-Sionnest, *Journal of Physical Chemistry*, 1996, **100**, 468-471.

92. M. Bruchez, M. Moronne, P. Gin, S. Weiss, and A. P. Alivisatos, *Science*, 1998, **281**, 2013-2016.

93. W. C. W. Chan and S. M. Nie, *Science*, 1998, **281**, 2016-2018.

94. N. Herron, Y. Wang, and H. Eckert, *Journal of the American Chemical Society*, 1990, **112**, 1322-1326.

95. M. Kundu, A. A. Khosravi, S. K. Kulkarni, and P. Singh, *Journal of Materials Science*, 1997, **32**, 245-258.

96. K. M. Choi and K. J. Shea, *Journal of the American Chemical Society*, 1994, **116**, 9052-9060.

97. P. lianos and J. K. Thomas, *Chemical Physics Letters*, 1986, **125**, 299-302.

98. R. S. Urquhart, D. N. Furlong, T. Gengenbach, N. J. Geddes, and F. Grieser, *Langmuir*, 1995, **11**, 1127-1133.

99. X. K. Zhao, S. Q. Xu, and J. H. Fendler, *Langmuir*, 1991, **7**, 520-524.

100. C. B. Murray, D. J. Norris, and M. G. Bawendi, *Journal of the American Chemical Society*, 1993, **115**, 8706-8715.

101. L. Manna, E. C. Scher, and A. P. Alivisatos, *Journal of the American Chemical Society*, 2000, **122**, 12700-12706.

102. D. J. Milliron, S. M. Hughes, Y. Cui, L. Manna, J. B. Li, L. W. Wang, and A. P. Alivisatos, *Nature*, 2004, **430**, 190-195.

103. X. G. Peng, L. Manna, W. D. Yang, J. Wickham, E. Scher, A. Kadavanich, and A. P. Alivisatos, *Nature*, 2000, **404**, 59-61.

104. M. Bruchez, M. Moronne, P. Gin, S. Weiss, and A. P. Alivisatos, *Science*, 1998, **281**, 2013-2016.

105. J. H. Fendler, *Chemistry of Materials*, 1996, **8**, 1616-1624.

106. A. P. Alivisatos, K. P. Johnsson, X. G. Peng, T. E. Wilson, C. J. Loweth, M. P. Bruchez, and P. G. Schultz, *Nature*, 1996, **382**, 609-611.

107. B. Oregan and M. Gratzel, *Nature*, 1991, **353**, 737-740.

108. A. Tredicucci, C. Gmachl, F. Capasso, D. L. Sivco, A. L. Hutchinson, and A. Y. Cho, *Nature*, 1998, **396**, 350-353.

109. S. Coe, W. K. Woo, M. Bawendi, and V. Bulovic, *Nature*, 2002, **420**, 800-803.

110. V. L. Colvin, M. C. Schlamp, and A. P. Alivisatos, *Nature*, 1994, **370**, 354-357.

111. M. Y. Gao, C. Lesser, S. Kirstein, H. Mohwald, A. L. Rogach, and H. Weller, *Journal of Applied Physics*, 2000, **87**, 2297-2302.

112. J. Lee, V. C. Sundar, J. R. Heine, M. G. Bawendi, and K. F. Jensen, *Advanced Materials*, 2000, **12**, 1311.

113. C. Lesser, M. Gao, and S. Kirstein, *Materials Science & Engineering C-Biomimetic and Supramolecular Systems*, 1999, **8-9**, 159-162.

114. T. Piok, S. Gamerith, C. Gadermaier, H. Plank, F. P. Wenzl, S. Patil, R. Montenegro, T. Kietzke, D. Neher, U. Scherf, K. Landfester, and E. J. W. List, *Advanced Materials*, 2003, **15**, 800.

115. K. K. Likharev, *Proceedings of the Ieee*, 1999, **87**, 606-632.

116. P. Facci, V. Erokhin, S. Carrara, and C. Nicolini, *Proceedings of the National Academy of Sciences of the United States of America*, 1996, **93**, 10556-10559.

117. D. Goldhaber-Gordon, H. Shtrikman, D. Mahalu, D. busch-Magder, U. Meirav, and M. A. Kastner, *Nature*, 1998, **391**, 156-159.

118. D. L. Klein, R. Roth, A. K. L. Lim, A. P. Alivisatos, and P. L. Mceuen, *Nature*, 1997, **389**, 699-701.

119. P. Michler, A. Kiraz, C. Becher, W. V. Schoenfeld, P. M. Petroff, L. D. Zhang, E. Hu, and A. Imamoglu, *Science*, 2000, **290**, 2282.

120. M. Ouyang and D. D. Awschalom, *Science*, 2003, **301**, 1074-1078.

121. S. A. Wolf, D. D. Awschalom, R. A. Buhrman, J. M. Daughton, S. von Molnar, M. L. Roukes, A. Y. Chtchelkanova, and D. M. Treger, *Science*, 11-16-2001, **294**, 1488-1495.

122. P. V. Kamat and D. Meisel, *Semiconductor Nanoclusters- Physical, Chemical, and Catalytic Aspects*, 1997, **103**, 1-3.

123. Schmid, G., *Clusters and Colloids: From Theory to Application*, VCH: Weinheim, 1994.

124. Y. Xiao, F. Patolsky, E. Katz, J. F. Hainfeld, and I. Willner, *Science*, 2003, **299**, 1877-1881.

125. T. Sato, H. Ahmed, D. Brown, and B. F. G. Johnson, *Journal of Applied Physics* 7-15-1997, **82**, 696-701.

126. K.L. Johnson, *Contact Mechanics*, Cambridge Univ. Press, Cambridge, 1985.

127. T.W. Keller et al., *Chem. Mater.* 2004, 16, 4413.

128. V. Maheshwari, R.F. Saraf, *Langmuir* 2006, ***22***, 8623-8626.

129. N. Duxin, F.T. Liu, H. Vali, A. Eisenberg, *J.Am. Chem. Soc.* 2005, ***127*** (28), 10063.

130. .J. Solis, M.O. de la Cruz, *Macromolecules* 1998, ***31*** (16), 5502.

131. A.V. Lyulin, B. Dunweg, O.V. Borisov, A.A. Darinskii, *Macromolecules* 1999, ***32*** (10), 3264.

132. L.E. Brus, *J. Chem. Phys.* 1984, ***80*** (9), 4403.

133. N.S. Pesika, K.J. Stebe, P.C. Searson, *Adv. Mater*. 2003, ***15*** (15), 1289.

134. T.A. Waigh, R. Ober, C.E. Williams, J.C. Galin, *Macromolecules* 2001, ***34*** (6), 1973.

Vitae

Vivek Chandra Maheshwari, born on 09th, January 1976 at Ajmer City, Rajasthan India, completed his Ph.D. from Virginia Polytechnic Institute and State University, Blacksburg, Virginia, USA in December of 2006. He obtained is Bachelors in Chemical Engineering from Indian Institute of Technology, New Delhi, India in 1998 and a Masters in Chemical Engineering from Wayne State University, Detroit, Michigan, USA in 2001. He worked as Young Professional at Pasupati Acrylon from ‘98-’99. He is son of Dr. Suresh and Leela Maheshwari.